STREAMLINE-BASED THREE-PHASE HISTORY MATCHING

A Dissertation

by

ADEDAYO STEPHEN OYERINDE

Submitted to the Office of Graduate Studies of
Texas A&M University
in partial fulfillment of the requirements for the degree of

DOCTOR OF PHILOSOPHY

May 2008

Major Subject: Petroleum Engineering

STREAMLINE-BASED THREE-PHASE HISTORY MATCHING

A Dissertation

by

ADEDAYO STEPHEN OYERINDE

Submitted to the Office of Graduate Studies of
Texas A&M University
in partial fulfillment of the requirements for the degree of

DOCTOR OF PHILOSOPHY

Approved by:

Chair of Committee,	Akhil Datta-Gupta
Committee Members,	Christine Ehlig-Economides
	Robert Wattenbarger
	Yalchin Efendiev
Head of Department,	Steve Holditch

May 2008

Major Subject: Petroleum Engineering

ABSTRACT

Streamline-Based Three-Phase History Matching.
(May 2008)
Adedayo Stephen Oyerinde, B.S., University of Ibadan;
M.S., Texas A&M University
Chair of Advisory Committee: Dr. Akhil Datta-Gupta

Geologic models derived from static data alone typically fail to reproduce the production history of a reservoir, thus the importance of reconciling simulation models to the dynamic response of the reservoir. This necessity has been the motivation behind the active research work in history matching. Traditionally, history matching is performed manually by applying local and regional changes to reservoir properties. While this is still in general practice, the subjective overtone of this approach, the time and manpower requirements, and the potential loss of geologic consistency have led to the development of a variety of alternative workflows for assisted and automatic history matching. Automatic history matching requires the solution of an inverse problem by minimizing an appropriately defined misfit function.

Recent advances in geostatistics have led to the building of high-resolution geologic models consisting of millions of cells. Most of these are scaled up to the sub-million size for reservoir simulation purposes. History matching even the scaled up models is computationally prohibitive. The associated cost in terms of time and manpower has led to increased interest in efficient history matching techniques and in particular, to sensitivity-based algorithms because of their rapid convergence. Furthermore, of the sensitivity-based methods, streamline-based production data integration has proven to be extremely efficient computationally.

In this work, we extend the history matching capability of the streamline-based technique to three-phase production while addressing in general, pertinent issues associated with history matching. We deviate from the typical approach of formulating the inverse problem in terms of derived quantities such as GOR and Watercut, or measured phase rates, but concentrate on the fundamental variables that characterize such quantities. The presented formulation is in terms of well node saturations and pressures. Production data is transformed to composite saturation quantities, the time variation of which is matched in the calibration exercise. The dependence of the transformation on pressure highlights its importance and thus a need for pressure match. To address this need, we follow a low frequency asymptotic formulation for the pressure equation. We propose a simultaneous inversion of the saturation and pressure components to account for the interdependence and thus, high non-linearity of three phase inversion. We also account for global parameters through experimental design methodology and response surface modeling. The validity of the proposed history matching technique is demonstrated through application to both synthetic and field cases.

DEDICATION

To my beloved parents, my brother, and my sister for their unconditional love and relentless support.

ACKNOWLEDGEMENTS

All glory, laud and honor to God almighty for His infinite mercies and abundant blessings.

I would like to express my gratitude to the management of ExxonMobil for the scholarship award that has afforded me the opportunity of pursuing my graduate studies.

I would like to thank my academic advisor, Dr. Akhil Datta-Gupta for his encouraging words and unparalleled academic guidance through my years of study.

I would also like to thank the members of my committee, Dr. Christine Ehlig-Economides, Dr. Robert Wattenbarger, and Dr. Yalchin Efendiev for the valuable comments and the insightful questions that have shaped the work in this dissertation.

Special thanks to my colleagues in the research group, Eduardo Jimenez and Deepak Devegowda, with whom I started this program, for the constructive discussions and knowledge sharing over the years. Also, to past member of the group, Dr. Ahmed Daoud, Dr. Hao Cheng, Dr. Al Harbi, and present members, Xianlin, Ahmed, Kim, Ajitabh, Pranay, Sarwesh, Alvaro, Shingo, Matt, Jiang, Jichao, thanks for your friendship and making my graduate years memorable.

Finally, to Titi, and Aygeero, thanks for the encouragement and support.

NOMENCLATURE

A	Maximum amplitude of observation data
β	Scalar weighting on regularization terms
Bo,w,g	Phase formation volume factor for oil, water, and gas
c	Divergence of flux
C	Phase compressibility
D	Depth
ξ	Phase molar density
$\vec{d}$	data vector
Ef	Bending Energy of Thin plate splines
f	fractional flow
g	Gravitational force
$g[m], g[\vec{R}]$ g	Simulator response to vector of reservoir parameter $\vec{R}$
G	Greens function
J	Flux
$\vec{K}$	Dispersion Tensor
k	Absolute Permeability
k_r	Relative permeability
L	Second order spatial difference operator
m	Reservoir model parameter
M	Stacked Sensitivity Matrix
N_{dj}	Number of observation data
ϕ	Porosity
P	Pressure

$P_{nw,\, w}$	Non-wetting and wetting phase pressure
$\hat{P}$	Fourier transform of pressure
ρ	Density
Φ	Potential
q	Injection or production rate
Q	Volumetric flux
$\vec{R}$	Vector of reservoir parameters
$\mathbf{R}$	Source/Sink Term
R_s	Solution gas-oil ratio
r_o	Peaceman's well radius
r_w	Wellbore radius
s	Skin factor
S	Phase Saturation
S_{ij}	Sensitivity of response *i* to model parameter *j*
t	Time
T	Transmissibility
$\boldsymbol{T}$	Transformation operator
τ	Time of flight
$\vec{u}$	Darcy Velocity
μ	viscosity
υ	Interstitial velocity
ω	frequency
W	Accumulation term
w	Weight of non-affline component of 'thin plate' spline interpolant
x_{ij}	Mole fraction of component *i* in phase *j*
λ	Mobility
ψ, χ	Bi-stream function

γ	Specific gravity
σ	Phase term for frequency domain
Ω	Parameter Space

TABLE OF CONTENTS

LIST OF FIGURES

Page

Page

LIST OF TABLES

CHAPTER I

INTRODUCTION

The need for accurate business projections based on production forecast provided by reservoir simulation studies has been the key motivating factor behind the active work done in the field of reservoir characterization. Reservoir simulation models are typically scaled up derivatives of the corresponding geologic models often referred to as static models. It is no surprise that these geologic models often fail to reproduce production history as they are generated through geostatistical interpolation of reservoir properties based on measurements obtained from just a few wells drilled in the field. Since the governing differential equations modeling fluid flow in the reservoir relates reservoir properties to well production, conceivably, through an inverse algorithm, underlying reservoir properties can be reconstructed given observed production data and model (simulator) response.[1-9] The approach of calibrating reservoir models to dynamic data is termed “History Matching”. As a convenient alternative to implementing the solution to the inverse problem, the traditional approach to history matching in the industry involves making educated guesses on property multipliers to be applied to specific regions of the model in order to obtain a fit between the model response and observed production.

While the subjective overtone of this approach to reconciling geologic model to dynamic data makes it difficult to assess, this is still a prevalent approach to history matching in the industry. Perhaps the greatest shortcomings of manual history matching are its inability to yield geologically plausible reservoir models, and the extensive turn around time of a model calibration exercise leading ultimately to the inability to examine multiple realizations. To circumvent much of these problems, the industry trend has been towards assisted and automatic history matching.[10]

This dissertation follows the style of *SPE Journal*.

1.1 Assisted and Automatic History Matching

Assisted history matching (AHM), can be considered a logical successor to manual history matching in that while intuition dictates the regions of the reservoir to which multipliers are applied in the manual approach, it is the components of flow mechanism that determines the region of the reservoir that influences production response at a well. Milliken et. al have shown successful application of streamlines in assisted history matching.[10] Transitioning from manual to assisted history matching eliminates some of the subjective nature of manual history matching. However, applying multipliers to regions often results in the loss of geologic realism characteristic of manual history matching, albeit a time consuming calibration effort. Automatic history matching algorithms offer a further improvement in reconciling geologic models to dynamic data. The iterative inversion algorithms are typically formulated to minimize a pre-specified objective function primarily aimed at reducing the data misfit between production and model response.[11] Also, the objective function includes regularization terms that address the issue of geologic consistency between pre and post inversion reservoir models.[1] In a broad sense, automatic history matching algorithms can be classified as either deterministic or Bayesian.[12] Given a prior geologic model, the deterministic algorithms produce a single model conditioned to production data. Bayesian adherents on the other hand are of the opinion that an ensemble and not a single reservoir model represent the heterogeneity characteristic of a reservoir and also, the fact that the uncertainty in model predictions can be assessed given a suite of realizations obtained from an inversion formulated in a Bayesian framework. Nonetheless, both these methods are still used in the industry. Amongst these automatic history matching methods, of particular interest in this work are the sensitivity-based algorithms discussed next.

1.2 Sensitivity-Based History Matching Algorithms and Streamline Methods

The prominence of sensitivity-based history matching algorithms can be largely attributed to the rapid convergence they exhibit.[13] Because of the computational challenge posed by even the smallest of field-scale history-matching endeavors, it becomes imperative for the computation of sensitivity coefficients to be as efficient as practically possible. One of the distinguishing features of streamline-based history matching algorithms is their superior efficiency in computing sensitivity coefficients.[1] It is the rapid sensitivity computation and thus applicability of the streamline-based method achieved in two phase applications that motivates the extension to three-phase production data researched in this work. The efficacy of the approach in calculating sensitivities is a direct consequence of the nature of the streamline formulation for modeling the dynamics of fluid flow. In the streamline domain, the flow and transport equations are decoupled with a resulting reduction of the solution of a three-dimensional problem to a series of one-dimensional problems.[14] In chapter II, we discuss the streamline formulation for the forward problem, and the sensitivity formulation for the inverse problem is detailed in chapter III.

1.3 Choice of Observation Data and Misfit Calculation

In most of the automatic history matching algorithms related to two and three-phase production data, the inverse problem is formulated such that the misfit between historical data and model response at each observation is quantified as the amplitude difference between these two. An inversion scheme formulated around such misfit quantification is termed an amplitude inversion. A different approach to quantifying the misfit between production history and model response is the travel-time inversion.[1, 15] In this approach, the misfit is quantified as the difference between the arrival times of a particular observation on both the historical data and model response. It has been shown that the non-linearity associated with the amplitude inversion is orders of magnitude greater than that of travel-time inversion.[16] The high non-linearity of amplitude inversion has adverse consequences on the convergence of the iterative inversion algorithm. Since rapid model calibration is of particular importance, the inversion approach followed in this research work is based on variations of travel-time inversion and will be discussed in chapter III.

Also, most of the automatic history matching algorithms formulate the inverse problem around matching quantities such as water-oil ratio (WOR), gas-oil ratio (GOR), and water-cut (WCT). In general, matching ratios has uniqueness implications and as such, this research work deviates from this trend and focuses on the fundamental variables at a well node, which uniquely characterize production. The fundamental variables are the phase saturations and the bottom-hole flowing pressure. These represent our choice of ‘observed’ data. This work shows that for two phase water-oil production, a phase saturation and bottom-hole flowing pressure at the producing well block completely characterize the production at the well. For the equivalent three-phase problem, two phase saturations and the bottom-hole flowing pressure at the well node are required to completely define the production at the well. While it is possible to formulate the inverse problem in an amplitude sense, and also compute sensitivities to production history, the approach presented herein is a travel-time type inversion that avoids the problems associated with amplitude matching. In chapter III, we show that the travel-time formulation of the inverse problem is a natural domain for computing component sensitivities using streamline models.

1.4 Objectives

The primary purpose of this research work is to present a robust streamline-based algorithm for history matching three-phase production data that addresses pertinent history matching issues and can be applied to large reservoir models. The choice of exploiting the streamline methodology is a result of its success in two-phase oil-water applications to geo-cellular models. Although the formulation of the inverse problem is for the most part presented in the streamline framework, the method can be extended to finite-difference models and the differences and commonalities in application between the streamline and finite difference models are pointed out in the discourse.

As will be shown in chapter III, travel-time sensitivities to saturation components are based on the streamline formulation generalized for three-phase compressible flow. The sensitivity formulation presented neglects the pressure dependence of the saturation components and thus represents an approximation to the true arrival time sensitivity especially for the gas saturation component. In chapter IV, the pressure component is explicitly accounted for by an asymptotic approach to pressure inversion after Vasco et. al.[17] This is incorporated into the presented streamline-based data integration workflow to honor, the variables that characterize production at a well node.

In the expression for the arrival time sensitivities of saturation components, the importance of PVT properties of the fluid and the relative permeability curves quickly becomes obvious. As there usually is reason to doubt how representative of field wide displacement a SCAL data based on isolated measurements is, end-points and critical saturations of relative permeability curves then represent global variables subject to optimization. In this study, an experimental design methodology coupled with response surface modeling using thin-plate splines is used to handle optimization of SCAL variables for the purpose of history matching. Needless to say this method can also be applied in the optimization of other global parameters such as fault transmissibility.

In all cases, presented concepts are validated through application to synthetic cases under the appropriate sections. The rigor and robustness of the presented inverse algorithm as a whole is provided by application to field cases as shown in chapters IV and V.

CHAPTER II

THE FORWARD MODEL

In this chapter, the basic governing equations for isothermal, multicomponent, and multiphase flow in permeable media are introduced in a finite-difference framework. Necessary assumptions are then made that reduce the formalism to the specific case of black-oil which is most commonly used to model fluid flow in petroleum reservoirs. The equivalent representation of the finite-difference equations are then presented in a streamline framework which is the basis of computing the sensitivity coefficients discussed in chapter III.

The finite-difference representation of the well model, which is greatly simplified in the streamline simulation framework, is briefly discussed as a preview to the discussion on transformation of production data to saturation components at the well block for finite-difference applications.

2.1 Mass Conservation Equations

Datta-Gupta and King describe multicomponent, multiphase flow in permeable media as the transport of multiple chemical species in homogeneous phases under viscous forces, gravity, mixing, and capillarity.[18] At each point in the medium, the mass conservation equation applies for each component. The general mass conservation equation for component *i* can be expressed as:

$$\frac{\partial W_i}{\partial t} + \nabla \bullet \vec{J}_i = R_i \quad \text{......} \quad 2.1$$

where W_i, J_i, and R_i are the accumulation, flux, and source or sink terms respectively (Lake, 1989).[19] Each term has units of molar flow rate per unit bulk (reservoir) volume. Expanding Eq. 2.1, neglecting component adsorption to the rock in the accumulation term, and accounting for both convection and dispersion in the flux term results in the equation below:

$$\frac{\partial}{\partial t}\left\{\phi\sum_{j=1}^{n_p}\xi_j S_j x_{ij}\right\}+\nabla\bullet\sum_{j=1}^{n_p}\left(\xi_j x_{ij}\vec{u}_j-\phi\xi_j\vec{\vec{K}}_{ij}\bullet\nabla x_{ij}\right)=r_i \quad i=1\ldots n_c \quad \ldots\ldots\ldots\ldots \quad 2.2$$

where, ϕ is porosity, ξ_j is molar density of phase *j*, S_j is the saturation of phase *j*, and x_{ij} is the mole fraction of component *i* in phase *j*. $\vec{u}_j$ is the Darcy velocity for phase *j* and $\vec{\vec{K}}$ is the dispersion tensor. Phase pressures are introduced into the model through phase fluxes based on the multiphase version of Darcy's law,

$$\vec{u}_j=-\vec{\vec{k}}\bullet\lambda_{rj}(\nabla P_j-\rho_j g\nabla D)=-\vec{\vec{k}}\bullet\lambda_{rj}\nabla\Phi_j \quad \ldots\ldots\ldots\ldots\ldots\ldots\ldots\ldots\ldots\ldots\ldots \quad 2.3$$

Where $\lambda_{rj}=\frac{k_{rj}}{\mu_j}$ represents the relative mobility of each phase, *D*, the datum depth and Φ_j is the phase potential. The coupled nonlinear partial differential equation (Eq. 2.2) is solved by satisfying the requirement of equality of component fugacities in each phase based on equations of state, and specifying the appropriate initial and boundary conditions.

2.2 Initial and Boundary Conditions

The initial conditions for the conservation equations require the specification of the phase pressures and total number of moles of each component. The individual phase compositions and saturations are then obtained from thermodynamic equilibrium calculations. Since capillary pressure functions define the relationship between the phase pressures, knowing the saturations, the phase pressures are thus easily obtained.

$$P_{nw}-P_w=P_{cnw,w}(s) \quad \ldots\ldots\ldots\ldots\ldots\ldots\ldots\ldots\ldots\ldots\ldots\ldots\ldots\ldots\ldots\ldots\ldots\ldots \quad 2.4$$

In order to satisfy static equilibrium conditions in the presence of capillary and gravity forces, where $\vec{u}_j=0$ in Eq. 2.3,

$$\frac{dPc_{nw,w}(S)}{dD} = \Delta\rho g \quad \ldots\ldots\ldots\ldots\ldots\ldots\ldots\ldots\ldots\ldots\ldots\ldots\ldots\ldots\ldots\ldots \quad 2.5$$

where,

$$\Delta\rho = \rho_j - \rho_l \quad \ldots\ldots\ldots\ldots\ldots\ldots\ldots\ldots\ldots\ldots\ldots\ldots\ldots\ldots\ldots\ldots \quad 2.6$$

The initial fluid distribution in the reservoir is thus determined through Eq. 2.5 by integrating from the free water level ($P_{cnw,w}=0$) to the depth of the center of each grid block.

The boundary conditions include inflow, outflow, and no-flow boundaries and require specifying either the value of the state variable on the boundary (Dirichlet condition) or its derivative (Carl Neumann condition).

2.3 Black-Oil Equations

The black-oil model represents a special case of the multicomponent multiphase flow in porous media presented in the last section. Several assumptions (Peaceman, 1977; Lake et al 1984) are made in reducing the more general equation 2.2 to the more frequently used black-oil equations. The basic assumptions are summarized below.[19]

1. Maximum of three phases flowing; water $(j=1)$, oil $(j=2)$, and gas $(j=3)$
2. Maximum of three components, water $(i=1)$, oil $(i=2)$, and gas $(i=3)$
3. Water phase exists as a single pseudocomponent ($x_{11}=1; x_{21}=x_{31}=0$)
4. Gas phase exists as a single pseudocomponent ($x_{33}=1; x_{31}=x_{32}=0$)
5. Oil phase ($j=2$) can have dissolved gas in it ($x_{22}>=0,\ x_{32}>=0;\ x_{21}=0$)

The introduction of the definitions of formation volume factors and solution gas-oil ratio and their relation to molar density and mole fractions facilitates the derivation of the black-oil equation. Thus,

Water formation volume factor $B_w = \frac{\xi_1^s}{\xi_1}$

Oil formation volume factor $B_o = \frac{\xi_2^s}{x_{22}\xi_2}$

Solution gas-oil ratio $R_s = \dfrac{\dfrac{x_{32}\xi_2}{\xi_3^s}}{\dfrac{x_{22}\xi_2}{\xi_2^s}} = \dfrac{x_{32}\xi_2^s}{x_{22}\xi_3^s}$

Gas formation volume factor $B_g = \dfrac{\xi_3^s}{\xi_3}$

Substituting these relations in Eq. 2.2, neglecting dispersion, and expressing the resulting equation in standard volumes gives the black-oil equations below: (Peaceman, 1977; Lake et al 1984)

$$\frac{\partial}{\partial t}\left(\frac{\phi S_{j=o,w}}{B_{j=o,w}}\right)+\nabla\bullet\left(\frac{\vec{u}_{j=o,w}}{B_{j=o,w}}\right)=q^s_{j=o,w} \quad \text{………………………………….…} \quad 2.7$$

for water and oil phases, and

$$\frac{\partial}{\partial t}\left(\phi\left[\frac{S_g}{B_g}+\frac{S_o R_s}{B_o}\right]\right)+\nabla\bullet\left(\frac{\vec{u}_o R_s}{B_o}+\frac{\vec{u}_g}{B_g}\right)=q^s_g \quad \text{……………………………...} \quad 2.8$$

Where q represents the injection or production rate of the phases in standard volumes per unit bulk (reservoir) volume.

2.4 Black-Oil Pressure Equation

The development and discussion of the underlying pressure equation is deferred until chapter V where we start to account for the role of pressure in history matching. It suffices to state at this point that considering an IMPES formulation for the finite-difference scheme for consistency with the streamline formulation, the pressure equation and its solution in both formulations (Finite-Difference and Streamline Simulation) are exactly the same. The fundamental difference being that in streamline simulation, the streamlines represent the computational domain for the saturation equation after appropriate coordinate transformation discussed in the next section. Next we consider the equivalent streamline representation of the saturation equations.

2.5 Black-Oil Equations: A Streamline Formulation

In 3-D, streamlines are defined by the intersection of two bi-streamfunctions, ψ and χ.[20] For compressible three-phase flow in porous media, the conserved quantity is a total multi-phase mass flux. Accordingly, the bi-streamfunctions are defined to incorporate the compressibility effects.[21]

$$\rho\vec{u} = \nabla\psi \times \nabla\chi \quad \ldots\ldots\ldots\ldots\ldots\ldots\ldots\ldots\ldots\ldots \quad 2.9$$

where ρ represents an 'effective density' of the total fluid. Since $\rho\vec{u}$ represents a conserved flux.

$$0 = \nabla \bullet (\nabla\psi \times \nabla\chi) = \nabla \bullet (\rho\vec{u}) = \vec{u} \bullet \nabla\rho + \rho\nabla \bullet \vec{u} \quad \ldots\ldots\ldots\ldots \quad 2.10$$

In streamline simulation, we work in the time of flight coordinates rather than the physical space.[2] The coordinate change is characterized by the Jacobian of transformation.

$$\left\| \frac{\partial(\tau,\psi,\chi)}{\partial(x,y,z)} \right\| = (\nabla\psi \times \nabla\chi) \bullet \nabla\tau = \rho\vec{u} \bullet \nabla\tau = \rho\phi \quad \ldots\ldots\ldots\ldots \quad 2.11$$

$$\vec{u} \bullet \nabla = \phi \frac{\partial}{\partial\tau} \quad \ldots\ldots\ldots\ldots\ldots\ldots\ldots\ldots\ldots\ldots \quad 2.12$$

Eq. 2 11 shows that the operator identity (Eq. 2.12) used for incompressible streamline formulation also holds good for compressible flow. Applying the identity to Eq. 2.10 gives the ordinary differential equation below.

$$\phi \frac{\partial \rho}{\partial \tau} + \rho \nabla \bullet \vec{u} = 0 \quad \text{...} \quad 2.13$$

where the divergence of flux $\nabla \bullet \vec{u}$ is a constant within each grid cell but varies spatially along the streamlines from cell to cell. Integrating Eq.2.12 permits the evaluation of the effective density along the streamlines starting with a value of unity at the injectors.

$$\rho = \rho_o e^{-\left(c\frac{\tau}{\phi}\right)} \quad \text{..} \quad 2.14$$

where c represents the local divergence of flux. With the initial volumetric flux $\Delta Q = \Delta\psi\Delta\chi$ being assigned to a streamline, and conserving mass assigned to a streamline, the volumetric flux will vary along the streamline according to the relationship $\frac{\Delta Q}{\rho}$.

2.5.1 Black-Oil Saturation Equations in Streamline Coordinates

To transform the black-oil saturation equations (Eqs. 2.7 and 2.8) to the equivalent equations in streamline coordinates, we use the operator identity (Eq. 2.12) and the relations

$$\vec{u}_{j=o,w,g} = f_{j=o,w,g}\vec{u} \quad \text{...} \quad 2.15$$

where $\vec{u}$ is the total volumetric flux and f, the fractional flow. Expanding Eqs. 2.7 and 2.8, writing the phase volumetric fluxes in terms of total volumetric flux, and applying the operator identity gives the saturation equations (away from sources/sinks) in terms of time-of-flight coordinates

$$\phi \frac{\partial}{\partial t}\left(\frac{S_w}{B_w}\right) + \phi \frac{\partial}{\partial \tau}\left(\frac{f_w}{B_w}\right) = -c\frac{f_w}{B_w} \quad \text{..} \quad 2.16$$

Equation 2.16 is the water saturation equation and Eq. 2.17 is the gas saturation equation away from sources/sinks

$$\phi\frac{\partial}{\partial t}\left(\frac{S_g}{B_g}+\frac{S_oR_s}{B_o}\right)+\phi\frac{\partial}{\partial\tau}\left(\frac{f_g}{B_g}+\frac{R_sf_o}{B_o}\right)=-c\left(\frac{f_g}{B_g}+\frac{R_sf_o}{B_o}\right) \quad \text{..................} \quad 2.17$$

Where the right hand terms in equations (Eqs. 2.16 and 2.17) can be seen as a compressibility-induced source term attributable to fluid compression and expansion. For incompressible flow, $c=0$ everywhere and the right hand term vanishes as expected. These equations are the basis of obtaining the gas and water saturation travel-time sensitivities applied in the three-phase inversion algorithm that is introduced in the chapter III.

2.6 Three-Phase Relative Permeability Model

The three phase relative permeability data models the rock-fluid interaction and relative displacement characteristics of fluid in the reservoir. Two sets of relative permeability curves model the relative fluid displacement for three-phase flow. The relative permeability for the wetting and non-wetting phases is strictly a function of their respective saturations while that of the intermediate wetting phase depends on the saturation of the other phases.[21] For water-wet rocks, this translates to the water relative permeability being strictly a function of water saturation, and the gas relative permeability, a strict function of gas saturation while oil relative permeability is a function of both water and gas saturations.

In this work, the relative permeability model used is a modified version of Stone's second model based on the channel flow theory after Aziz and Settari (1977). Also,.

$$k_{rw}=f(S_w) \quad \text{...} \quad 2.18$$

$$k_{rg}=f(S_g) \quad \text{...} \quad 2.19$$

$$k_{ro}=k_{rocw}\left[\left(\frac{k_{row}}{k_{rocw}}+k_{rw}\right)\left(\frac{k_{rog}}{k_{rocw}}+k_{rg}\right)-k_{rw}-k_{rg}\right] \quad \text{...............................} \quad 2.20$$

the equations above (Eqs. 2.18, 2.19, and 2.20) describe the relative permeability relations given a set of water-oil relative permeability curves and another for gas-oil at connate water saturation. The transformation of production data to saturation components, which represent the basis of the history matching approach presented here relies on these fundamental relationships.

2.7 The Well Model

A simplified well model is presented for illustrative purposes. As stated in the previous section, the boundary condition could be either pressure (Dirichlet) or rate (Neumann) constraint. Neglecting friction losses in the wellbore, and assuming a variable density gradient, the governing equation for a well with k_l layers is given by

$$q_s = \sum_{k=1}^{k_l} T_k^w \left[P_k^w - P_k \right] \quad \text{……………………………………………………....…… 2.21}$$

where P_k^w is the wellbore pressure and P_k is the pressure in the gridblock. T_k^w is the layer transmissibility given by

$$T_k^w = \frac{2\pi \Delta z_k}{\ell n\left(\dfrac{r_{o,k}}{r_{w,k}}\right) + s_k} \lambda_{t,k}^w \quad \text{…………………………………………………..….. 2.22}$$

s_k is the skin factor, $r_{o,k}$ and $r_{w,k}$ are respectively, the Peaceman's and wellbore radii and $\lambda_{t,k}^w$ is the total mobility of the gridblock.[22] Assuming a variable density gradient wellbore, the particular gridblock pressure can be related to the pressure at the topmost gridblock completion (k^t)

$$P_k^w = P_{k^t}^w + 0.5 \sum_{i=k^t+1}^{k} \left(\gamma_{i-1} + \gamma_i \right)\left(D_i - D_{i-1} \right) \quad \text{…………………………………... 2.23}$$

D_i is the depth to the center of the i^{th} layer. The mobility weighted specific gravity at the wellbore γ_i can be calculated as

$$\gamma_i = \frac{\sum_{j=1}^{n_p} \frac{k_{rj}\rho_j g}{\mu_j}}{\sum_{j=1}^{n_p} \frac{k_{rj}}{\mu_j}} \qquad \ldots\ldots\ldots\ldots\ldots\ldots\ldots\ldots \quad 2.24$$

where the summation is over all phases present in each grid block. Substituting Eq. 2.23 into Eq. 2.21 gives the well production from all the completed layers

$$q_s = \sum_{k=1}^{k_l} T_k^w \left[P_{k^t}^w - P_k + 0.5 \sum_{i=k^t+1}^{k} (\gamma_{i-1} + \gamma_i)(D_i - D_{i-1}) \right] \qquad \ldots\ldots\ldots\ldots \quad 2.25$$

In calculating the fractional flow components required for transforming production data to saturation components, the form of Eq. 2.25 for well production is useful for finite difference applications as an approximation to the well production. For streamline applications on the other hand, this form would not be adequate as there is sub-grid resolution in the saturation calculations along a streamline. In essence, the block saturations used to compute the mobility terms in Eq. 2.25 would be erroneous. Thus the fractional flow of a phase *p* is given by

$$f_p = \frac{\sum_{k=1}^{k_l} T_{pk}^w \left[P_{k^t}^w - P_k + 0.5 \sum_{i=k^t+1}^{k} (\gamma_{i-1} + \gamma_i)(D_i - D_{i-1}) \right]}{\sum_{k=1}^{k_l} T_k^w \left[P_{k^t}^w - P_k + 0.5 \sum_{i=k^t+1}^{k} (\gamma_{i-1} + \gamma_i)(D_i - D_{i-1}) \right]} \qquad \ldots\ldots\ldots\ldots \quad 2.26$$

Where,

$$T_{pk}^{w} = \frac{2\pi\Delta z_k}{\ell n\left(\frac{r_{o,k}}{r_{w,k}}\right) + s_k} \lambda_{p,k}^{w} \qquad 2.27$$

The simplistic well model is primarily introduced in this section for the purpose of computing the equivalent saturations at the well node for multi-layer applications. A variation of the presented approach is to weight the layer saturations according to the product of the layer transmissibility and its connection factor with the well. This offers additional time savings as the minimization described in chapter III for obtaining equivalent saturations from well production is skipped.

2.8 Chapter Summary

In this chapter, starting with the mass conservation equation, and necessary constitutive relations, we arrive at the governing partial differential equations for modeling fluid flow in the reservoir. Necessary assumptions were made to simplify the form of the equation as it would apply to black oil models that are the most commonly used in reservoir simulation applications. The equations are then presented in the streamline representation through a coordinate transformation from the spatial to time-of-flight coordinates. We emphasized that the simplification obtained from the form of the transport equation in streamline coordinates motivates the approach to history matching in this work whereby the temporal variation of saturation components is matched rather than the typical representation of production data as WCT and GOR.

In this chapter we also discussed three phase relative permeability model and a simplistic well model as a precursor to the details of transformation of production data to saturation components discussed in the next chapter.

CHAPTER III

THE INVERSE MODEL

As stated in the introduction, the presented approach to history matching three-phase production data requires a simultaneous match on both the saturation components and the well flowing pressure. The streamline formulation offers a natural computational domain for solving the transport equations. It is the simplicity and efficiency with which the transport equations are solved in streamline simulation that is exploited when employed in history matching applications.[1, 15, 19] In this chapter, the match on the saturation components termed "saturation match" is discussed. The discussion of the match on well flowing pressure termed "pressure inversion" is deferred till chapter V.

The mathematical basis of the streamline approach to automatic history matching is first introduced and then the inverse algorithm is presented. In subsequent sections, each of the components of the inverse model is further discussed in details. The derivations are first generalized for three-phase incompressible flow. The special case of two-phase incompressible flow is shown to be a subset of the generalized formalism.

3.1 Estimation of Reservoir Properties: The Objective Function

Integration of dynamic data into reservoir model requires the solution of an inverse problem, that is, minimizing the misfit to a set of N observations d_i, $i=1,\ldots\ldots,N$:

$$\sum_{i=1}^{N}\left(d_i - g_i\left[\vec{R}\right]\right)^2 \quad \ldots\ldots\ldots\ldots\ldots\ldots\ldots\ldots\ldots\ldots\ldots\ldots\ldots\ldots\ldots\ldots \quad 3.1$$

where $g_i\left[\vec{R}\right]$ is the response of the forward model (streamline or finite-difference simulator described in chapter II) that predicts the i^{th} observation given a vector of reservoir properties $\left[\vec{R}\right]$. Linearizing Eq. 3.1 using a Taylor series expansion of $g_i\left[\vec{R}\right]$ about some initial reservoir model $\vec{R}^0$ and neglecting terms of second order and higher, the data misfit, which is observed minus calculated data, can be related to perturbations in reservoir properties.[1]

$$\delta d_i = d_i - g_i\left[\vec{R}^o\right] = \sum_{j=1}^{M} S_{ij}\delta R_j \quad \ldots\ldots\ldots\ldots\ldots\ldots\ldots\ldots\ldots\ldots\ldots \quad 3.2$$

where δR_j represents a perturbation in reservoir properties and S_{ij} are sensitivity coefficients which are discussed later. These coefficients are given by

$$S_{ij} = \frac{\partial g_i\left[\vec{R}^o\right]}{\partial R_j} \quad \ldots\ldots\ldots\ldots\ldots\ldots\ldots\ldots\ldots\ldots\ldots\ldots\ldots\ldots \quad 3.3$$

The inverse problem is then formulated to minimize the sum of squares of the data misfit or residuals.

$$\left\|\delta d - S\delta R\right\| = \sum_{i=1}^{N}\left(\delta d_i - \sum_{j=1}^{M} S_{ij}\delta R_j\right)^2 \quad \ldots\ldots\ldots\ldots\ldots\ldots\ldots\ldots\ldots\ldots \quad 3.4$$

where $\|\cdot\|$ represents the norm in the desired vector space. In the application presented, this is the Euclidean norm as the inverse problem is formulated in the Hilbert space; a usual vector space for the solution of the discrete problem.[23] Eq. 3.4 is the mathematical representation of the primary objective of the inverse problem.

3.1.1 Augmented Objective Function

In history matching in general, there are many more reservoir parameters than there are observations. This combined with the fact that the data are often noisy results in the solution to the inverse problem that can be non-unique and highly unstable numerically. Typically this instability is eliminated by introducing some form of regularization.[24] The regularization terms are functions which measure property of the model such as size or spatial roughness. The penalty terms are often quadratic functions on the set of models. In this work two penalty terms are imposed. The first is the model norm, and the second, the model roughness. The model norm is represented by

$$\|\delta R\| = \sum_{i=1}^{N} \left(\delta R_j\right)^2 \qquad 3.5$$

and the model roughness by

$$\|L\delta R\| = \sum_{i=1}^{N} \left(\Delta^2 \delta R_j\right)^2 \qquad 3.6$$

where L is a second order spatial difference operator that ensures the requirement for the differentiability of the estimate everywhere thus invoking a smooth solution.[25] With these penalty terms (Eqs. 3.5 and 3.6) the regularized inverse problem entails finding the elements of change vector δR that minimize the expression:

$$\|\delta d - S\delta R\| + \beta_1 \|\delta R\| + \beta_2 \|L\delta R\| \qquad 3.7$$

Eq. 3.7 thus becomes the augmented objective function.

3.2 The Observed and Calculated Data

The observation and simulated data for ‘saturation’ inversion in most history matching algorithms is the derived quantities of watercut and gas-oil ratio. These quantities constitute the model response and observation data to be matched by the inverse algorithm. These quantities are ratios derived from the phase production rates. There are additional non-uniqueness problems associated with matching ratios and this is one disadvantage of this common approach. In recognition of the fact that well production is princiapally characterized by saturation / saturations at the well node as well as the well flowing pressures, the observation and calculated data in this work are saturation components based on the three-phase black oil saturation equations in streamline coordinate (Eqs. 2.16 and 2.17). We will term this “saturation inversion”. These saturation quantities are the argument of the time derivative in the equations (S_w / B_w , and $S_g / B_g + R_s S_o / B_o$). It becomes clear that working with these quantities, among other advantages discussed later, sensitivities are easily obtained through a simple manipulation of the underlying equations (Eqs. 2.16 and 2.17). What is not particularly obvious is how these quantities are obtained as they are not reported or measured quantities. This motivates the subject of the discussion in the next section; the transformation of typical production data and simulator response to saturation quantities.

3.2.1 Data Transformation

In formulating the inverse problem for the saturation match in terms of the fundamental quantities characterizing well production, (water and gas saturations), the observed and simulator calculated responses then need to be in terms of saturation. We take advantage of the form of the streamline representation of the black-oil saturation equations in simplifying the problem. As a substitute for the water and gas saturations, we work with the components S_w / B_w , and $S_g / B_g + R_s S_o / B_o$. In essence, instead of matching the derived quantities (water-cut and gas-oil ratio) as is typically the case, in this approach, we match the time variation of the saturation components S_w / B_w, and $S_g / B_g + R_s S_o / B_o$ respectively as a convenient substitute to matching explicitly the time variation of water and gas saturation at the well node.

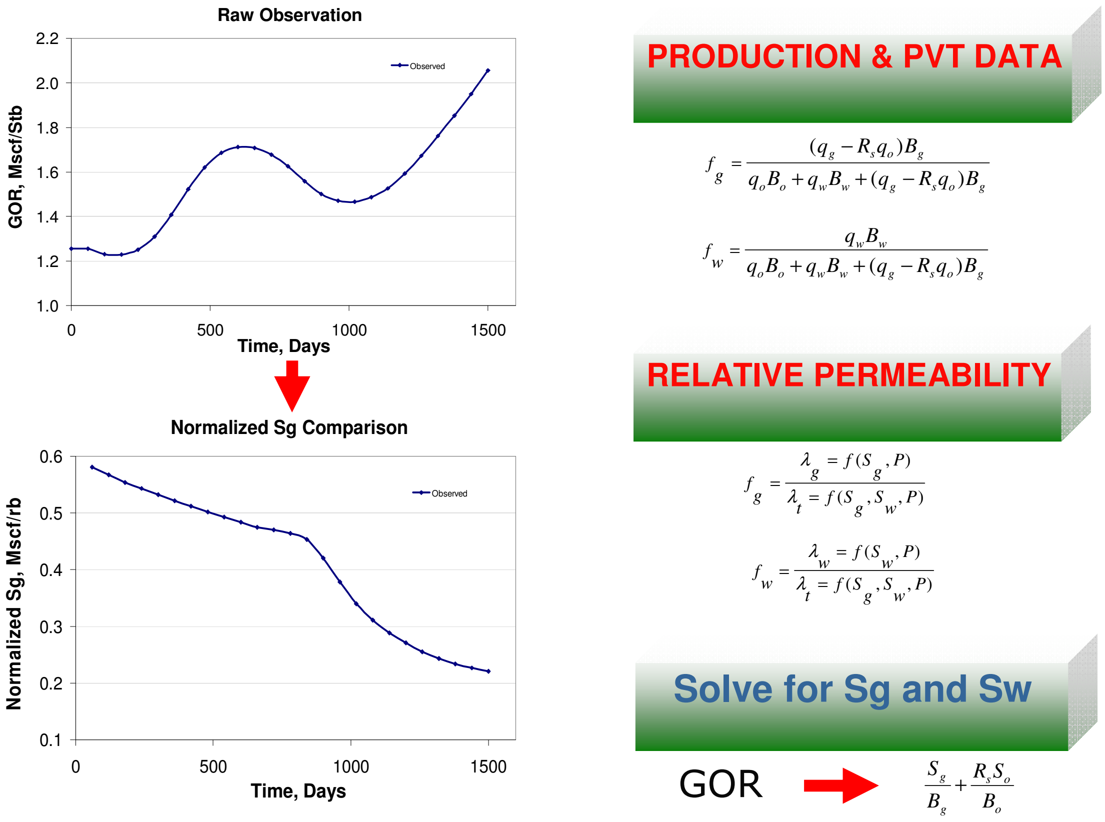

Fig. 3.1 - Transformation of Production Data to Saturation Components

Since the saturations required for computing these quantities are not reported, there is a need to transform production data to saturation (two-phase flow) or saturations (three-phase flow). To be consistent, for the calculated data, the transformation is applied to obtain the equivalent saturation quantities. It is important to note however that while the simulator reported block saturations are adequate to make this transformation for finite-difference applications, in streamline simulation, sub-grid resolution along streamlines makes the block saturation not representative of the saturation quantity characterizing production. For this reason, the transformation operator ($\boldsymbol{T}$) should be applied to both the observed and simulated production rates.

Fig 3.1 shows the basis of the transformation of production data to saturation components. From reported production data, it is possible to compute the fractional flow to both gas and water at reservoir conditions through the equations below:

$$f_g = \frac{(q_g - R_s q_o)B_g}{q_o B_o + q_w B_w + (q_g - R_s q_o)B_g} \quad \ldots\ldots\ldots\ldots\ldots\ldots\ldots\ldots\ldots\ldots\ldots\ldots\ldots\ldots \quad 3.8$$

$$f_w = \frac{q_w B_w}{q_o B_o + q_w B_w + (q_g - R_s q_o)B_g} \quad \ldots\ldots\ldots\ldots\ldots\ldots\ldots\ldots\ldots\ldots\ldots\ldots\ldots\ldots \quad 3.9$$

Approximations to Eqs. 3.8 and 3.9 for finite-difference applications were presented in chapter II for calculated data that offers computational savings.

From the relative permeability relations, the fractional flow can equally be computed for both phases at known gas and water saturations with the expression

$$f_g = \frac{\lambda_g = f(S_g, P)}{\lambda_t = f(S_g, S_w, P)} \quad \ldots\ldots\ldots\ldots\ldots\ldots\ldots\ldots\ldots\ldots\ldots\ldots\ldots\ldots \quad 3.10$$

$$f_w = \frac{\lambda_w = f(S_w, P)}{\lambda_t = f(S_g, S_w, P)} \quad \ldots\ldots\ldots\ldots\ldots\ldots\ldots\ldots\ldots\ldots\ldots\ldots\ldots\ldots \quad 3.11$$

where λ_j represents mobility of phase j and λ_t, the total mobility of all phases. It is then possible to determine saturation from eqns. 3.10 and 3.11 if the fractional flows calculated from eqns. 3.8 and 3.9 are imposed. This process in itself is an optimization based on the representation of the three-phase relative permeability relations. An example of the transformation of observed production to saturation components is shown in the Fig. 3.1

For inverse modeling purposes, it is necessary for the transformation operator ***T*** to be bijective (both Surjective and Injective) as a non-unique transformation will result in a match on the saturation components not yielding a corresponding match on the derived quantities, thus compromising the foundations of this approach to history matching. In order to verify this, for a fixed three-phase relative permeability data, at a fixed pressure of 2800 psi, truncated families of fixed water and gas saturations were plotted against the derived quantities (water-cut and gas-oil ratio) and superimposed on each other. Fig. 3.2 shows the bijective nature of the transformation operator

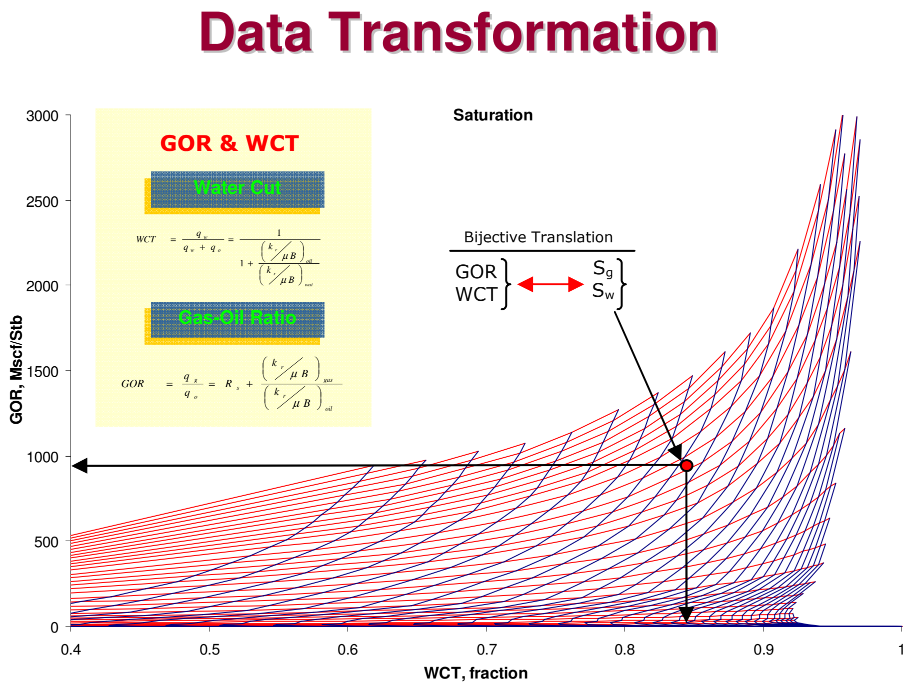

Fig. 3.2 - Unique Translation of Production Data to Water and Gas Saturations

The figure above not only confirms the desired bijective nature of the transformation operator, it also clearly shows that gas-oil ratio (GOR) by itself cannot be used to uniquely determine a pair of saturation (S_g and S_w) and thus for three phase flow, history matching GOR by itself is not sufficient for accurate characterization as seen by the multiplicity of solution shown in Fig. 3.2 Matching both GOR and WCT, however, gives a fixed pair of gas and water saturation as shown in the figure. Based on the bijective property of the operators, it follows that matching the gas and water saturation guarantees a match on both WCT and GOR if the pressure is matched.

To satisfy the requirement of simultaneously matching both gas and water saturation, we match the saturation components (S_w / B_w , and $S_g / B_g + R_s S_o / B_o$) simultaneously as an alternative because of the convenience offered by the form of the saturation equations in streamline coordinates.

Eq. 3.1 can then be rewritten as

$$\sum_{i=1}^{N}\left(T[d_i]-T\left[g_i\left[\vec{R}\right]\right]\right)^2 \quad \ldots\ldots\ldots\ldots\ldots\ldots\ldots\ldots\ldots\ldots \quad 3.12$$

to account for the mapping of production data to saturation components and to make it clear that a transformation operator is applied to typical observation data.

3.3 Data Misfit

Data misfit is generally quantified as the amplitude difference between the observed and calculated data. An inverse problem formulated on the basis of resolving this amplitude difference is termed an amplitude inversion.[16]

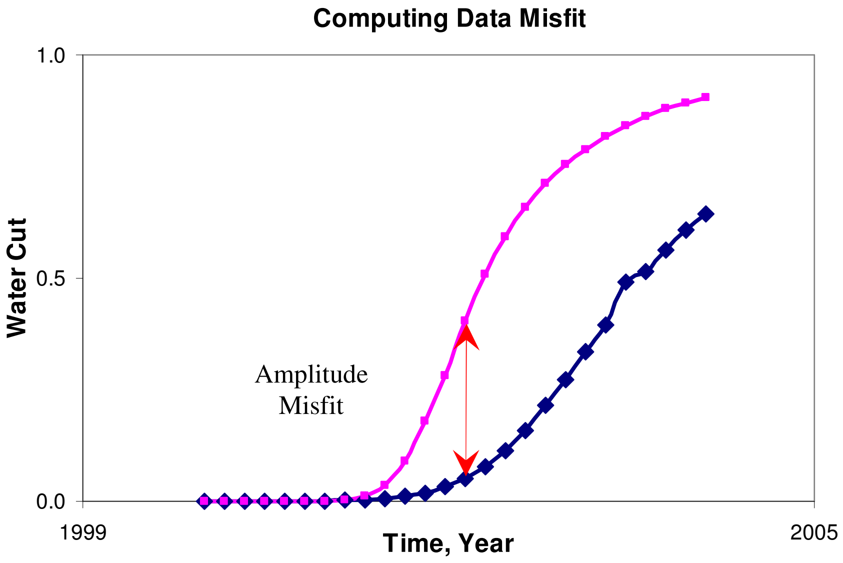

Fig. 3.3 - Quantifying Data Misfit: Amplitude Inversion

A typical watercut profile is shown in Fig. 3.3 highlighting the misfit estimation at a particular observation as the difference between the observed and calculated profiles at the same observation time. The resulting amplitude inversion has been shown to be highly non-linear with poor convergence characteristics.[16]

An alternative to this approach of quantifying data misfit is one analogous to seismic waveform inversion and borrows from efficient methods from geophysical imaging. The resulting inversion is termed a travel-time inversion. In history matching applications, a travel-time inversion is aimed at resolving the difference in the arrival time of fixed saturation fronts or quantities.[1] Fig. 3.4 shows how a travel-time data misfit is quantified.

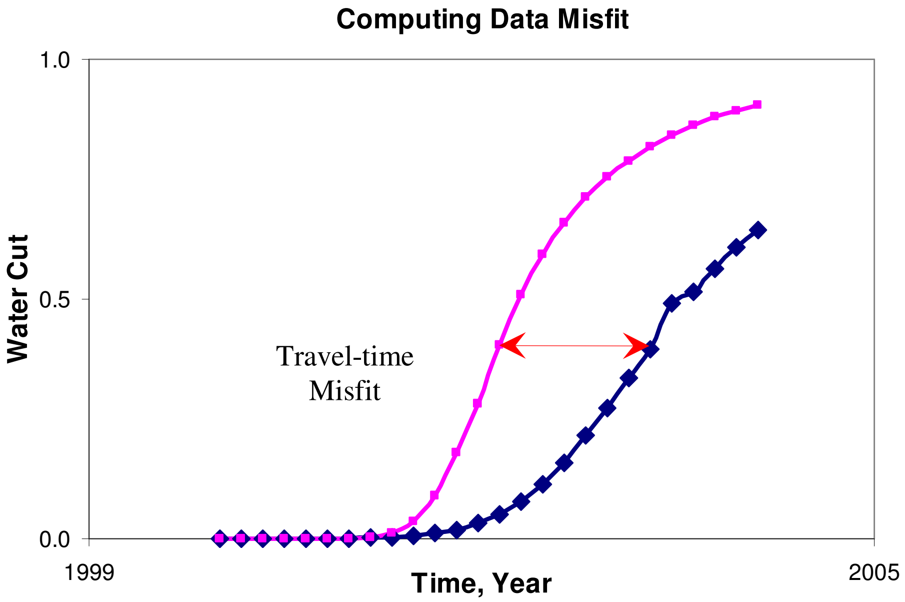

Fig. 3.4 - Quantifying Data Misfit: Travel-time Inversion

In this case, instead of fixing the time and differencing the calculated and observation data at this time as done in the amplitude inversion, what is fixed is the observation while the differencing is done on the time axis. The travel-time misfit thus becomes the difference between the observation time of a fixed saturation on a calculated profile and the observation time of that same saturation on the observation profile.

Travel-time inversion has been shown to be quasi-linear with rapid convergence characteristics.[26] For this reason, this work focuses on travel-time inversion and its elegant variant discussed later.

3.4 Sensitivity Calculations

Simply put, sensitivities represent a linearized relationship between the model parameters and the data. The attraction to sensitivity-based history matching algorithms can be attributed to their quick convergence as compared to other methods.[13] However, what differentiates the different sensitivity-based algorithms from each other is the efficiency with which they compute parameter sensitivities. Streamline-derived sensitivity has proven to be computationally superior to other methods primarily because it is evaluated as one-dimensional integrals along the trajectory of each of the streamlines.

3.4.1 Water Saturation Arrival-time Sensitivity

In computing the arrival-time sensitivity of a fixed saturation to a perturbation in reservoir parameter, the three-phase black oil transport equations introduced in chapter II is utilized. To motivate the derivation for compressible flow, briefly consider the incompressible flow case. The saturation velocity for a given saturation contour S_w along a streamline will be given by,

$$\left.\frac{\partial \tau}{\partial t}\right|_{S_w} = \left.\frac{df_w}{dS_w}\right|_{S_w} \qquad \text{3.13}$$

This follows from the incompressible water saturation equation. The arrival time of the saturation front will be,

$$t\big|_{Sw} = \tau \Big/ \left.\frac{df_w}{dS_w}\right|_{S_w} \qquad \text{3.14}$$

The sensitivity of the saturation arrival time with respect to reservoir parameter *m* is computed as,

$$\left.\frac{\partial t}{\partial m}\right|_{S_w} = \frac{\dfrac{\partial \tau}{\partial m}}{\left.\dfrac{df_w}{dS_w}\right|_{S_w}} \qquad \text{3.15}$$

where the numerator is computed analytically based on the definition of time of flight

$$\tau = \int \frac{\phi}{\left\|\vec{u}\right\|} \delta r \qquad \text{3.16}$$

with the reservoir parameter m embedded in the Darcy velocity $\vec{u}$.

We can generalize the sensitivity calculations using the water saturation equation for compressible flow along a streamline, Eq. 2.16 which can be rearranged as follows,

$$\frac{\partial}{\partial t}\left(\frac{S_w}{B_w}\right) = -\frac{\partial}{\partial \tau}\left(\frac{f_w}{B_w}\right) - \frac{c}{\phi}\frac{f_w}{B_w} \quad \text{.......................................} \quad 3.17$$

In travel time inversion of production data, we are interested in obtaining the partial derivative of the arrival time of saturation with respect to reservoir parameters, m for example permeability. Let $S_w^{'}$ represent the quantity S_w / B_w in the water saturation equation. This is the fixed saturation quantity at the well node segment of a streamline to which we want to compute the sensitivity. $S_w^{'}$ is functionally dependent on t (the arrival time), τ (the time of flight), and p (pressure). Also, τ and p in turn depend on m. For a fixed $S_w^{'}$, we can express this implicitly as follows,

$$\frac{\partial S_w^{'}}{\partial t}\frac{\partial t}{\partial m} + \frac{\partial S_w^{'}}{\partial \tau}\frac{\partial \tau}{\partial m} + \frac{\partial S_w^{'}}{\partial p}\frac{\partial p}{\partial m} = 0 \quad \text{.......................................} \quad 3.18$$

Since water formation volume factor (B_w) is weakly dependent on pressure, the term $\frac{\partial S_w^{'}}{\partial p}$ could be assumed negligible and Eq. 3.18 reduces to

$$\frac{\partial S_w^{'}}{\partial t}\frac{\partial t}{\partial m} + \frac{\partial S_w^{'}}{\partial \tau}\frac{\partial \tau}{\partial m} = 0 \quad \text{.......................................} \quad 3.19$$

A simple manipulation of Eq. 3.19 gives

$$\left.\frac{\partial t}{\partial m}\right|_{S_w^{'}} = -\frac{\frac{\partial S_w^{'}}{\partial \tau}\frac{\partial \tau}{\partial m}}{\frac{\partial S_w^{'}}{\partial t}} \quad \text{.......................................} \quad 3.20$$

rearranging Eq.2.16 and substituting for the denominator gives the required travel time sensitivity for a fixed $S_w^{'}$.

$$\left.\frac{\partial t}{\partial m}\right|_{S_w^{'}} = -\frac{\dfrac{\partial S_w^{'}}{\partial \tau}\dfrac{\partial \tau}{\partial m}}{\dfrac{\partial}{\partial \tau}\left(\dfrac{f_w}{B_w}\right)+\dfrac{f_w}{B_w}\dfrac{c}{\phi}} \qquad \text{3.21}$$

For incompressible flow, c = 0, B_w is constant and Eq. 3.21 reduces to the familiar formulation for incompressible flow (Eq.3.15). All the terms in Eq. 3.21 can be computed along the streamline. Specifically, $\partial\tau/\partial m$ is computed analytically under the assumption that the streamlines do not shift because of small perturbation in reservoir properties. The remaining partial derivatives are approximated by a backward difference along the streamline.

3.4.2 Gas Saturation Arrival-time Sensitivity

The conservation equation for gas is given in Eq. 2.17. Let S_g' represent the quantity $S_g / B_g + S_o R_s / B_o$. We rewrite Eq. 2.17 in the form below

$$\frac{\partial S_g'}{\partial t} = -\frac{\partial}{\partial \tau}\left(\frac{f_g}{B_g}+\frac{f_o R_s}{B_o}\right)-\left(\frac{f_g}{B_g}+\frac{f_o R_s}{B_o}\right)\frac{c}{\phi} \qquad \text{3.22}$$

Considering this quantity S_g' at the well node, it depends on t (the arrival time) and τ (the time of flight), and p (pressure). For a fixed value of S_g', we can express this dependence implicitly as follows,

$$\frac{\partial S_g^{'}}{\partial t}\frac{\partial t}{\partial m}+\frac{\partial S_g^{'}}{\partial \tau}\frac{\partial \tau}{\partial m}+\frac{\partial S_g^{'}}{\partial p}\frac{\partial p}{\partial m}=0 \qquad \text{3.23}$$

Unlike the case of water saturation arrival-time sensitivity, S_g' has a strong dependence on pressure as it contains solution gas-oil ratio and gas formation volume factor (B_g) terms, both of which are strongly pressure dependent. That being noted, in the saturation sensitivity calculation, we do not account explicitly for this pressure dependence. In chapter V, we introduce an approach to pressure inversion that accounts for this assumption and we revisit the formulation presently presented. Neglecting the last term in Eq. 3.23, we have

$$\left.\frac{\partial t}{\partial m}\right|_{S_g'} = -\frac{\dfrac{\partial S'_g}{\partial \tau}\dfrac{\partial \tau}{\partial m}}{\dfrac{\partial S'_g}{\partial t}} \qquad \text{3.24}$$

Rearranging Eq. 2.27 and substituting for the denominator gives the arrival-time sensitivity to a fixed S'_g

$$\left.\frac{\partial t}{\partial m}\right|_{S_g'} = \frac{\dfrac{\partial S'_g}{\partial \tau}\dfrac{\partial \tau}{\partial m}}{\dfrac{\partial}{\partial \tau}\left(\dfrac{f_g}{B_g}+\dfrac{f_o R_s}{B_o}\right)+\left(\dfrac{f_g}{B_g}+\dfrac{f_o R_s}{B_o}\right)\dfrac{c}{\phi}} \qquad \text{3.25}$$

Again, the parameters needed to compute the partial derivatives are readily available along streamlines. As previously pointed out, the sensitivity derivations have not explicitly accounted for the pressure effects. In fact, as shown in Fig. 3.2, S'_w, and S'_g can only uniquely define watercut and GOR at a fixed pressure. Thus, it is critical to match the BHP along with the saturation components.

3.4.3 Sensitivity Verification

By rearranging Eq. 3.25, it can be shown that the sensitivity is composed of two separate and distinct components. The first being a fractional flow component along the streamlines and the second, a grid component based on the divergence of flux. Fig. 3.5 is a verification of this assertion. In this plot, the GOR sensitivity is computed through numerical perturbation and at the same time the divergence of flux is calculated on the grid for a quarter-five spot model on a 21X21 mesh.

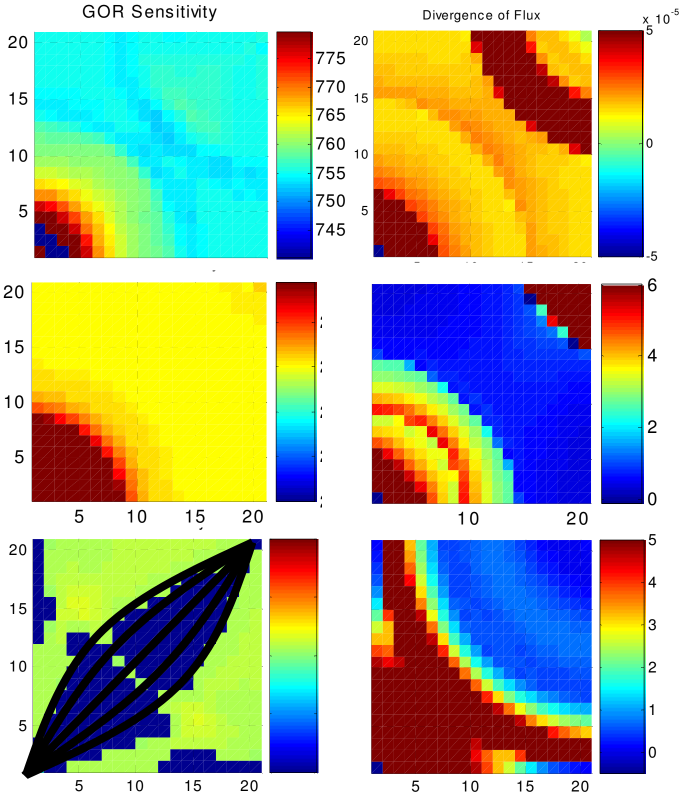

Fig. 3.5 - Verification of Analytical Sensitivities: The Two Components of Sensitivity Dominate at Different Times

Starting form the top of the figure to the bottom, it is clear that we initially have a close resemblance between the GOR sensitivity and the divergence of flux plot and we lose this resemblance descending from the top to the bottom plots. In the bottommost plot, the GOR sensitivity aligns with the trajectory of the streamlines. This observation is suggestive of a transition from the divergence of flux dominated component of the sensitivity to one dominated by the fractional flow component. That the analytical sensitivity formulated is consistent with numerical results verifies the accuracy and thus applicability of the sensitivities for history matching purposes.

3.5 Generalized Travel-time Inversion: GTTI

In section 3.3, the travel-time misfit quantification was presented in comparison to the amplitude approach to quantifying data misfit. In the manner it was presented, to each observation point, the misfit between the calculated and observed profiles is computed on an arrival-time basis. In a variation of this approach, the generalized travel-time inversion quantifies the data misfit by systematically shifting the calculated and observed profiles relative to each other and simultaneously computing the coefficient of correlation corresponding to each shift. For each well, only one misfit is calculated and this corresponds to the shift in the sequence that yields the optimal coefficient of determination.[27, 28] **Fig. 3.6** depicts the optimal shift calculated for a typical water-cut profile.

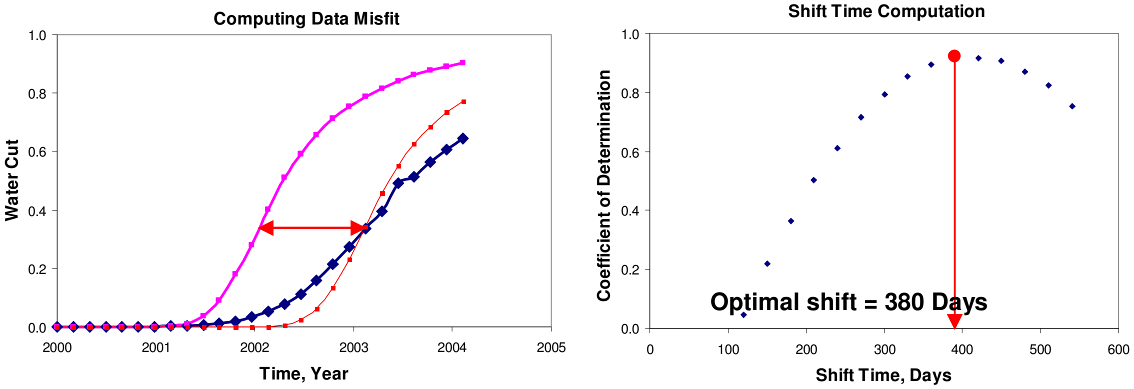

Fig. 3.6 - Misfit Quantification Using Generalized Travel Time

This variation of the travel-time inversion has the advantage that only one misfit needs to be calculated for each well irrespective of the number of observation data. This reduces drastically the size of system of equations to be solved.

3.5.1 GeneralizedTravel-time Inversion: Sensitivity

There are two different ways of computing the sensitivities for a generalized travel-time inversion as applied in this work. The difference between the methods is based on the relative weighting of the arrival-time sensitivity calculated at each observation. In one case, the sensitivity computed for each observation has equal weights and in the other, different weights are applied to the different calculated sensitivities at different observations.

When applying equal weights to the sensitivities calculated at each observation, the generalized travel time sensitivity of each well is calculated by

$$\frac{\partial \Delta \tilde{t}_j}{\partial m} = -\frac{\sum_{i=1}^{N_{dj}} \left(\partial t_{i,j} / \partial m \right)}{N_{dj}} \quad \ldots\ldots\ldots\ldots\ldots\ldots\ldots\ldots\ldots\ldots\ldots\ldots\ldots\ldots \quad 3.26$$

where *i* is the index for the observation data, *j* the index for the well, N_{dj} the number of observation data for well *j,* and $\partial t_{i,j} / \partial m$ the arrival-time sensitivity for a fixed saturation component to a reservoir parameter *m* valid at the i^{th} observation of well *j.*[28]

The second method is a variation of the wave equation travel time inversion after Luo and Schuster.[27] In this approach, a correlation function is defined that relates travel time with production response

$$f(x,\tau) = \int dt \frac{S^{'}(x,t+\tau)_{obs}}{A} S^{'}(x,t)_{cal} \quad \ldots\ldots\ldots\ldots\ldots\ldots\ldots\ldots\ldots\ldots... \quad 3.27$$

where A is a scaling factor that corresponds to the maximum amplitude of the observation data, $S^{'}$ represents fixed saturation components obtained from the transformation operator ***T*** operating on production data. The criterion for the best match is then defined as the travel time residual $\Delta\tau$ that maximizes Eq. 3.27 thus

$$f(x,\Delta\tau) = \max\left\{ f(x,\tau) \middle| \tau \in \left[-T_{\max}, T_{\max} \right] \right\} \quad \ldots\ldots\ldots\ldots\ldots\ldots\ldots\ldots.\ldots \quad 3.28$$

where $T_{\max}$ is the maximum time difference between the observed and calculated profiles of the saturation components. At the optimal shift, the derivative of $f(x,\tau)$ should be zero at $\Delta\tau$ unless its maximum is at an end point.

$$\dot{f}_{\Delta t} = \left[\frac{\partial f(x,\tau)}{\partial \tau}\right]_{\tau=\Delta\tau}$$

$$= \frac{1}{A}\int dt \frac{\partial S^{'}(x,t+\Delta\tau)_{obs}}{\partial t} .S^{'}(x,t)_{cal} . \frac{\partial t}{\partial \tau}\bigg|_{S^{'}(x,t+\Delta\tau)_{obs}}$$

…………………………..... 3.29

Through the use of the rule of an implicit function derivative, the generalized travel-time sensitivity is obtained as

$$\frac{\partial(\Delta\tau)}{\partial m(x)} = -\frac{\left[\dfrac{\partial\left(\dot{f}_{\Delta\tau}\right)}{\partial(m(x))}\right]}{\left[\dfrac{\partial\left(\dot{f}_{\Delta\tau}\right)}{\partial(\Delta\tau)}\right]}$$

…………………………………………………….… 3.30

where

$$\frac{\partial\left(\dot{f}_{\Delta\tau}\right)}{\partial(m(x))} = \frac{1}{A}\int dt \frac{\partial S^{'}(x,t+\Delta\tau)_{obs}}{\partial t} . \frac{\partial t}{\partial \tau}\bigg|_{S^{'}(x,t+\Delta\tau)_{obs}} . \frac{\partial S^{'}(x,t)}{\partial t} . \frac{\partial t}{\partial \tau}\bigg|_{S^{'}_{cal}} . \frac{\partial \tau}{\partial m(x)}$$

…………………………………………………………………………………… 3.31

and

$$\frac{\partial\left(\dot{f}_{\Delta\tau}\right)}{\partial(\Delta t)} = \int \frac{dt}{A} E$$

…………………………………………………….… 3.32

$$E = \frac{\partial S^{'}(x,t+\tau)_{obs}}{\partial t} . \frac{\partial t}{\partial \tau}\bigg|_{S^{'}(x,t+\tau)_{ob}} \frac{\partial S^{'}(t)_{cal}}{\partial t} + S'(t)_{cal} \frac{\partial^2 S'(x,t+\tau)}{\partial \tau^2}$$

………….. 3.33

hence,

$$\frac{\partial(\Delta\tau)}{\partial m(x)} = -\int dt \frac{\dfrac{\partial S^{'}(x,t+\Delta\tau)_{obs}}{\partial t} \dfrac{\partial t}{\partial \tau}\bigg|_{S^{'}(x,t+\Delta\tau)_{obs}} . \dfrac{\partial S^{'}(x,t)}{\partial t} . \dfrac{\partial t}{\partial \tau}\bigg|_{S^{'}_{cal}} . \dfrac{\partial \tau}{\partial m(x)}}{\dfrac{\partial S^{'}(x,t+\tau)_{obs}}{\partial t} . \dfrac{\partial t}{\partial \tau}\bigg|_{S^{'}(x,t+\tau)_{ob}} \dfrac{\partial S^{'}(t)_{cal}}{\partial t} + S'(t)_{cal} \dfrac{\partial^2 S'(x,t+\tau)}{\partial \tau^2}}$$

.... 3.34

$$\frac{\partial(\Delta\tau)}{\partial m(x)} = -\int dt \left\{ \left(\frac{\frac{\partial S'(x,t+\Delta\tau)_{obs}}{\partial t} \left.\frac{\partial t}{\partial\tau}\right|_{S'(x,t+\Delta\tau)_{obs}} \cdot \frac{\partial S'(x,t)}{\partial t}}{\frac{\partial S'(x,t+\tau)_{obs}}{\partial t} \cdot \left.\frac{\partial t}{\partial\tau}\right|_{S'(x,t+\tau)_{ob}} \frac{\partial S'(t)_{cal}}{\partial t} + S'(t)_{cal} \frac{\partial^2 S'(x,t+\tau)_{obs}}{\partial\tau^2}} \right) \left.\frac{\partial t}{\partial m(x)}\right|_{S'_{cal}} \right\} \qquad 3.35$$

Comparing Eq. 3.35 to Eq. 3.26, and noting that the arrival time sensitivity for a fixed saturation to a perturbation in reservoir parameter *m* is $\left.\frac{\partial t}{\partial m(x)}\right|_{S'_{cal}}$, it becomes obvious that the difference in the two representations of the generalized travel time sensitivity at a well is the relative weighting of the sensitivity calculated at each observation. Also, note that the implementation of Eq. 3.35 requires the computation of numerical derivatives along the profiles of the transformed observation and calculated data. This could be problematic for the gas saturation component because of the inaccuracy of gas measurements and thus potentially erratic nature of the resulting profile.

3.6 Amplitude Inversion

Quantifying amplitude data misfit was discussed in section 3.3. The resulting amplitude inversion then requires a consistent sensitivity calculation. The appropriate sensitivity is obtained by applying the chain rule

$$\frac{\partial S'}{\partial m(x)} = \frac{\partial S'}{\partial t} \left.\frac{\partial t}{\partial m(x)}\right|_{S'} \qquad 3.36$$

where the rightmost term is the same as the previously expressed arrival time sensitivity and $\frac{\partial S'}{\partial t}$ is obtained from the numerical derivative along the profile of *S'* vs *t*. It is interesting to note that Eq. 3.35 contains the components of the amplitude sensitivity easily explaining why the amplitude is resolved during the generalized travel-time inversion. Same interpretation can be extended to Eq. 3.26 with the understanding that the amplitude term of Eq. 3.36 ($\frac{\partial S'}{\partial t}$) is constant for all observations in this formulation compared to the preferential weighting applied in Eq. 3.35. Thus we see that the amplitude is equally resolved through the generalized travel-time inversion technique.

3.7 Minimizing the Linear System of Equations

The formulation of the inverse problem as described then results in the solution of a least-squares problem at each iteration. The least-squares problem is characterized by the form shown in Eq. 3.37

$$\min_{x \in \Re^n} \|b - Ax\|, \quad A \in \Re^{mxn}, \; b \in \Re^m, \, m \geq n \qquad \text{3.37}$$

Where A represents the stacked matrix of the sensitivities and the regularization terms, b the vector of calculated misfit and x, the change vector of reservoir parameters needed to update the current estimate of these parameters. For the minimization, we use LSQR (Paige and Saunders, 1982), a particular implementation of the conjugate gradient method applied to normal equations associated with Eq. 3.37. With the Lanczos bidiagonalization algorithm being the core of LSQR, it is an extremely efficient method for the solution of large linear systems of equations and least-squares problems.

3.8 Chapter Summary

In this chapter, an approach to history matching three phase production data has been presented. The approach is unique in that it is formulated on matching the fundamental quantities that characterize production at the well as opposed to the derived quantities of WCT and GOR. A transformation of production data to saturation components that facilitate this saturation inversion is also presented. This transformation clearly highlights the role of pressure and relative permeability in history matching. The formulation of both travel-time and amplitude sensitivity coefficients for water and gas saturation components is discussed in details and the relationship between travel-time and amplitude inversion is explained. The superior convergence characteristic of travel-time inversion over the amplitude inversion earlier shown by previous authors for two phase application is shown to be valid for three phase applications. In the formulation of sensitivity expression for the saturation components, the pressure dependent component is assumed negligible. This is accounted for through a joint saturation and pressure inversion discussed in chapter V.

In the next chapter, the application of the concepts presented here is shown for both synthetic and field applications.

CHAPTER IV

SATURATION INVERSION

In the previous chapter, for three phase history matching, it was established that we need to match three variables (water saturation, gas saturation, and flowing bottom-hole pressure) in order to match production data. For two phase oil-water flow, the problem reduces to matching two variables (water saturation, and flowing bottom-hole pressure). The inverse problem formulated thus far and the sensitivity components discussed relates to saturation inversion. At this point, it is assumed that merely honoring the reservoir voidage for instance is adequate to reproduce the reservoir energy and sufficient for the ensuing saturation inversion to result in a match on production data.

In this chapter, the saturation inversion concepts introduced is validated through application to both synthetic and field cases.

4.1 Two Dimensional Synthetic Case

The synthetic case is a two-dimensional reservoir model with an inverted nine-spot pattern waterflood.

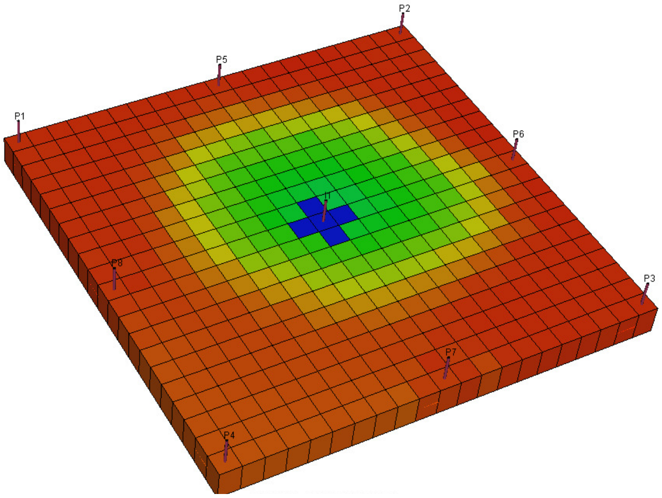

Fig. 4.1 - Synthetic Two Dimensional Inverted Nine-Spot Model

The model consists of eight producers located at the sides and corners of the model and an injector in the center. The model is a three phase black oil model with both solution and free gas existing in the reservoir. The computational domain is on a 21X21X1 mesh. The reservoir is at a depth of about 1000 ft and has an initial pressure of 3000 psi. the pressure-volume-temperature relations is modeled by the curves shown in Fig. 4.2 and rock-fluid data is modeled by the oil-water and gas-oil relative permeability data shown in Fig. 4.3. The model does not include property anisotropy and has uniform porosity and a heterogeneous permeability field shown in Fig. 4.4 Water is injected into the reservoir at a rate of 225rb/d and total production from the reservoir is 280rb/d, resulting in a continual pressure drop and thus more free gas in the reservoir in the vicinity of the wells. Production history is available for 1500 days

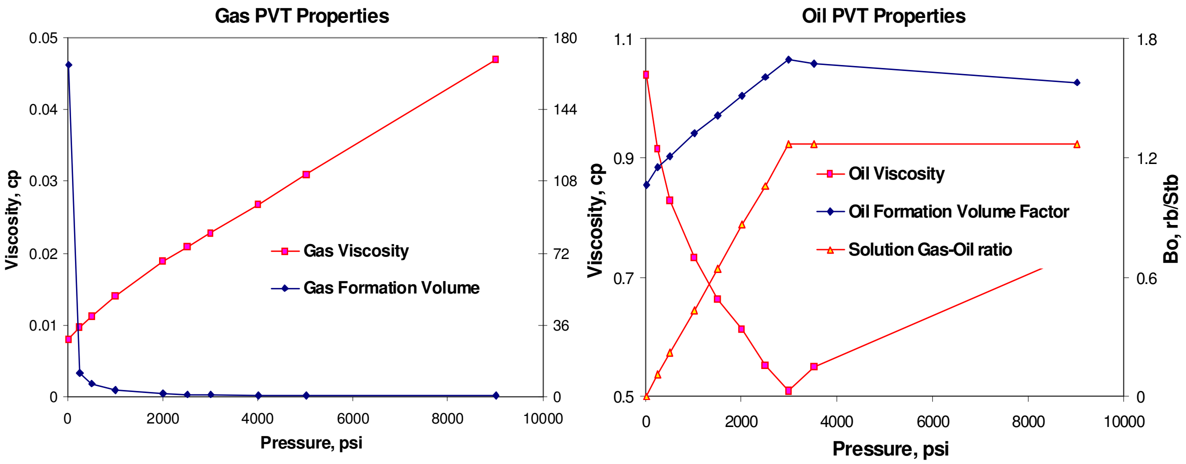

Fig. 4.2 - Oil and Gas PVT Properties

4.1.1 Data Integration: Generalized Travel-Time Inversion

The primary objective is to reconstruct the underlying permeability field by matching the composite saturation components (S_w / B_w , and $S_g / B_g + R_s S_o / B_o$) based on the inverse formulation presented in chapter III. Matching observed production data is based on the premise that a match on the saturation components results in a match on GOR and WCT provided the pressure match is reasonable.

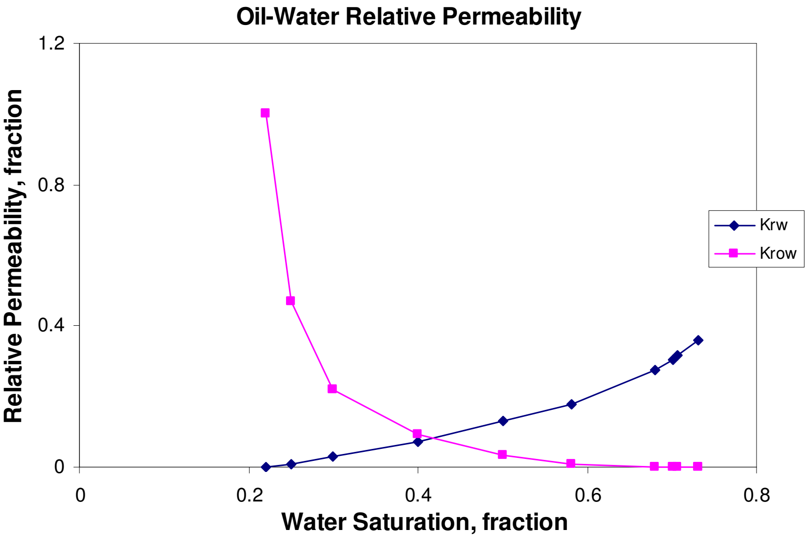

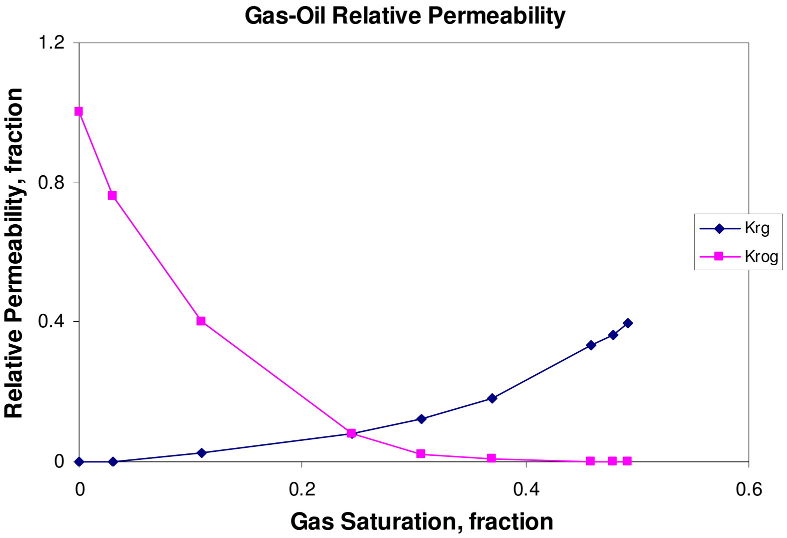

Fig. 4.3 - Three-Phase Relative Permeability Data

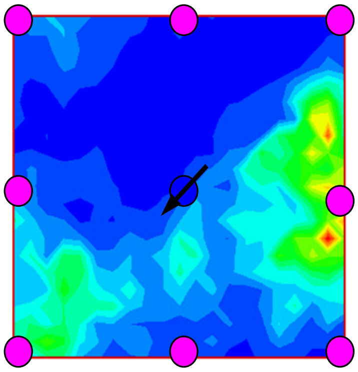

Fig. 4.4 - Reference Permeability Field

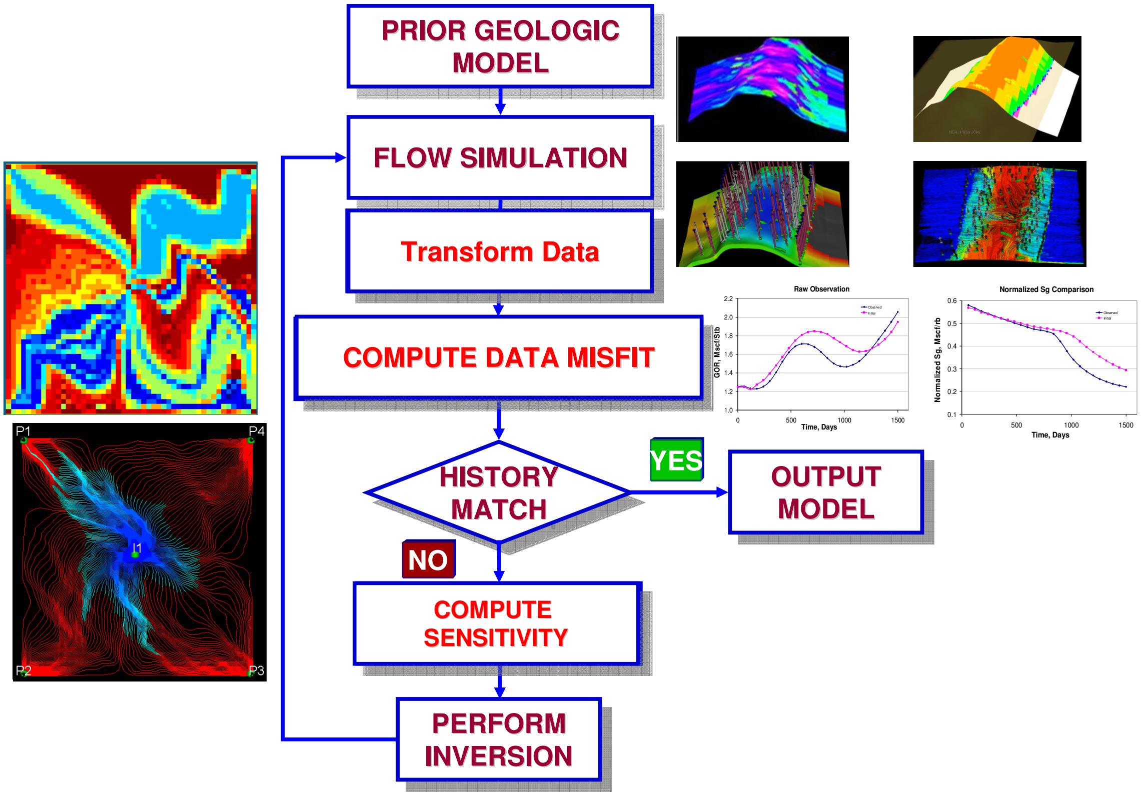

Fig. 4.5 - Workflow for Saturation Inversion

In this case, all variables are assumed known except the permeability distribution. A schematic of the inversion algorithm is shown in Fig. 4.5 where all the components have been discussed previously.

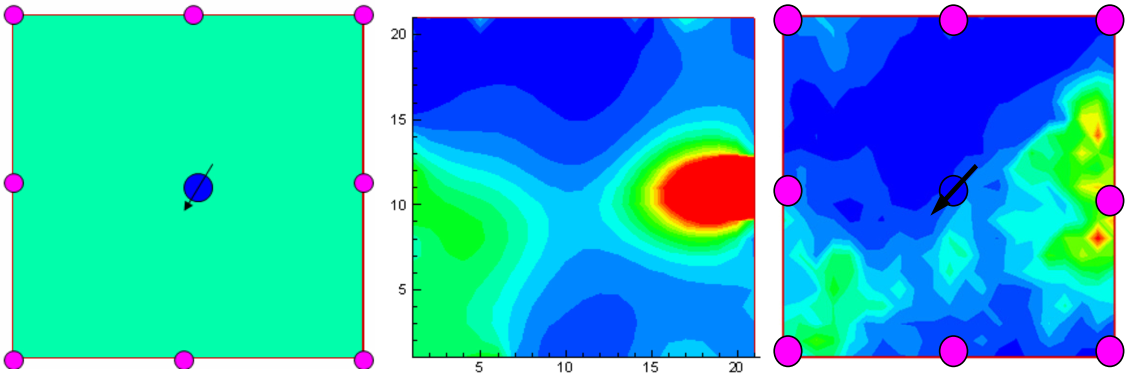

Fig. 4.6 - Initial (left), Reconstructed (Center) and Reference Permeability Field

Starting with a homogenous permeability field as the initial model and proceeding with the simultaneous inversion of the composite saturation quantities, Fig. 4.6 shows the reconstructed permeability field after the inversion. The plot indicates that the data integration has correctly identified the locations of the highs and lows. The reconstructed model is however very “smooth” compared to the reference permeability field due to the smoothness constraint imposed on the solution as part of the regularization. This match is obtained in seven iterations after which all misfit indices have dropped significantly
(Fig 4.7)

The match on the saturation components is shown in the first two columns of Figs. 4.8a & b for the eight producers included in the model. Also shown in the two plots is the corresponding match on the derived quantities (GOR and WCT). In some cases, a match on the saturation components is more precise than the corresponding match on the derived quantities. Whenever this is the case, the difference is primarily due to a difference between the well flowing pressure and the observed pressure thus indicating a need to match the reservoir pressure for the saturation match to translate to a complete match of the derived quantities. However, the weak dependence of water formation volume factor on pressure makes the match on water saturation component result in a seemingly precise match on the WCT profile. Because of the pressure sensitivity of solution gas-oil ratio (R_s), gas formation volume factor (B_g), and thus gas saturation component ($S_g^{'}$), in the absence of a pressure match, a match on the gas saturation component will generally result in discrepancies between the observed and matched GOR data. This difference is seen in the plots shown earlier. A comparison of the reference and simulated pressures after the inversion at the producers is shown in Fig. 4.9.

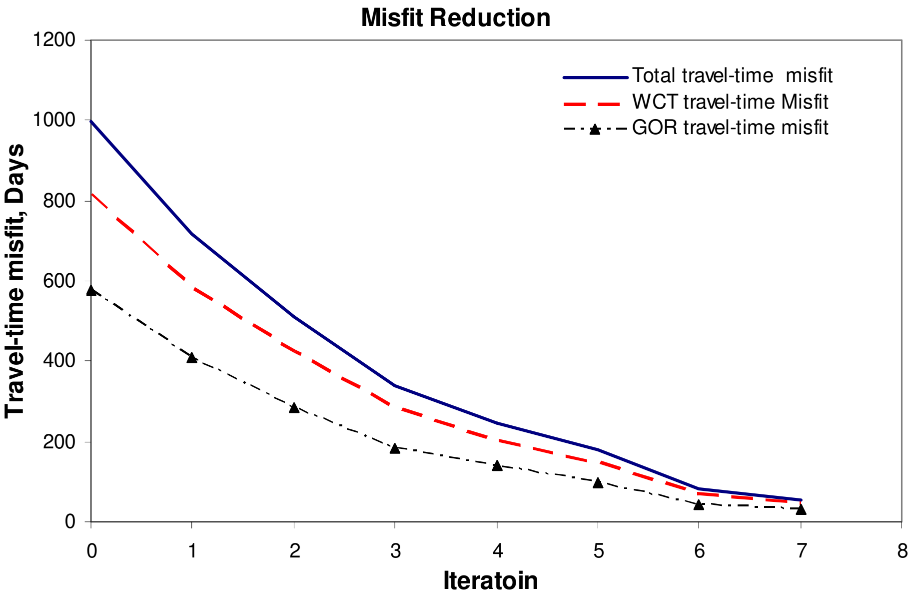

Fig. 4.7 - Misfit Reduction: Synthetic Inversion

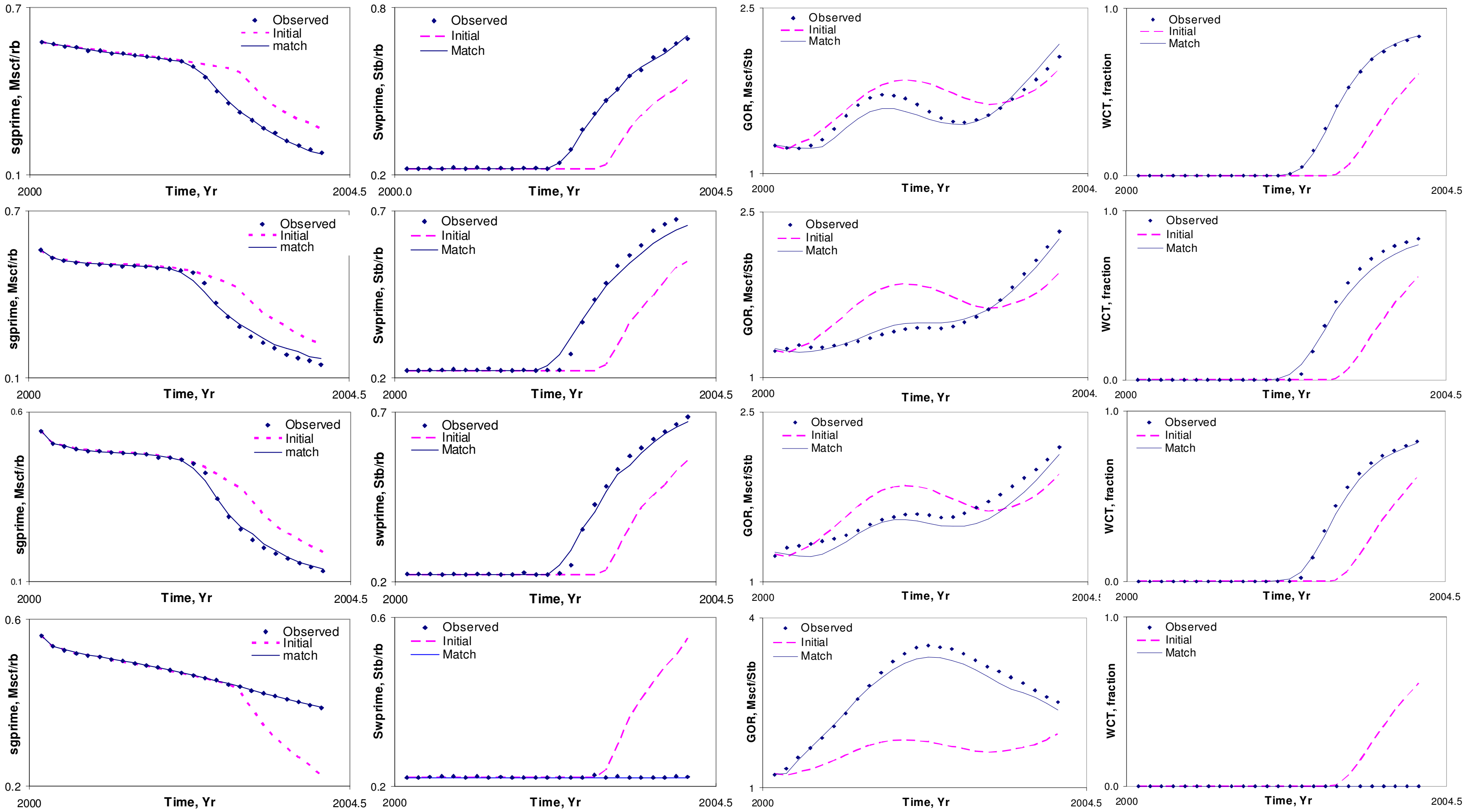

Fig. 4.8a - Match on Composite Saturation Quantities (Columns 1 & 2) and Resulting Match on GOR and WCT (Columns 3 & 4) (Wells 1- 4)

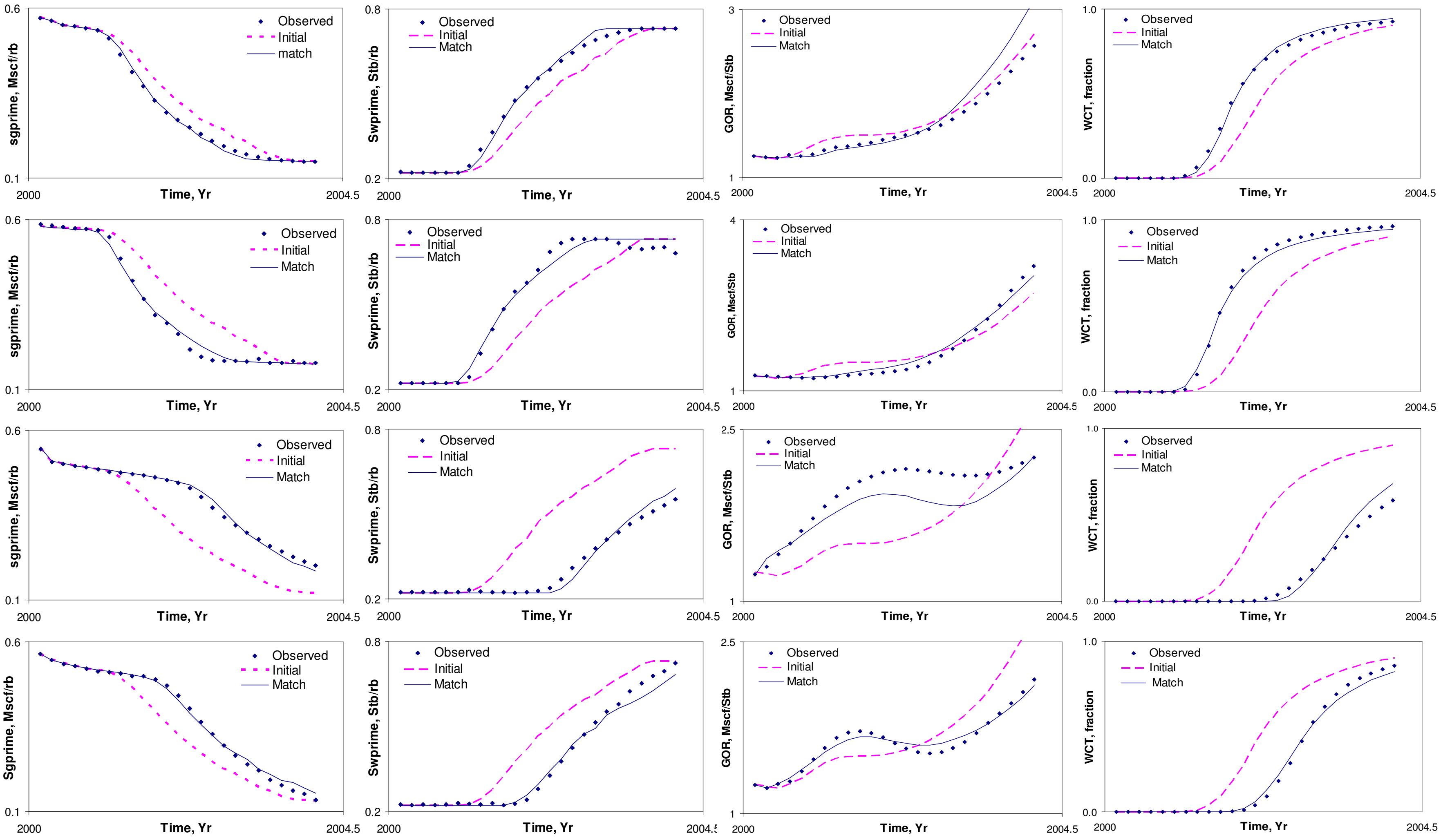

Fig. 4.8b - Match on Composite Saturation Quantities (Columns 1 & 2) and Resulting Match on GOR and WCT (Columns 3 & 4) Wells(4-8)

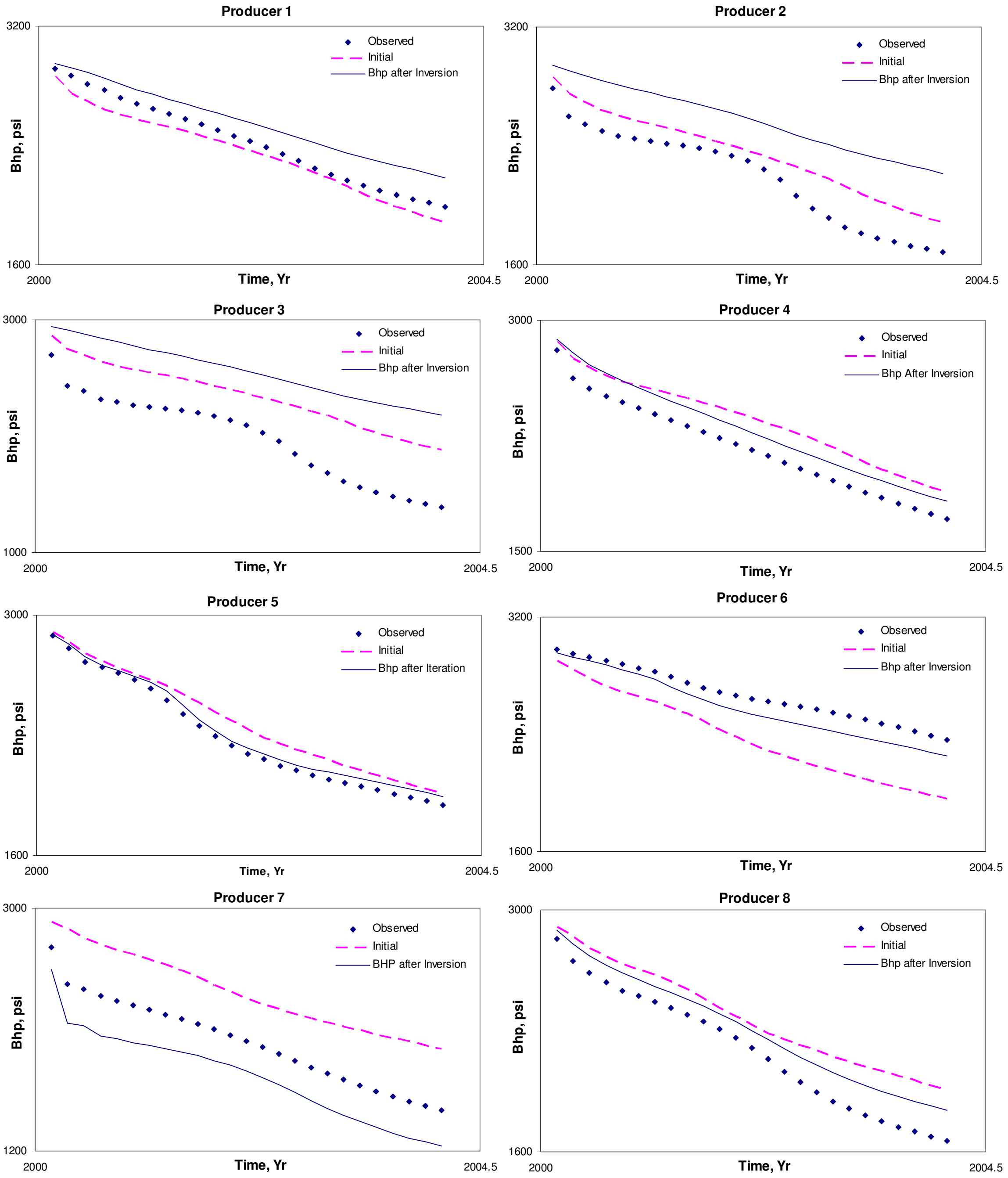
Producer 1

Producer 2

Producer 3

Producer 4

Producer 5

Producer 6

Producer 7

Producer 8

Fig. 4.9 - BHP Comparison after Saturation Inversion Only

The difference seen between the observed and calculated BHP profiles accounts for the slight mismatch in the GOR match even when the gas saturation component is matched precisely.

The validation of the presented concept with this synthetic case clarifies the basis of the approach, which is a decoupling of the history matching problem to saturation and pressure inversion. As it is evident from the results, a representative and thus reliable history match is obtained only when both the saturation and pressure components are resolved.

While the match on BHP is inadequate after the saturation inversion, it is note worthy that in some of the wells (wells 4-8), the saturation inversion tries to resolve the pressure difference between the reference and simulated (based on reconstructed model) BHP profiles. This difference is due largely to the fact that the sensitivity to the saturation components is approximate because we have neglected the pressure component of the saturation sensitivity (Sections 3.4.1 & 3.4.2).

4.1.2 Data Integration: Amplitude Inversion

In the previous section, the data integration was based on the generalized travel-time formulation. In section 3.5, this approach to data integration was discussed and it was emphasized that the objective function has quasi-linear properties with respect to model parameters when the formulation is based on a travel-time inversion, while in comparison the amplitude inversion (section 3.6) is highly non-linear with poor convergence characteristics. In this section, this assertion is verified by applying an amplitude inversion on the inverted nine-spot synthetic model.

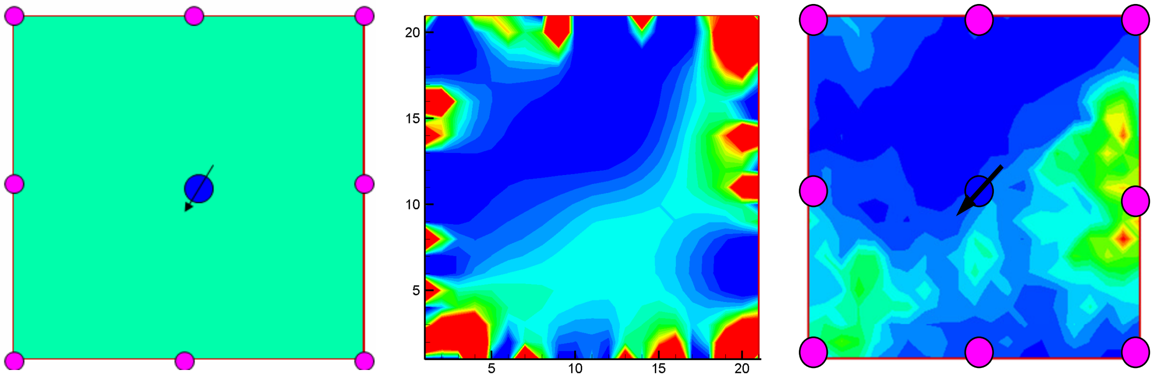

Fig. 4.10 - Amplitude Inversion: Initial (left), Reconstructed (Center) and Reference Permeability Field

The reconstructed permeability field after an amplitude inversion is shown in Fig. 4.10 while the inversion has been able to capture in general, the position of the high and low permeability trend, some numerical artifact is noticed in the reconstructed permeability field unlike what we see in the case of generalized travel-time inversion. This observation is similar to that seen in two phase oil-water model calibration.[16]

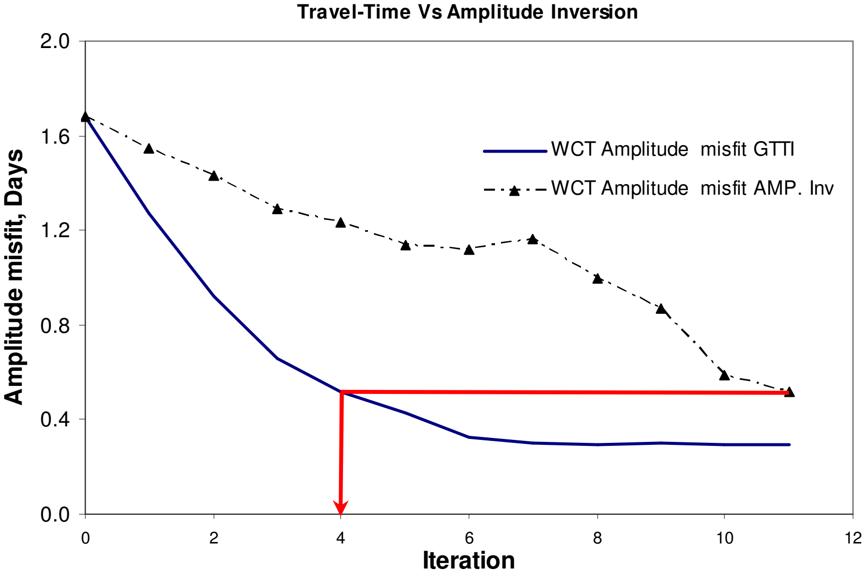

Fig. 4.11a - Comparison of Amplitude and Travel-time Inversion Techniques (WCT)

Comparing the convergence performance of the amplitude and generalized travel-time inversion (Fig. 4.11a & b), the misfit reduction in both plots for the amplitude inversion after eleven iterations is achieved in only four iterations using the generalized travel time inversion technique. A plot of the match on production data and a comparison of the reference and simulated BHP after the inversion is shown in appendix A.

4.2 A Million Cell Two Phase Field Application

The second application is a two phase field case. This is an Asian field with hundreds of wells and about a million grid blocks in the reservoir model. The reservoir model is a sector of a larger field model and consists of a two phase oil-water system with 320 producers and 7 injectors.

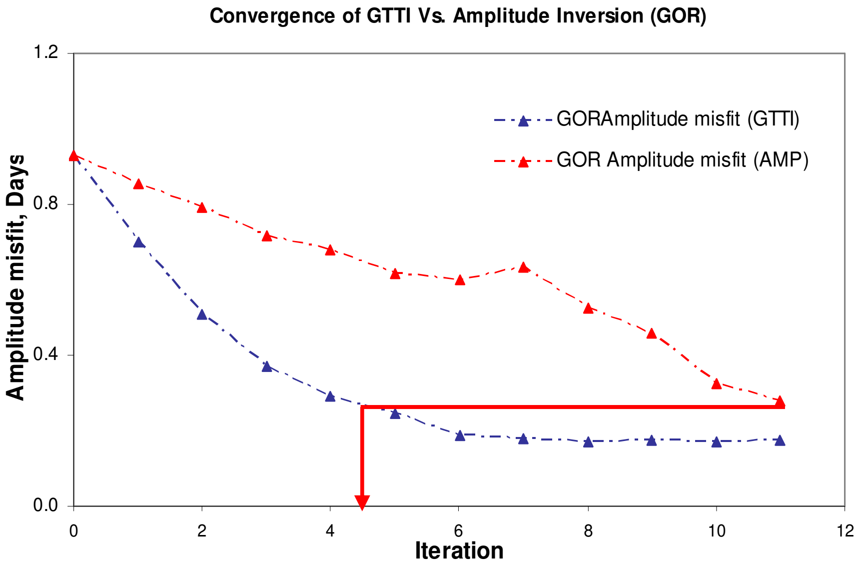

Fig. 4.11b - Comparison of Amplitude and Travel-time Inversion Techniques (GOR)

The dimensions of the field are 25 km by 12 km. The field was discovered in 1944 and oil production began in 1952. Cumulative oil production till date is over four billion barrels. Produced water re-injection commenced in 1970 with pattern waterflood in the crest of the main segment. Present oil production rate is over 100Mstb/d. Rock-fluid interaction is modeled by two normalized relative permeability curves for the twenty five facie types. The first ten facie types use the first relative permeability data and the second relative permeability data set models fluid flow in the other facie types.

Each cell in the model has critical saturations specified based on petrophysical data and accounts for the use of normalized relative permeability data.

The field came into production early in 1952 and has over 50 years of production history to be integrated in the model calibration exercise. The primary purpose for the history match is to assess the performance of a surfactant flood in a region of the model and the discretization of the simulation domain was designed accordingly. The finer mesh is applied to the center of the model in the proposed surfactant fluid region with coarsening of the mesh away from this region. The model is further divided into five fluid-in-place regions based on field measured average reservoir pressure in these regions. Ultimately, this would serve to clarify regional pressure match.

4.2.1 Production Data Integration

The history match desired in this field case is a match on the field observed watercut and average regional pressures. Since this is a two phase model, based on the discussion in chapter III, the problem reduces to one of matching the water saturation and flowing pressure at each of the wells. In the formulation of the inverse problem, the transformation operator ***T*** was used to convert production data to saturation components as a requirement for consistency between the sensitivity and misfit calculation. In the two phase oil-water case, a simplification can be made in which case the transformation step is skipped. The reason being that for this case, since the watercut is the same as the water fractional flow and the water saturation uniquely determines the fractional flow, the fractional flow profile (f_w Vs. *time*), and thus watercut profile mimics the water saturation profile at the outlet node. In other words, the arrival time of fixed water saturation is the same as the arrival time of the corresponding water fractional flow and in essence, watercut. For this reason, while the sensitivity expression remains the same as presented, for two phase applications, it is sufficient to use the watercut profile to compute the data misfit and skip the transformation step of the algorithm.

On running the initial reservoir model, most of the wells did not have the required pressure support and are shut in once the minimum pressure constraint set for the wells is violated resulting in the simulated average regional pressures falling well below the observed values. Since this is a sector model, the representation of the boundary conditions based on pressure support from peripheral injectors in the full field model was questionable. To address this, pseudo injectors were placed at the boundaries of the sector model where the full field model was thought to be strongly influenced by the peripheral injectors.

The steps followed for the data integration is as follows:

- Include pseudo wells to model boundary conditions and eliminate well control mode switching to BHP constraint
- Constrain model by liquid rate to honor voidage requirement
- Ascertain match on regional pressures
- Constrain model by oil rate for automatic history matching through GTTI

The objective is to match the production data while maintaining a decent match on the regional pressures. Fig. 4.12 shows the match on the observed regional pressures on following the outlined steps.

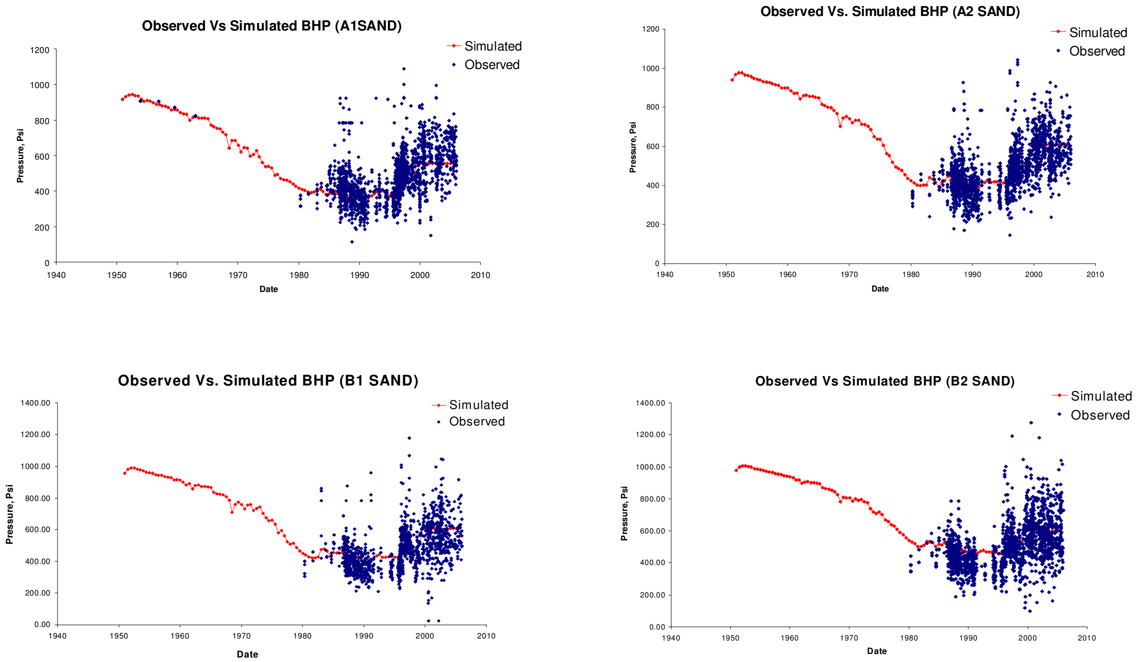

Fig. 4.12 - Regional Pressure Match after Saturation Inversion

In the saturation inversion, more weight was placed on the 57 wells in the surfactant region with the finer grids in order to address the primary purpose of the history match with emphasis on detailed characterization in the area of interest. A plot of watercut on a few of the wells after the saturation inversion is shown in Fig. 4.13. The pre and post inversion permeability models are shown in Fig. 4.14. That the difference between the pre and post inversion models is not very discernable is a result of the imposed norm constraint in the augmented objective function. In this case in particular, after several years of production and with so many producers in the field, the expectation would be that the prior model built from both static and dynamic data integration over the years would be somewhat representative of the underlying geology and thus warrants the preservation of the model.

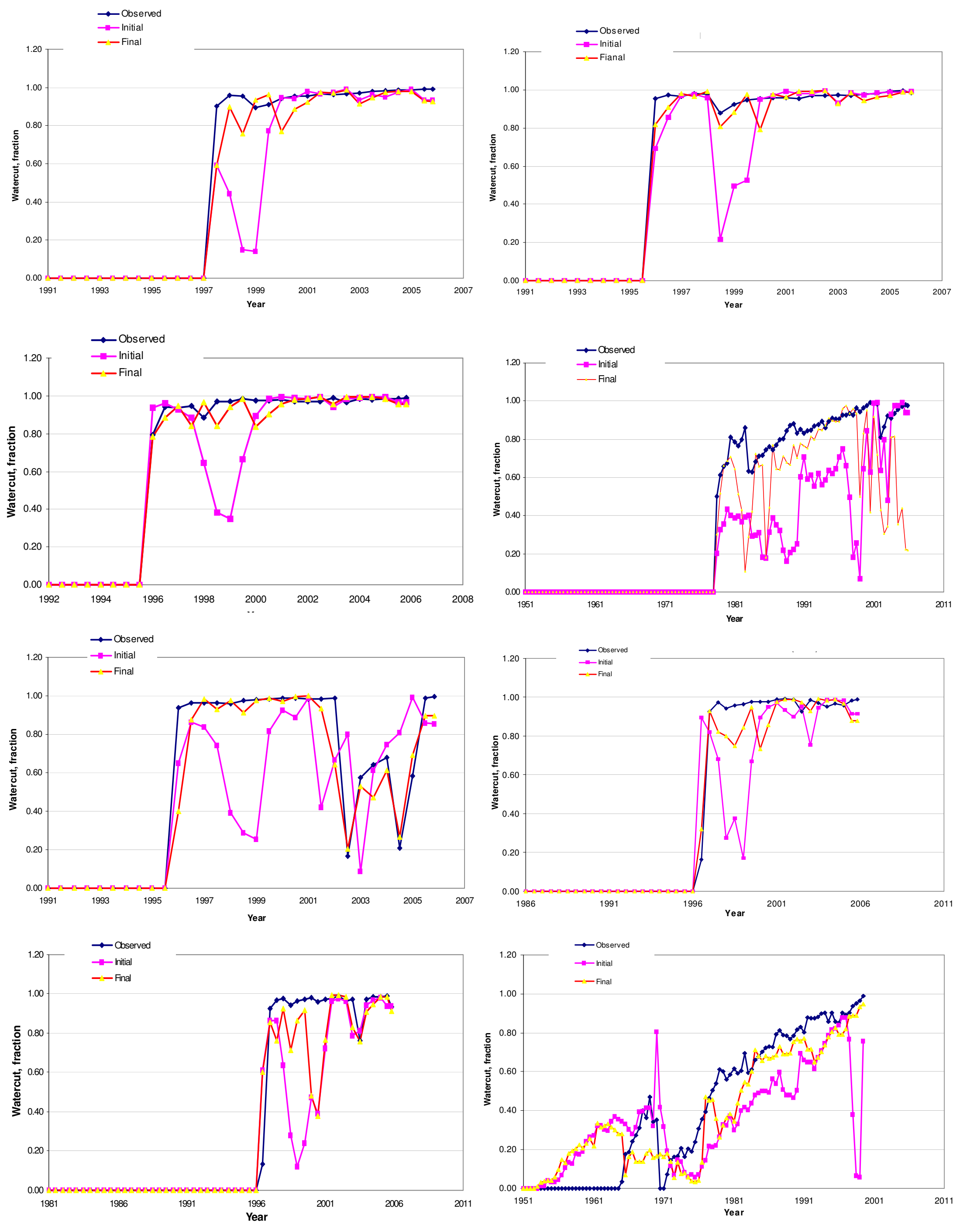

Fig. 4.13 - Saturation Match on Some Wells in Surfactant Fluid Region

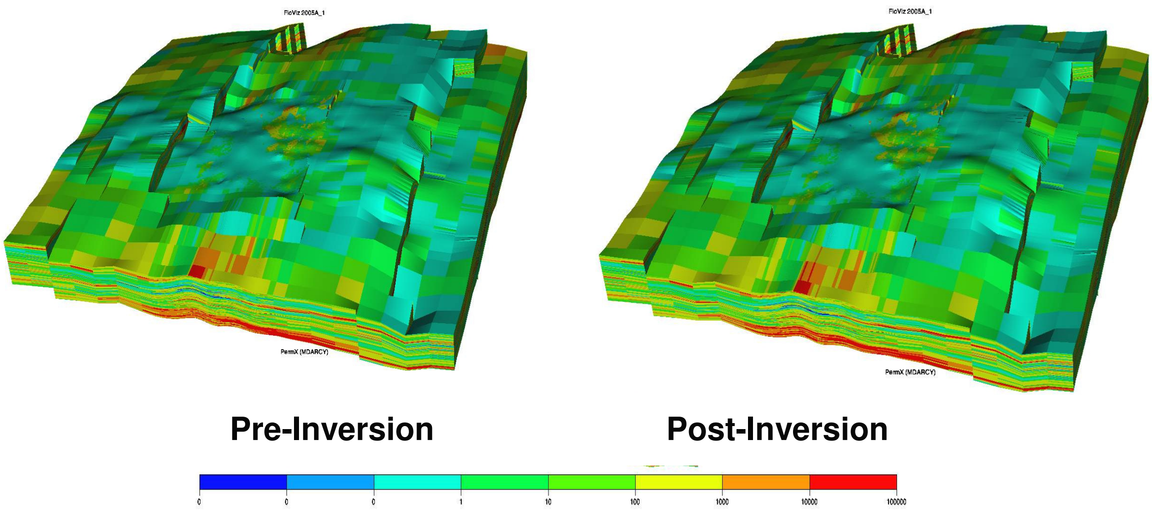

Fig. 4.14 - Preservation of Prior Model after Inversion

A comparison of the pre and post inversion permeability distribution on a layer by layer basis is included in appendix B.

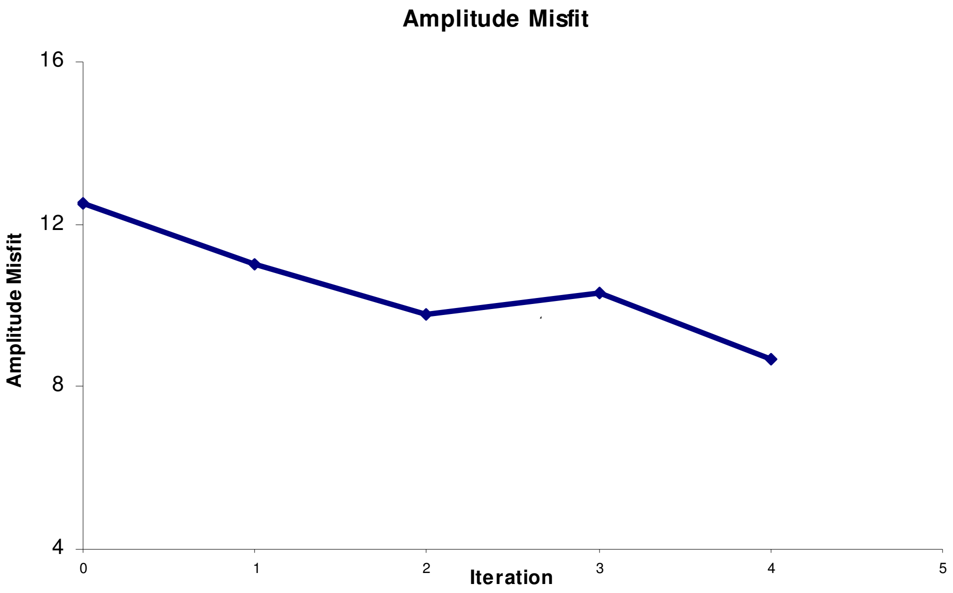

Fig. 4.15 - Slow Convergence of GTTI in the "Vicinity" of the Solution

In the presented match (Fig. 4.13), it is seen that most of the wells already have a reasonable match on water breakthrough and the inversion really needs to resolve the amplitude mismatch between the observed and calculated data.

The match on the first arrival of water by the prior model supports the initial argument about the prior model and the need to preserve it. It was stated in chapter III that in the vicinity of the solution (when the travel-time misfit is minimal), the generalized travel time inversion reduces to an amplitude inversion exhibiting the slow convergence that is characteristic of amplitude inversion. This is verified by the misfit reduction shown in Fig. 4.15. In this figure, the convergence is not as rapid as is typically the case because the travel time misfit has been mostly resolved in the prior model and the inversion is essentially resolving the amplitude misfit.

4.3 Three Dimensional Three Phase Synthetic Case: Ninth SPE Comparative Study

The synthetic case considered in this section is a slightly modified version of the ninth SPE comparative study. The reservoir (Fig. 4.16) is represented by a 24X25X15 mesh with rectangular coordinates. The dimensions of the grid blocks are 300 feet in both the X and Y directions. Cell (1,1,1) is at a depth of 9000 feet sub sea at the center of the cell top. The remaining cells dip in the x-direction at an angle of 10 degrees. Values of porosity and thickness can be found in the paper by Killough. [29]

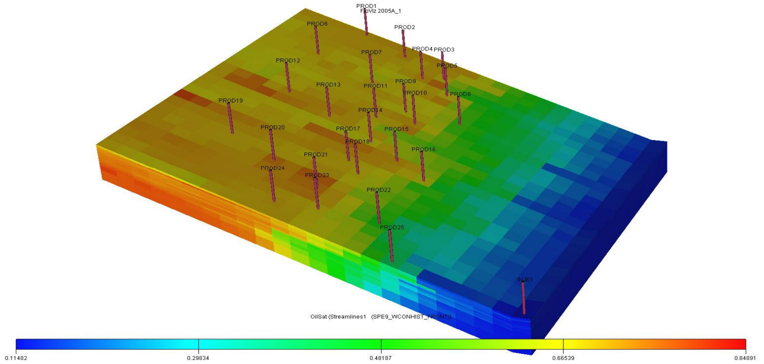

Fig. 4.16 - Field-Scale Synthetic Case: Modified SPE9 Model

The total thickness from Layers 1 to 13 is 209 feet(16 feet per layer in average)., and Layers 14 and 15 have thickness of 50 and 100 feet respectively. Fluid properties and relative permeability data are the same as provided for the comparative study. The reference permeability field is that provided by SPE and it is used to generate the ‘observed’ production history. A total of one water injector and 25 producers were included in the simulation model. The injector was completed from layers 1 through 11. All producers excepting producers 8, 16, 22, and 25 are completed in layers 1 through 13. These producers are completed in layers 1 through 5 to avoid completion in the water leg. An initial model which serves as a prior in this case was generated geostatistically as a random realization of a sequential Gaussian simulation based on variograms generated using control points at the well location.

4.3.1 Data Integration

Since this is a three phase application, where both water and gas saturation are needed to characterize GOR and WCT, the simplification applied to two phase models would not be valid and the fully developed formulation of the inverse problem for three phase flow is followed in the data integration.

Fig. 4.17 shows a comparison of the reference and the BHP obtained on running the geostatistically created prior for some of the 25 producers in the model. The wells shown have been selected to give a fair representation of the spectrum of pressure mismatch for all the wells in the model. While Producers 22 and 25 show a remarkable mismatch, in general, for most of the wells in the model, the simulated BHP based on the prior model was not too far from the reference BHP which at this point is desirable because we have not explicitly accounted for pressure dependence in the sensitivity formulation.

The saturation inversion results in a reasonable match on all the producers in the model. The match on gas and water saturation components as well as the derived quantities of GOR and WCT for those wells in Fig. 4.17 is shown in Fig. 4.18. Like most of the other wells, the match is decent.

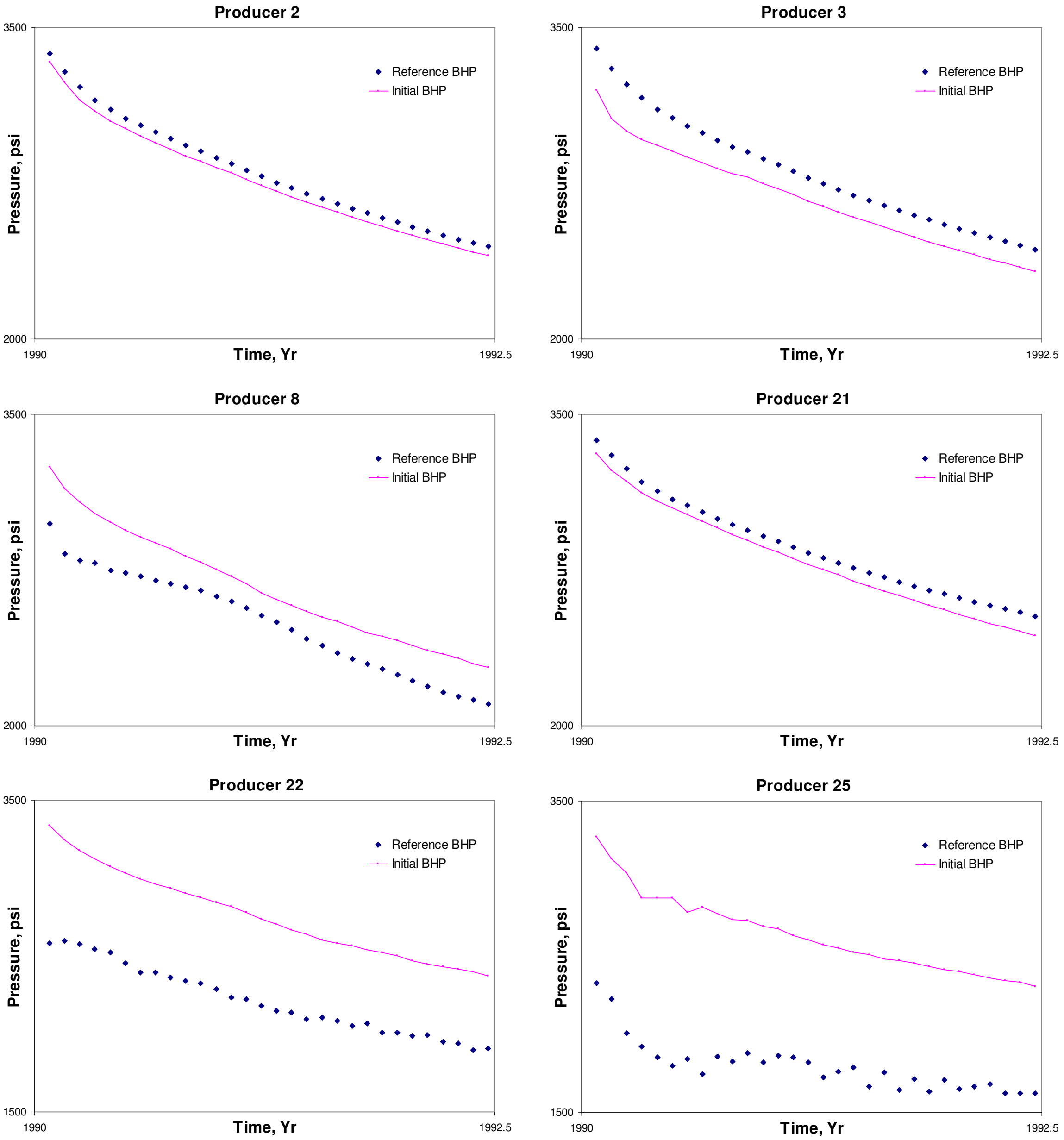

Fig. 4.17 - Comparison of Initial and Reference BHP: Wells Are Selected to Give a Fair Representation of the Spectrum of Pressure Mismatch

4.3.2 Inversion Validation by Layer Basis and Histogram Comparison

Since in this case, we have access to the true permeability field, a more detailed analyses on the results of the inversion is done.

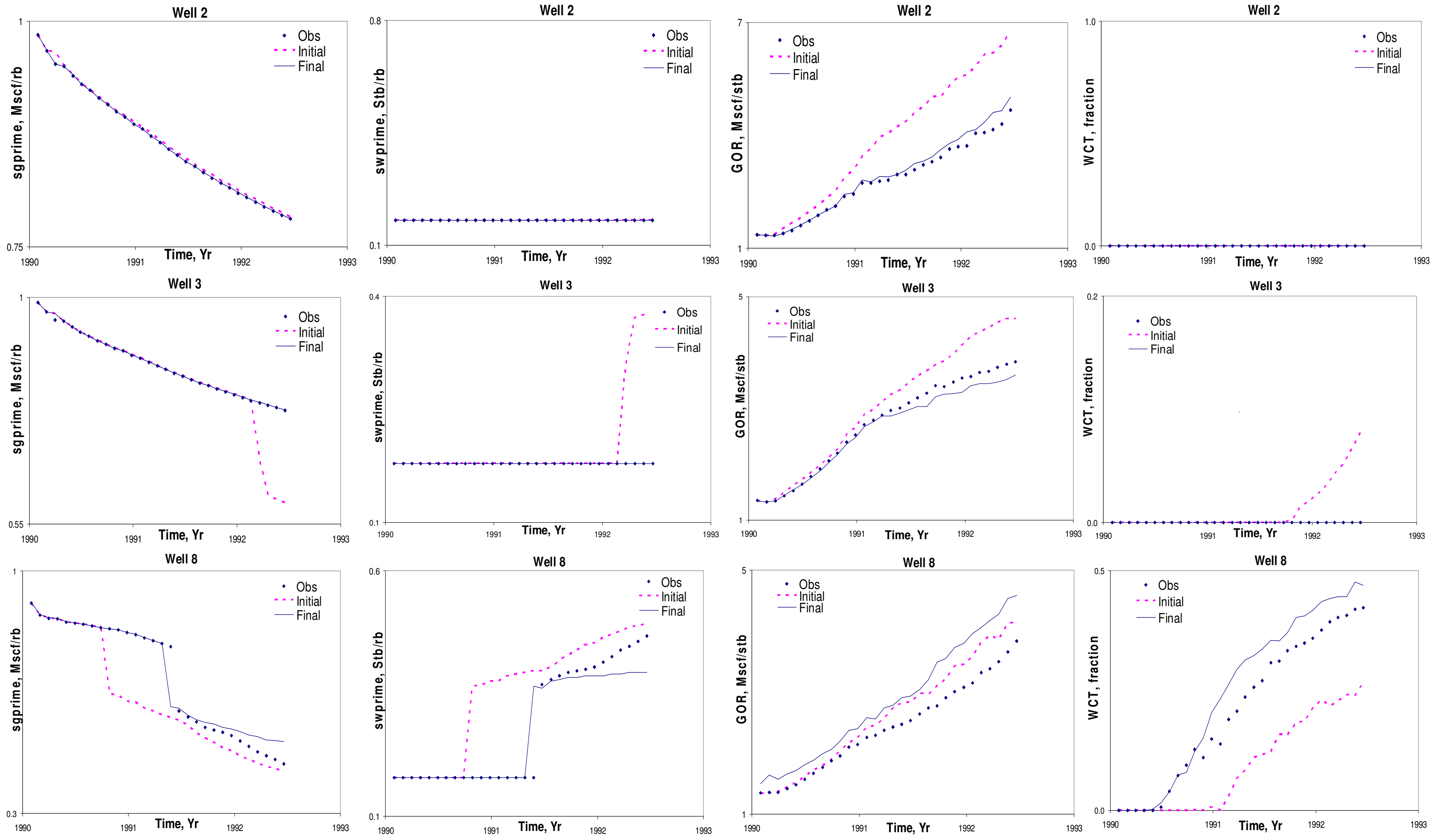

Fig 4.18a - Saturation Inversion Showing a Match on Both Saturation Components and Derived Quantities

(Wells -2, 3, 8)

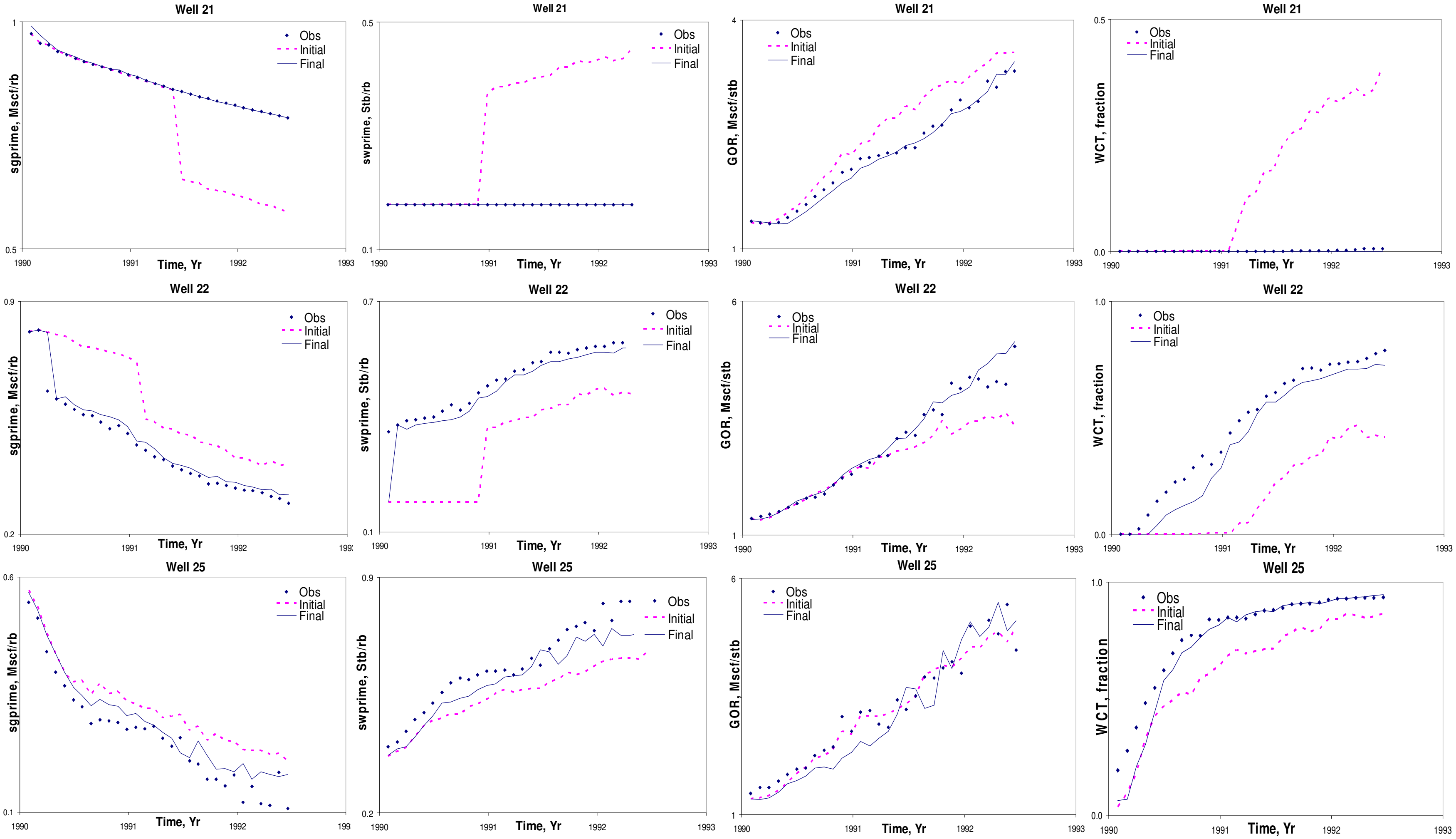

Fig. 4.18b - Saturation Inversion Showing a Match on Both Saturation Components and Derived Quantities (Wells - 21, 22 ,25)

A comparison of the changes made to the initial permeability field (update less initial) to those needed to be made for total reconstruction of the reference permeability field (reference less initial) indicates that directionally, the changes made by the inversion are consistent with the changes needed (Fig. 4.19) for the most part as highlighted by the solid ellipse on the plot.

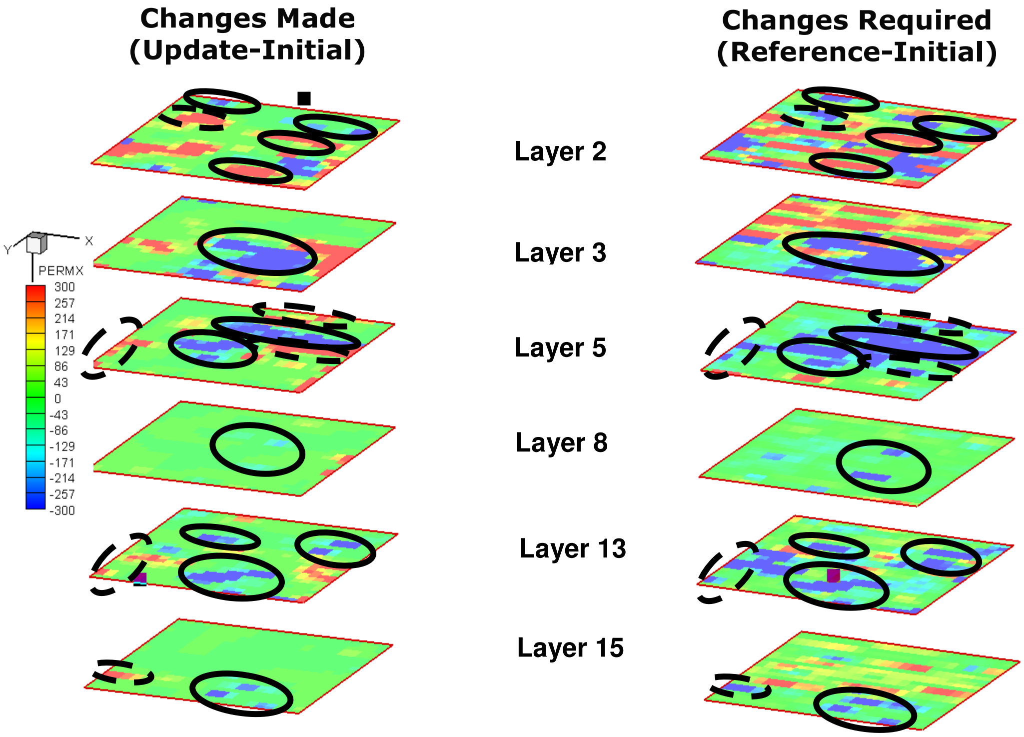

Fig. 4.19 - Comparison of Changes Made to Changes Required: Modified SPE9

In a few other locations (highlighted by dashed ellipse) on the same plot, it is obvious that the changes made are not directionally consistent with those required. The failure of the inversion algorithm to capture the directional change needed in these locations could be due to one or a combination of the following:

- **Lack of layer resolution**: The matched production data for each well is the sum of the contribution from each of the completed layers in the calibrated model. This contribution is known for the simulated data but unknown for the observed “true” model except there is additional data from layer monitoring tools such as a production logging tool (PLT) or distributed temperature sensor (DTS). In the absence of additional data, the non uniqueness exists as to the layer contribution in the matched data.

- **Low streamline density in affected regions:** This is an important factor as it is fundamental to the presented approach to history matching. Sensitivities are calculated along streamlines and these provide the necessary information on the influence of each cell on the production data. Without adequate streamline coverage as seen in stagnant regions of the reservoir, it is believed that the cells are insensitive to production and thus changes are not made
- **Imposed roughness penalty:** The requirement for a ‘smooth’ solution as imposed by the roughness constraint could also be a reason for the discrepancies noticed in the figure.

The initial and updated permeability histograms and statistics are also compared after the inversion (Fig. 4.20). The permeability histogram constructed from the updated permeability field is in general closer to the reference model in terms of statistics and distribution. As a whole, the data integration process for this three phase application has resulted in a satisfactory match on production data and clearly reconstructed the permeability field reasonably accurately.

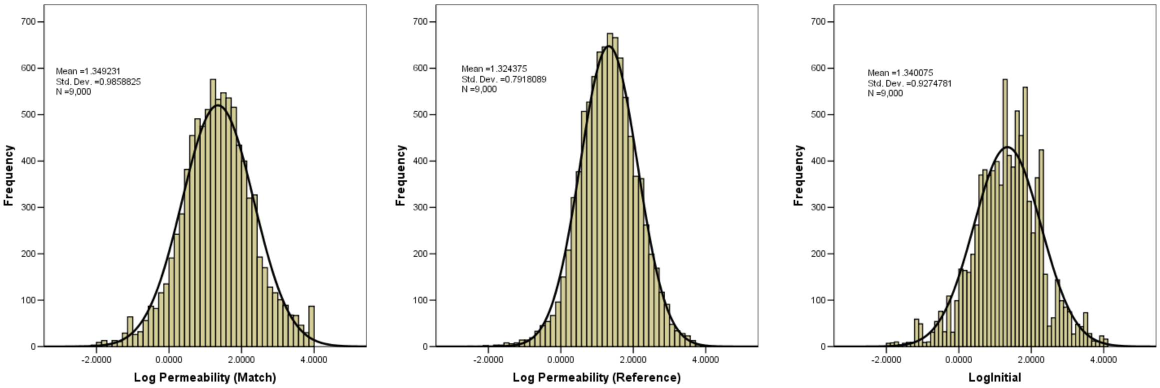

(a). After Inversion **(b) Reference** **(c) Initial**

Fig. 4.20 - Histogram and Statistics of Permeability Field

4.4 High Resolution Field Application

This section highlights the computational efficiency and practicability of the presented approach to reconciling high-resolution geologic model to dynamic data. The application presented is a giant Middle-East field that ranks among the largest hydrocarbon accumulations in the world with over 30 years of production history and hundreds of wells. The field was discovered in 1948 and was put on production in 1951. Peak production from this field was attained in the 80's with production being cut down following depression in the oil industry in the late 80's.

The geologic model was created by a combination of log measurements of porosity, core measured permeability with resulting porosity-permeability transforms, and 3-D seismic information. The facies model consists of seven indicators categorized as dolomitic and non-dolomitic lithologies. The model has over a million cells with a north-east striking anticline.

Initial fluid distribution is based on capillary-gravity equilibrium requirements with the Leverett-J function for individual facies used to model capillary pressure-saturation relations. The oil-water contact has a northeasterly dip of over 660 feet with an associated tar mat. To maintain the reservoir pressure water injection wells are completed at the flanks of the anticline structure above the tar mat. The water saturation after initialization for some of the layers is shown in Fig. 4.21.

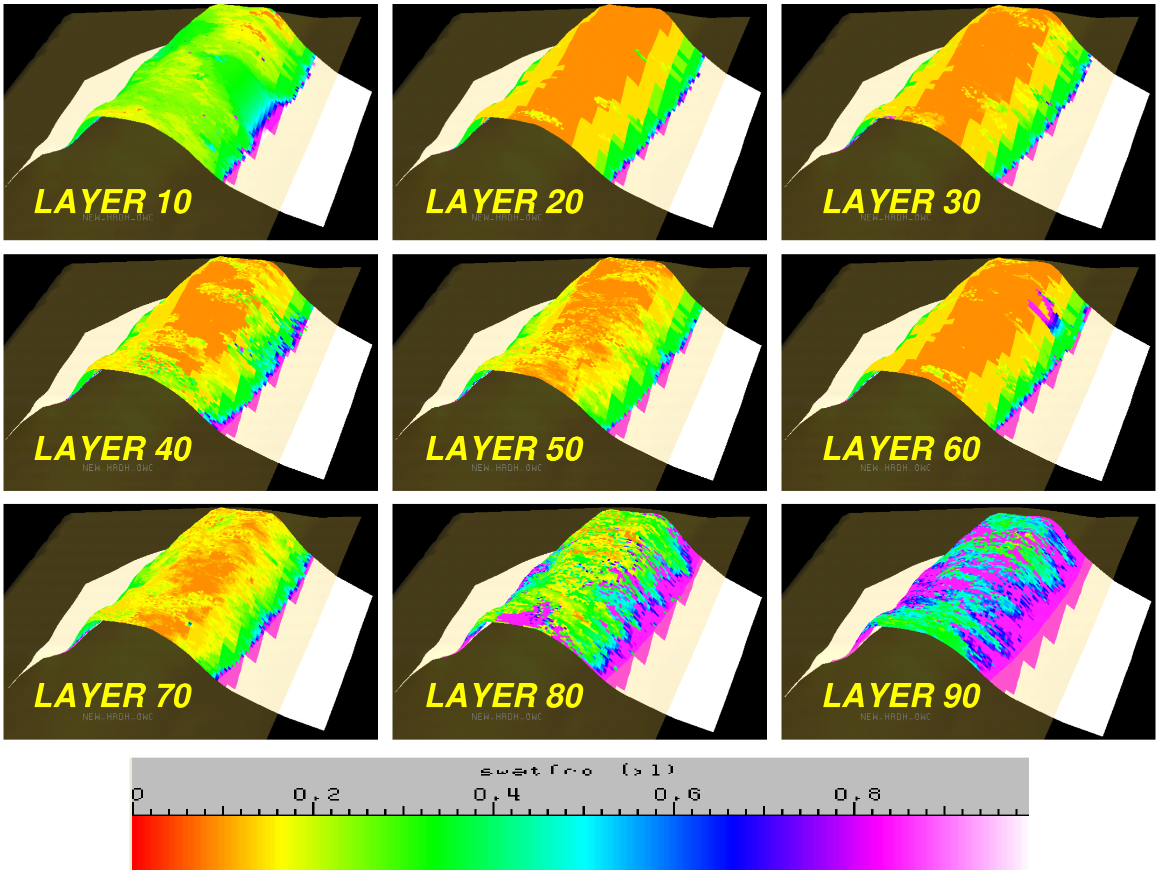

Fig. 4.21 - Water Saturation after Initialization

4.4.1 Production History

For all the wells in the simulation model, monthly production data was provided. The data was averaged on a yearly basis in a manner to preserve cumulative volumes. Averaging of the production data on a yearly basis serves two important purposes; first, the data averaging results in smoothening of the water cut profile thus making it more reliable for misfit quantification through the generalized travel time inversion technique. Second, it provides for a synchronization of the observation and simulation time steps resulting in a reduced number of simulation report steps and retracing of streamline trajectories required for data integration. Fig 4.22 shows the averaging applied to a few of the wells in the model.

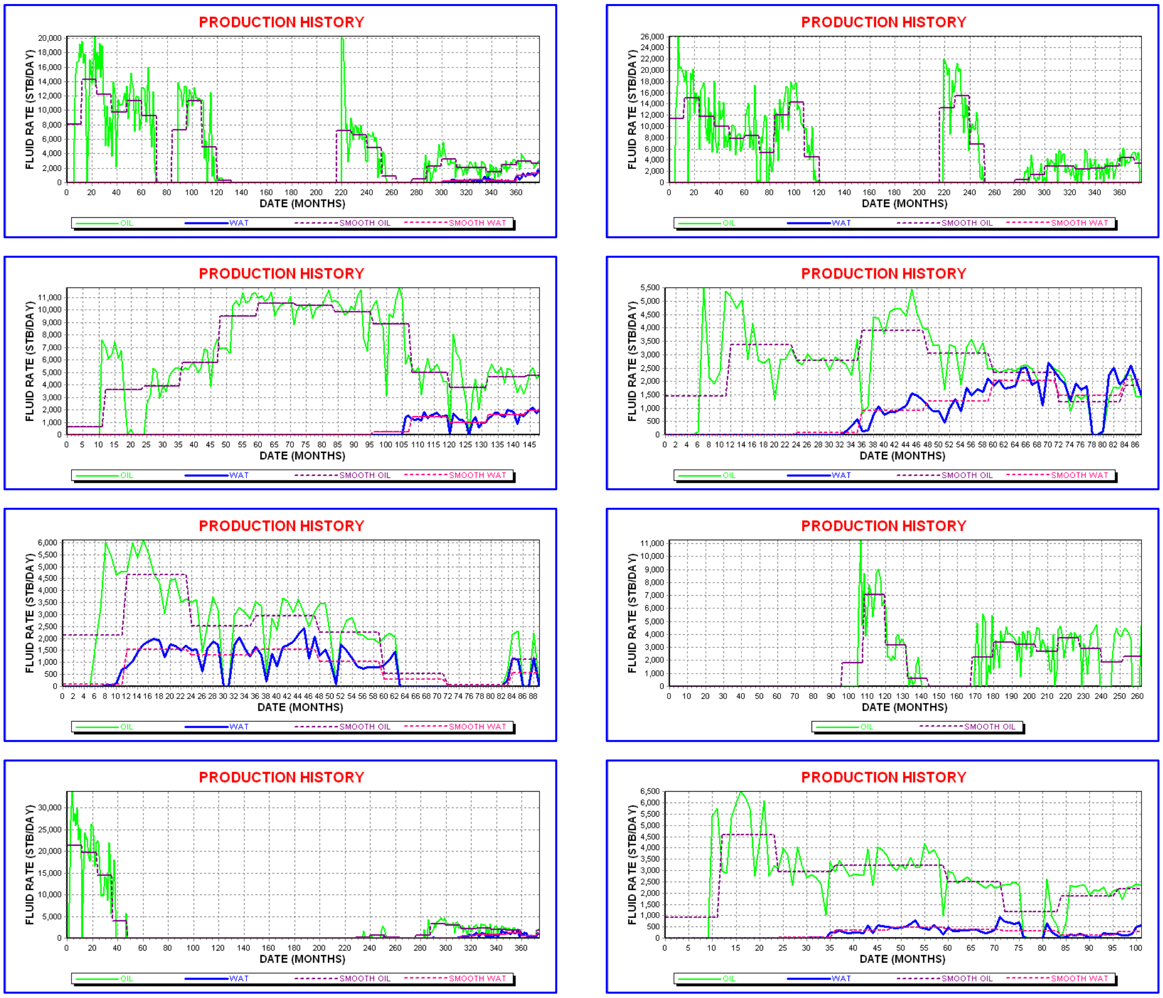

Fig. 4.22 - Averaging Production History: Results in Better Profile for GTTI Misfit Quantification and Enables Synchronization of Observation and Simulation Steps

4.4.2 Dynamic Data Integration

Similar to the field case presented earlier, this is a two phase compressible application and the simplification (watercut profile replacing water saturation component profile) to the formulation of the inverse problem earlier described applies. A comparison of the observed and calculated watercut based on the prior geologic model is shown in Fig. 4.23

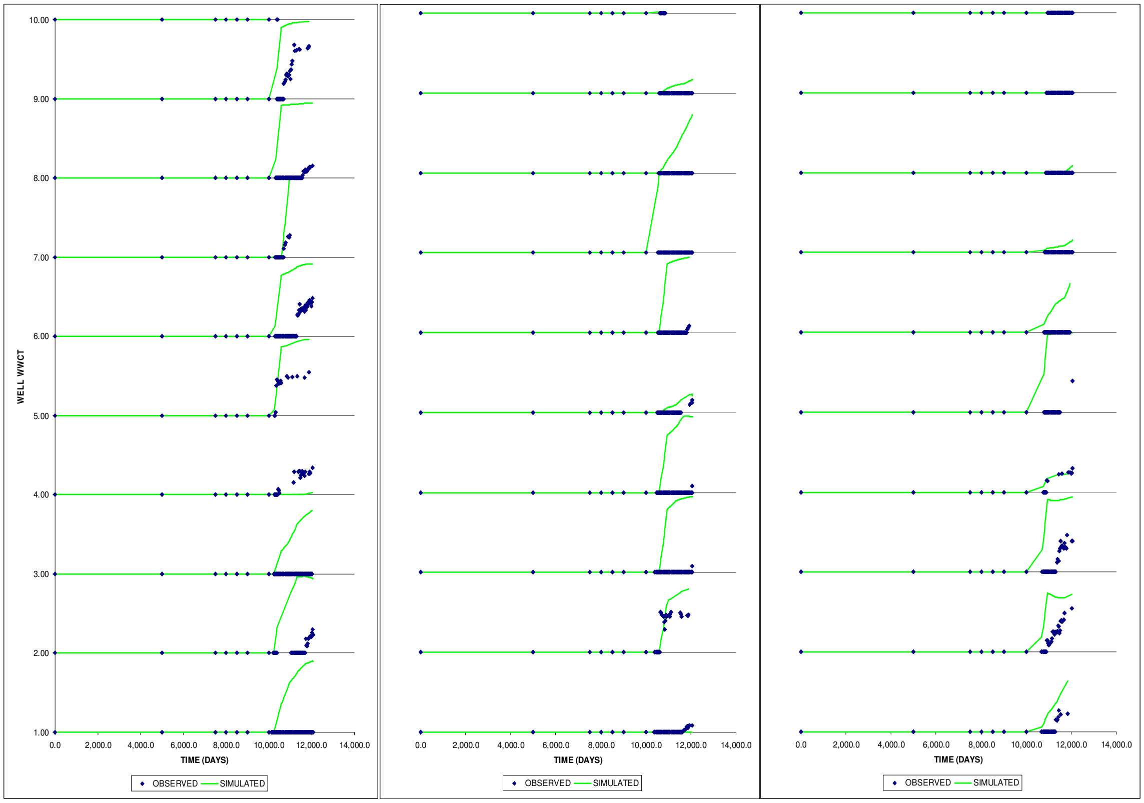

Fig. 4.23 - Increased Water Production and Early Water Breakthrough Prediction by the Prior Model as Compared to Historical Data

In most of the wells, the prior model predicts higher water production and in general, earlier water breakthrough than the historical data.

Geologic studies suggest that the field is naturally fractured however the static modeling did not incorporate any fracture modeling techniques to corroborate the idea. One of the objectives of this production data integration was to identify the locations and facies in particular, where large permeability values were required in order to match historic data thus verifying through detailed analysis, the potential correctness of the fracture concept.

The result of the history match is shown on some of the wells in Fig. 4.24. Clearly, the match for the 30+ years of production on the wells shown has been drastically improved after the saturation inversion.

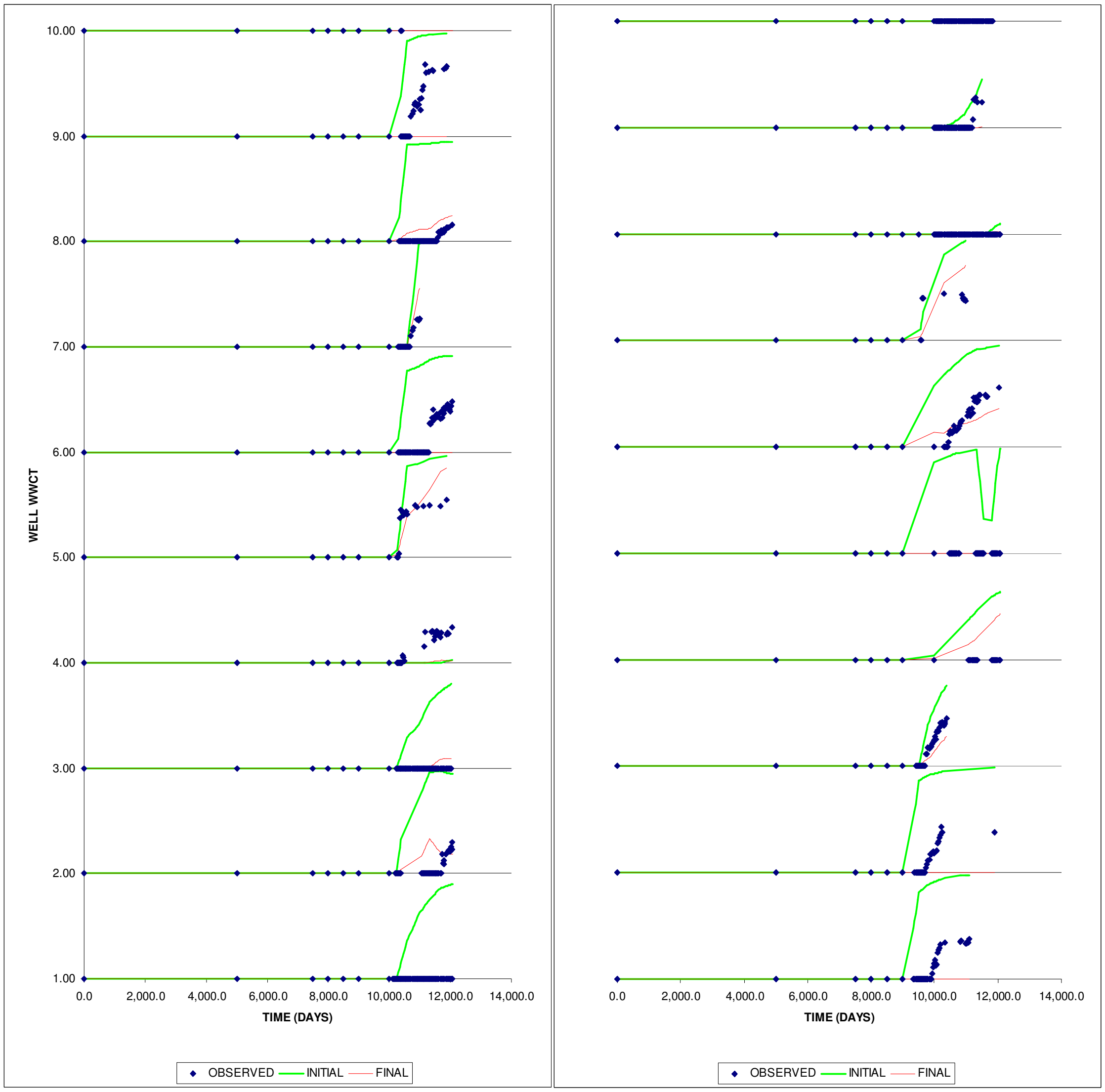

Fig. 4.24 - History Match on Some of the Wells after Saturation Inversion

4.4.3 Pre and Post Inversion Facie Analysis

In accordance with the objectives of the history match, a detailed analysis of the result of the inversion is necessary to determine which of the facies if any, is likely to contain the high conductivity streaks suggestive of the presence of fractures. The first step taken in this direction is a visual inspection on a layer basis of the locations where the positive permeability changes (permeability increased after inversion) have been made by the inversion algorithm. Consistently, in all of the layers with significant positive permeability changes, the dominating facies are the dolomitic facies. Some of these layers are shown in Fig. 4.25

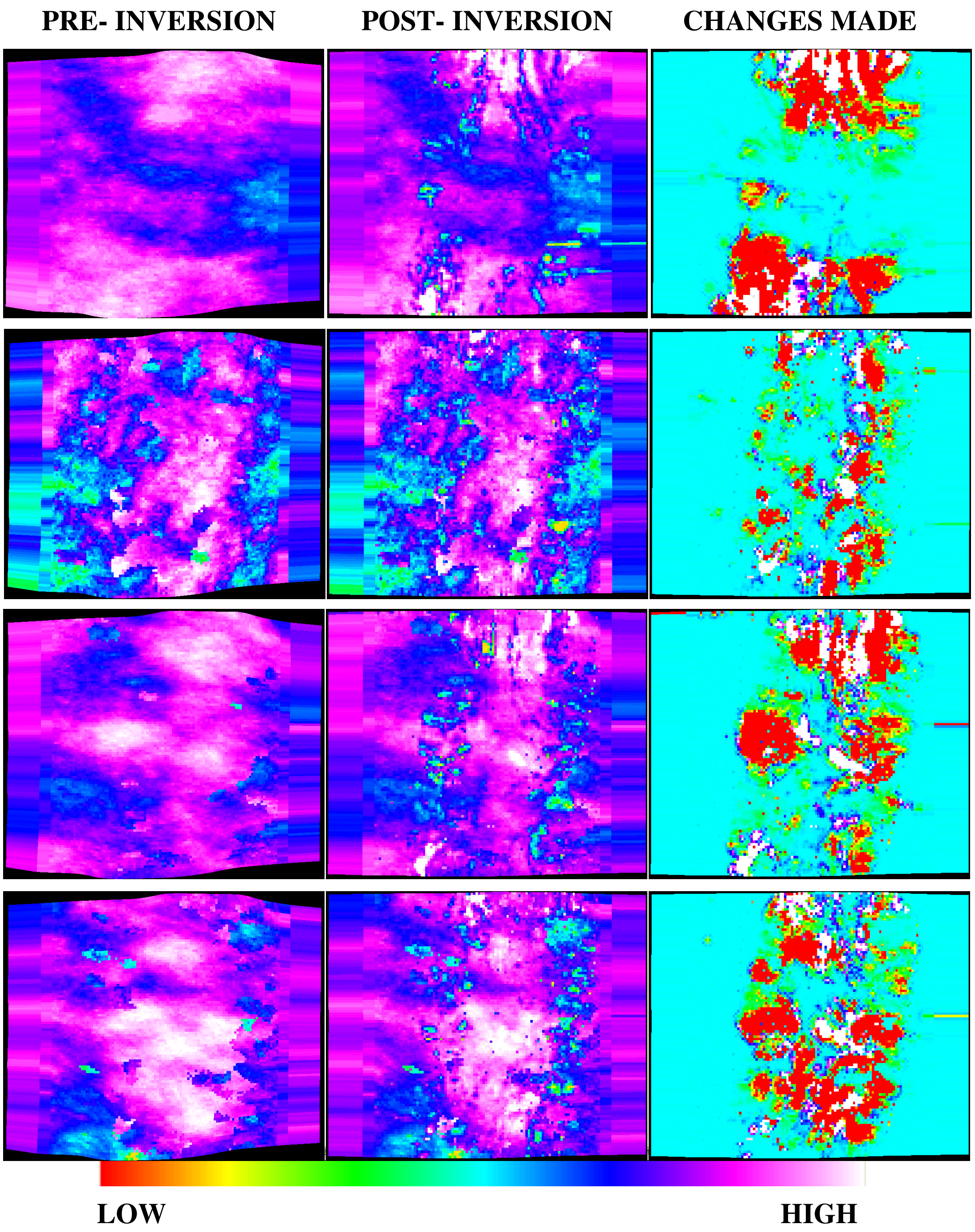

Fig. 4.25 - Layers with Predominant Dolomitic Facies Showing Increased Permeability Changes after Inversion

More detailed analysis was done based on the first two statistical moments of the pre and post inversion permeability distribution for each of the facies for better insights into drastic facie changes that might be indicative of the presence of fractures in particular facies. Histograms of the permeability distribution before and after the inversion were also built for each of the facies in the model. A comparison of the pre and post inversion permeability distribution is shown in Fig. 4.26.

Based on the analysis, conclusions drawn on each of the facies is as follows:

- Facie 1 (non-dolomitic), one of the 3 lithologies with low permeability (0.001-100md). Both probability functions show multimodal behavior. However, there is a considerable reduction in permeability that can be seen on the right tail of the posterior histogram.
- Facie 2 (non-dolomitic), this is another lithology with low permeability as compared to the rest of the lithologies. On the right half of the prior histogram zones of 20 and 200 md were removed by the inversion. The left tail of the posterior histogram shows a greater occurrence of low permeability values.
- Facie 3 (non-dolomitic), prior model showed a multimodal histogram which was preserved during the inversion. This lithology showed little change to the inversion approach except for the increase in the number of permeability values between 0.5 and 1 md.
- Facie 4 (dolomitic), this is a lithology with good reservoir properties, the right tail in the posterior histogram is clear evidence that the inversion increased the initial permeability. This kind of behavior is quite important, since it might be the foundation to make the statement of fracture presence in the model and within a particular lithology
- Facie 5¸ this is perhaps the lithology with the most extensive changes in permeability. The increase in permeability is quite considerable indicating that this lithology is most likely to contain fractures.
- Facie 6 (dolomitic)¸ the tail end to the right in the posterior histogram is a clear indicator of substantial increase in permeability.

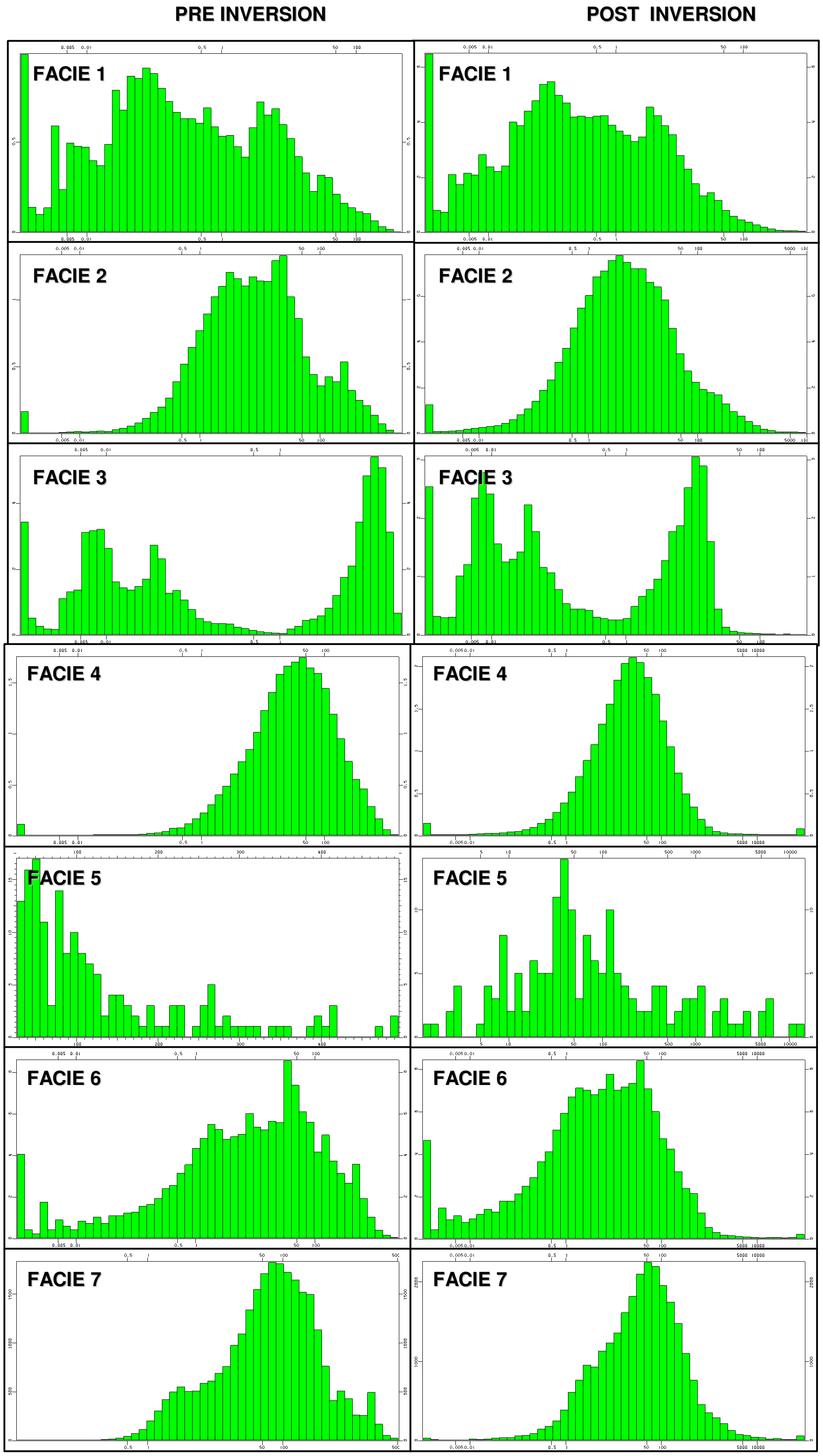

Fig. 4.26 - Facies Permeability Histograms before and after Inversion

- Facie 7 (dolomitic), this lithology is quite interesting. Although there's a permeability increase in the posterior histogram (tail to the right) within the right half of the prior histogram, zones of 200 up to 500 md were removed after inversion.

A close look at the facies-based statistical moments of the permeability indicates that the fractures appear to be located primarily in the dolomitic facies. The non-dolomitic facies have largely undergone a permeability reduction after the model calibration. Further analysis not documented here based on facie proportions analysis also supports the findings. Based on these analyses, it would appear that the result of the inversion supports the geologic understanding of the presence of fractures in the field.

4.5 Chapter Summary

In this chapter we have validated the saturation inversion technique through application to both synthetic and field cases. The field applications presented embodies some of the largest models to be automatically calibrated to the best of our knowledge. This is not surprising as we are aware of how computationally burdensome multi-million cell applications would be for most sensitivity-based methods compared to the streamline-derived sensitivity technique applied here. We have demonstrated that the convergence superiority of generalized travel time technique over amplitude inversion experienced for two-phase applications applies also to three phase applications. While we have not explicitly taken into consideration the pressure misfit in the algorithm at this point, we have constantly stressed the importance of having a good match on the pressure data for a sound model calibration. The importance of reproducing the reservoir energy through a match on the observed pressure paves the way for the discussion in the next chapter.

CHAPTER V

SATURATION AND PRESSURE INVERSION

The role of pressure in history matching in general and particularly for three phase flow is captured by the transformation of production data to saturation components discussed in chapter III (Fig. 3.2). The transformation of production data to unique pairs of gas and water saturation is valid only at a fixed pressure. As pressure changes, the mapping of production data to water and gas saturation also changes. Any uncertainty in pressure at each observation translates to an error in the in the mapping from production data to saturation components with the result that production data may be adequately matched but the saturations and pressure responsible for the observed production will not be reproduced.

In chapter IV, the focus was on saturation inversion with the assumption that we had a reasonable match on the well flowing pressures. The results of the saturation inversion only validated the formulation for the inverse model presented thus far where we have neglected the influence of pressure in the sensitivities. In this chapter, we follow an asymptotic approach to pressure inversion after Vasco and Karasaki and integrate this with the streamline-based saturation inversion workflow for a simultaneous calibration of reservoir models to production and BHP data. The formulation for the pressure inversion is first introduced and verified by synthetic applications. Next, a joint inversion of pressure and saturation is applied to both synthetic and field cases to validate the integrated algorithm.

5.1 Introduction

The approach presented by Vasco and Karasaki is based on a low-frequency asymptotic solution to the equation governing transient pressure variations. In this work, we have chosen to follow this approach to pressure inversion because it offers significant computational efficiency as both the forward and inverse modeling require the solution to two problems which are equivalent to the steady state pressure equation.[17] Also, that the approach is formulated in the frequency domain causes a substantial reduction in the amount of observations that must be considered.

5.2 Pressure Equation in Frequency Domain

The derivation as presented by Vasco and Karasaki is summarized in this section.

For two phases flowing through a reservoir, with the wetting phase denoted by *w* and non-wetting phase denoted by *n*, the governing equations are (Peaceman, 1977) [30]

$$-\nabla \bullet (\alpha\rho_n v_n) + \alpha q_n = \alpha\left[\rho_n S_n \frac{\partial\phi}{\partial t} + \phi S_n \frac{d\rho_n}{dP_n}\frac{\partial P_n}{\partial t} + \rho_n \frac{\partial S_n}{\partial t}\right] \quad \text{………..…….. 5.1}$$

$$-\nabla \bullet (\alpha\rho_w v_w) + \alpha q_w = \alpha\left[\rho_w S_w \frac{\partial\phi}{\partial t} + \phi S_w \frac{d\rho_w}{dP_w}\frac{\partial P_w}{\partial t} + \phi\rho_w \frac{\partial S_w}{\partial t}\right] \quad \text{………….. 5.2}$$

where *S* represents saturation, *P,* pressure, ρ, density, *v*, the interstitial velocity, *q*, the source or sink term associated with production or injection, ϕ is the porosity, and α the compressibility. Combining the two equations above, we arrive at an equation for the average pressure,

$$P = \frac{1}{2}(P_n + P_w) \quad \text{…………………………………………………..……. 5.3}$$

Also, assuming that the average pressure is much greater than the difference between the non-wetting and wetting phase pressure (Capillary Pressure), the equation representing the variation of pressure with space and time is given by[17]

$$\nabla \bullet [k(x)\lambda_t \nabla P(x,t)] = C\frac{\partial p}{\partial t} \quad \text{……………………………………….....….. 5.4}$$

where *k(**x**)* denotes the absolute permeability and λ_t, the total mobility

$$C = \frac{d\phi}{dP} + \phi S_n C_n + \phi S_w C_w \quad \ldots\ldots\ldots\ldots\ldots\ldots\ldots\ldots\ldots\ldots\ldots\ldots \quad 5.5$$

with C_n and C_w representing the non-wetting and wetting phase compressibility respectively.

Furthermore, the total mobility is treated as spatially varying but time invariant (an acceptable approximation for water-oil applications). Also, the coefficient C in Eq. 5.4 is treated as time invariant by assuming a non-deformable medium and similar compressibility for both wetting and non-wetting phases. With these assumptions, the coefficient is strictly a function of position x.

Expanding Eq. 5.4 and Fourier transforming to the frequency domain gives

$$\nabla(k\lambda_t) \bullet \nabla \hat{P} + k\lambda_t \nabla \bullet \nabla \hat{P} = \omega C \hat{P} \quad \ldots\ldots\ldots\ldots\ldots\ldots\ldots\ldots\ldots\ldots \quad 5.6$$

Where $\hat{P}$ is the Fourier transform of the pressure variation (Arsac, 1966).[31]

$$\hat{P}(x,\omega) = \int_0^\infty e^{-i\omega t} P(x,t)dt \quad \ldots\ldots\ldots\ldots\ldots\ldots\ldots\ldots\ldots\ldots\ldots\ldots \quad 5.7$$

5.2.1 Asymptotic Solution

With the focus being the low-frequency portion of pressure variation, a power series representation of the pressure in the frequency domain is applied given by

$$\hat{P}(x,\omega) = \frac{e^{-\sqrt{\omega}\sigma(x)}}{\sqrt{\omega}} \sum_{n=0}^{\infty} P_n(x)\omega^n \quad \ldots\ldots\ldots\ldots\ldots\ldots\ldots\ldots\ldots\ldots\ldots\ldots \quad 5.8$$

which is dominated by the first few terms of the sum when w is small. This form is motivated by the solution of the diffusion equation in a homogeneous medium for an impulsive source and follows from an approximation to the modified Bessel function for small ω.[32] The inherent assumption of an impulsive source in the asymptotic expansion causes a singularity when ω is 0. The correction for this is discussed later. Substituting the series (Eq. 5.8) into the Fourier transformed pressure equation (Eq. 5.6) results in an infinite expression with terms of various powers of $\sqrt{\omega}$. For the expansion, the two spatial derivatives are involved ($\nabla\hat{P}$ and $\nabla\bullet\nabla\hat{P}$) and are given by

$$\nabla\hat{P}(x,\omega)=\frac{e^{-\sqrt{i\omega}\sigma(x)}}{\sqrt{\omega}}\left(\nabla w(x,\omega)-\sqrt{i\omega}\nabla\sigma(x)w(x,\omega)\right) \quad \ldots\ldots\ldots\ldots\ldots\ldots\ldots\ldots \quad 5.9$$

$$\nabla\bullet\nabla\hat{P}(x,\omega)=\frac{e^{-\sqrt{i\omega}\sigma(x)}}{\sqrt{\omega}}\left\{\begin{array}{l}\nabla\bullet\nabla w(x,\omega)-\sqrt{i\omega}\nabla\bullet\nabla\sigma(x)w(x,\omega)+\\ i\omega\nabla\sigma(x)\bullet\nabla\sigma(x)w(x,\omega)-2\sqrt{i\omega}\nabla\sigma(x)\bullet\nabla w(x,\omega)\end{array}\right\}$$

$$\ldots\ldots\ldots\ldots\ldots\ldots\ldots\ldots\ldots\ldots\ldots\ldots\ldots\ldots\ldots\ldots\ldots\ldots\ldots\ldots \quad 5.10$$

where

$$w(x,\omega)=\sum_{n=0}^{\infty}P_n(x)\omega^n \quad \ldots\ldots\ldots\ldots\ldots\ldots\ldots\ldots\ldots\ldots\ldots\ldots \quad 5.11$$

substituting Eqs. 5.10 and 5.11 into Eq. 5. 6 gives

$$\begin{array}{l}k(x)\lambda_t\left\{\begin{array}{l}\dfrac{\nabla\bullet\nabla w(x,\omega)}{\sqrt{\omega}}-\sqrt{i}\nabla\bullet\nabla\sigma(x)w(x,\omega)+i\sqrt{\omega}\nabla\sigma(x)\bullet\nabla\sigma(x)w(x,\omega)\\ -2\sqrt{i}\nabla\sigma(x)\bullet\nabla w(x,\omega)\end{array}\right\}+\\ +\nabla k(x)\bullet\left\{\dfrac{\nabla w(x,\omega)}{\sqrt{\omega}}-\sqrt{i}\nabla\sigma(x)w(x,\omega)\right\}=i\sqrt{\omega}C(x)w(x,\omega)\end{array}$$

$$\ldots\ldots\ldots\ldots\ldots\ldots\ldots\ldots\ldots\ldots\ldots\ldots\ldots\ldots\ldots\ldots\ldots\ldots\ldots\ldots \quad 5.12$$

As written in Eq. 5.12, the expression is an infinite sum of terms because of the infinite series $w(x,\omega)$. Since the low frequency is considered ($\omega << 1$), the terms of lowest order in frequency are the most significant and are considered here.

Substituting the expression for the series (Eq. 5.11) into Eq. 5.12 results in an infinite series of terms of various orders in $\sqrt{\omega}$. Focusing on the terms of lowest order in

$\sqrt{\omega}$ based on the interest in low-frequency variations, the terms considered are those of order $\sqrt{\omega}^{-1}$, $\sqrt{\omega}^{-0} \approx 1$, and $\sqrt{\omega}$.

5.2.2 Expression for the Lowest Order of $\sqrt{\omega}$

The lowest order of $\sqrt{\omega}$ after expanding Eq. 5.12 by substituting for the series is $\sqrt{\omega}^{-1}$. By considering terms of this order, the resulting equation is for the zeroth-order amplitude, $P_o(\mathbf{x})$.

$$k(x)\lambda_t \nabla \bullet \nabla P_o(x) + \nabla[k(x)\lambda t] \bullet \nabla P_o(x) = 0 \quad \text{……………………..………} \quad 5.13$$

The form of the differential equation makes it adaptable to existing techniques for its numerical solution. In particular, the simulator used for the forward model may be used to find $P_o(\mathbf{x})$.[17]

5.2.3 Expression for the Next Order of $\sqrt{\omega}$

The next order of $\sqrt{\omega}$ is $\sqrt{\omega}^{0}$. The resulting equation on collecting these terms is given by Eq. 5.14 and used to determine the phase ($\sigma(x)$).

$$\Omega(x)\nabla \bullet \nabla \sigma(x) + \Gamma(x).\nabla \sigma(x) = 0 \quad \text{…………………………………………} \quad 5.14$$

where

$$\Omega(x) = P_o(x)k(x)\lambda_t \quad \text{………………………………………………………} \quad 5.15$$

And

$$\Gamma(x) = P_o(x)\nabla[k(x)\lambda_t] + 2\nabla P_o(x) \quad \text{……………………………………...} \quad 5.16$$

Thus, on solving for $P_o(x)$ through Eq. 5.13, the expressions in Eqs. 5.15 and 5.16 are evaluated and used in solving for the phase term $\sigma(x)$ in Eq. 5.14.

5.3 The Zeroth-order Expression for Pressure

The low-frequency assumption ($\omega << 1$) is such that the first term in Eq. 5.8 is dominant over all subsequent terms and the expression adequately represents the pressure variation.

$$\hat{P}(x,\omega) = \frac{e^{-\sqrt{\omega}\sigma(x)}}{\sqrt{\omega}} P_o(x) \quad \ldots\ldots\ldots\ldots\ldots\ldots\ldots\ldots\ldots\ldots\ldots\ldots \quad 5.17$$

The efficiency of this approach results primarily from the adequacy of the zeroth-order asymptotic expression (Eq. 5.17). Transitioning from time to frequency domain is then easily accomplished once $P_o(x)$ and $\sigma(x)$ are obtained from a single solution of equations 5.13 and 5.14.

5.4 Sensitivity Computation

As discussed in chapter III, model parameter sensitivities relate a perturbation in model parameter to change in the observations. In this case, perturbations in the permeability field at some point y is related to changes in observations of the Fourier transformed component $\hat{P}(x,\omega)$ at a point *x*. In deriving the model parameter sensitivities, a perturbation approach is followed:

Considering a slight change in permeability at a point *y* from an initial value $k^b(\mathbf{y})$

$$\delta k(y) = k^b(y) - k(y) \quad \ldots\ldots\ldots\ldots\ldots\ldots\ldots\ldots\ldots\ldots\ldots\ldots \quad 5.18$$

and a corresponding change in the pressure observation at position ***x*** with respect to a background pressure value $\hat{P}^b(x,\omega)$

$$\delta\hat{P}(x,\omega) = \hat{P}^b(x,\omega) - \hat{P}(x,\omega) \quad \ldots\ldots\ldots\ldots\ldots\ldots\ldots\ldots\ldots\ldots\ldots \quad 5.19$$

[Vasco et al., 2000] gives the expression for $\delta\hat{P}(x,\omega)$ in terms of the Green's function as the integral over the volume of interest V. [33]

$$\delta\hat{P}(x,\omega) = -2\int_v \nabla G(x,y,\omega)\bullet\nabla\hat{P}^b(y,\omega)\delta k(y)dy \tag{5.20}$$

Using the asymptotic expressions for the Green's function and the pressure field, the zeroth-order representation of the Green's function becomes[17]

$$G(x,y,\omega) = P_o(y,x)e^{-\sqrt{i\omega}\sigma(y,x)}\psi(\omega) \tag{5.21}$$

$\psi(\omega)$ in the equation above accounts for source and windowing of the observations and it is discussed in the next section. The notation $P_o(y,x)$ represents $P_o(x)$ for a source at y and the same applies to the phase term. The zeroth-order representation of the pressure at point *y* due to a source at $\boldsymbol{x_s}$ is given by

$$P^b(x_s,y,\omega) = P_o(x_s,y)e^{-\sqrt{\omega}\sigma(x_s,y)} \tag{5.22}$$

The spatial gradients in Eq 5.20 are

$$\nabla G(x,y,\omega) = \nabla P_o(y,x)e^{-\sqrt{i\omega}\sigma(y,x)}\psi(\omega) - \sqrt{i\omega}\nabla\sigma(y,x)P_o(y,x)e^{-\sqrt{i\omega}\sigma(y,x)}\psi(\omega) \tag{5.23}$$

$$\nabla P^b(x_s,y,\omega) = \nabla P_o(x_s,y)e^{-\sqrt{i\omega}\sigma(x_s,y)}\psi(\omega) - \sqrt{i\omega}\nabla\sigma(x_s,y)P_o(x_s,y)e^{-\sqrt{i\omega}\sigma(x_s,y)}\psi(\omega) \tag{5.24}$$

substituting Eqs. 5.23 and 5.24 into Eq. 5.20 results in

$$\delta P(x,\omega) = -2\int_v \nabla P_o(x,y)\bullet\nabla P_o(x_s,y)\psi^2(\omega)\times e^{-\sqrt{\omega}[\sigma(x_s,y)+\sigma(x,y)]}\delta K(y)dy \tag{5.25}$$

Neglecting terms of order $\sqrt{\omega}$ and higher and defining

$$\sum(x_s, x) = \sigma(x_s, y) + \sigma(y, x) \quad \ldots\ldots\ldots\ldots\ldots\ldots\ldots\ldots\ldots\ldots\ldots\ldots\ldots\ldots\ldots.. \quad 5.26$$

and

$$\prod(x_s, x, \omega) = -2\nabla P_o(x, y) \bullet \nabla P_o(x_s, y)\psi^2(\omega) \quad \ldots\ldots\ldots\ldots\ldots\ldots\ldots\ldots\ldots\ldots\ldots \quad 5.27$$

With the definition, Eq. 5.25 is written in the more compact form as

$$\delta P(x, \omega) = \int_v \prod(x_s, x, \omega) e^{-\sqrt{\omega}\sum(x_s, x)} \delta K(y) dy \quad \ldots\ldots\ldots\ldots\ldots\ldots\ldots\ldots\ldots\ldots\ldots \quad 5.28$$

The sensitivity, the partial derivative of the pressure at the observation point x due to a perturbation of the permeability at y is given by the integrand

$$\frac{\delta P(x, \omega)}{\delta K(y)} = \prod(x_s, x, \omega) e^{-\sqrt{\omega}\Sigma(x_s, x)} \quad \ldots\ldots\ldots\ldots\ldots\ldots\ldots\ldots\ldots\ldots\ldots\ldots\ldots\ldots.. \quad 5.29$$

5.5 Source and Windowing Effects

As noted earlier, the singularity seen in Eq. 5.8 at $\omega = 0$ is due to the impulsive source assumption implicit in the problem that motivates the use of the power series applied. In order to account for rate variations, the impulse response must be convolved with source-time function in the time-domain. The equivalent of this convolution in the frequency domain is the multiplication of the Fourier transform of the source-time function by the Fourier transformed impulse response. This source-time transformation is represented as $\sum(\omega)$. For a rectangular (box-car) source-time variation, the Fourier transform is the 'sinc' function, $\sin(\omega)/\omega$.[34]

Also the truncation of the observed data as determined by its starting and ending points constitutes a windowing effect. This is modeled by multiplication by a box-car function in the time-domain. In the frequency-domain, the corresponding operation is convolution by the Fourier transform of the box-car, the *sinc* function. Hence the complete response due to source variation and windowing effect is given by

$$\psi(\omega) = \sin c(\omega) \times \sum(\omega) \quad \text{………………………………………………..} \quad 5.30$$

5.6 Pressure Inversion

As presented above, the pressure inversion for the zeroth-order pressure and several frequencies is possible. In this work however, it is the zeroth-frequency component alone that is inverted offering several simplification to the presented formulation. For instance for $\omega = 0$, $\psi(\omega) = 1$ and the sensitivity term reduces to

$$\frac{\delta P(x, \omega = 0)}{\delta k(y)} = -2\nabla P_o(x, y) \bullet \nabla P_o(x_s, y) \quad \text{…………………………………} \quad 5.31$$

assuming the validity of a rectangular source-time function.

The inversion of the zeroth-frequency component follows a similar approach to that described for saturation inversion with the augmented objective function being

$$\left\|\delta P_o - M\delta k\right\| + \beta_1\left\|\delta k\right\| + \beta_2\left\|L\delta k\right\| \quad \text{………….……………………….…} \quad 5.32$$

where in this case, *M* represents the sensitivity matrix, *k*, the permeability field, and δP_o , the misfit in the zeroth-frequency component of the Fourier transformed pressure. The definition of the other terms in the norm constraint (second term) and the smoothness constraint (third term) are as previously defined in chapter III.

5.6.1 Synthetic Case: Nine Spot Model

In the previous chapter, the saturation inversion was validated by application to both synthetic and field cases. As it is clearly stated in the formulation, a complete match of the production data is achieved only after resolving both saturations and pressure. To account for pressure, we apply the low-frequency asymptotic formulation. In this section, we validate the adequacy of the zeroth-frequency component of the pressure match using a 2-D synthetic case before a joint inversion of both saturation and pressure components.

The synthetic case is the three-phase, 2-D nine-spot waterflood model used to validate the saturation inversion in chapter IV. Starting with the same homogenous model, the objective now is to match the observed flowing BHP with the described pressure inversion.

The result of the BHP inversion is shown in Fig. 5.1. Clearly, the inversion gives a good match on the observed production data for all the wells considered. The plot of the misfit reduction (Fig. 5.2) indicates a rapid convergence that is comparable to the convergence of the saturation inversion (Fig. 4.7). However, for each iteration, the sensitivity coefficients of the saturation inversion is computed in a single flow simulation while for the pressure inversion, the sensitivity coefficients are obtained from a number of static solves equivalent to the number of wells in the model. It is important to note that while the static solutions are much quicker than full transient solves, the streamline-based sensitivity computation for the saturation components is a lot more efficient than the zeroth-frequency asymptotic pressure sensitivity calculation.

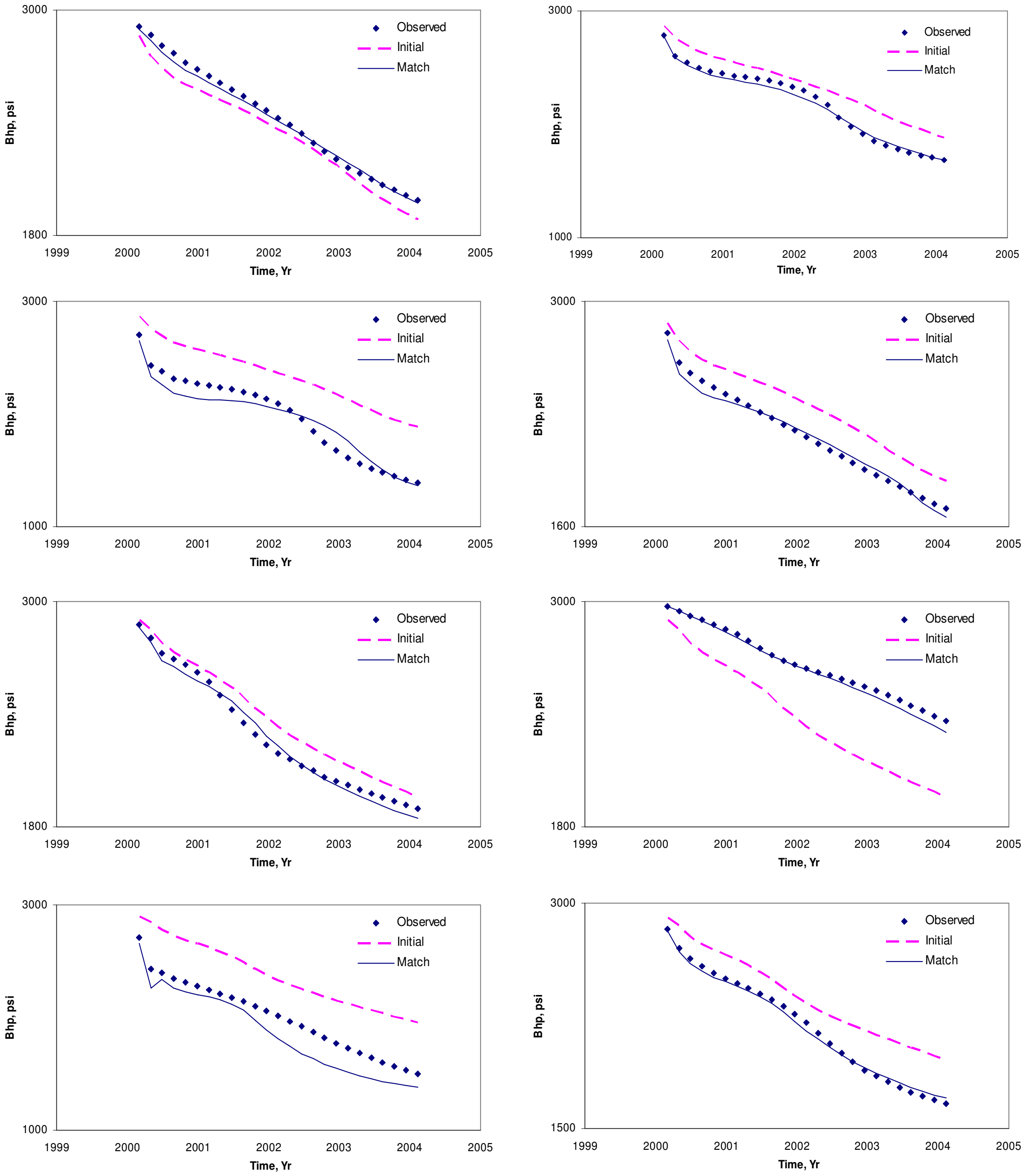

Fig. 5.1 - Nine-Spot Synthetic Case: Pressure Match Using the Zeroth-Frequency of Low-frequency Asymptotic Pressure Inversion

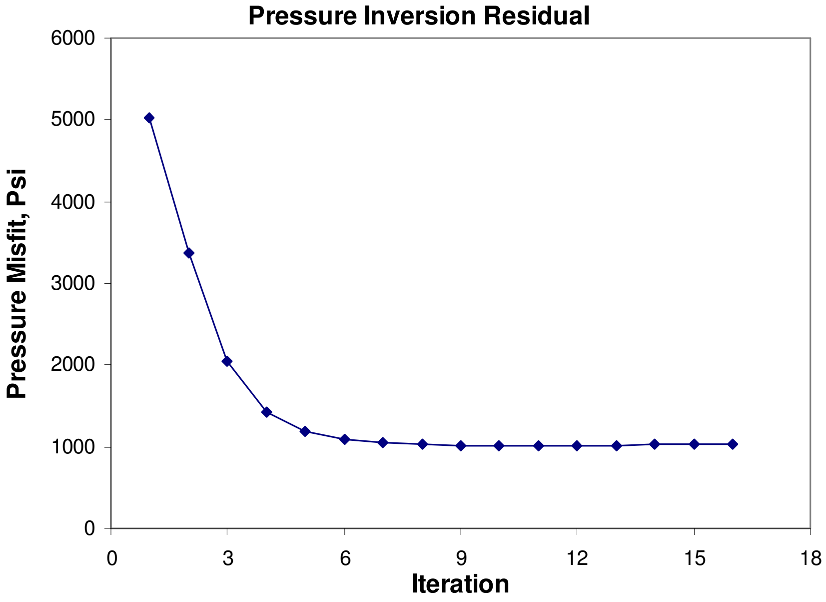

Fig 5.2 - Rapid Convergence of Pressure Inversion

5.6.2 Synthetic Case: Modified SPE9 Comparative Study

To further verify the adequacy of the zeroth-frequency component of the pressure inversion for field scale applications, it is again applied on the 3-D synthetic model that was also used to validate the saturation inversion technique. As shown for the saturation inversion, a good number of the wells in the model had a close initial match to the reference BHP while some exhibit significant disparity. For the same wells highlighted in the saturation inversion and a few more of the twenty five producers, the result of the pressure inversion is shown in Fig. 5.3. In this plot, some of the wells that started out with a reasonable match maintain the match after the inversion, while those wells with significant misfit (wells 3, 8, 16, 22, and 35) show considerable improvement after the inversion.

The successful application of the zeroth-frequency pressure inversion to both synthetic cases and its rapid convergence characteristic suggests a viable simultaneous inversion of both saturation components and the well flowing pressure in an efficient algorithm that captures both saturation and pressure components of history matching.

It should be noted that several simplifying assumptions were made in the derivation of the pressure inversion scheme such as two phase flow, similar compressibility of the two fluids and spatially varying but time invariant total mobility. While these seem quite limiting, the application of the formulation to three phase models that violate some of these assumptions shows encouraging results and motivates its application in the joint saturation and pressure inversion.

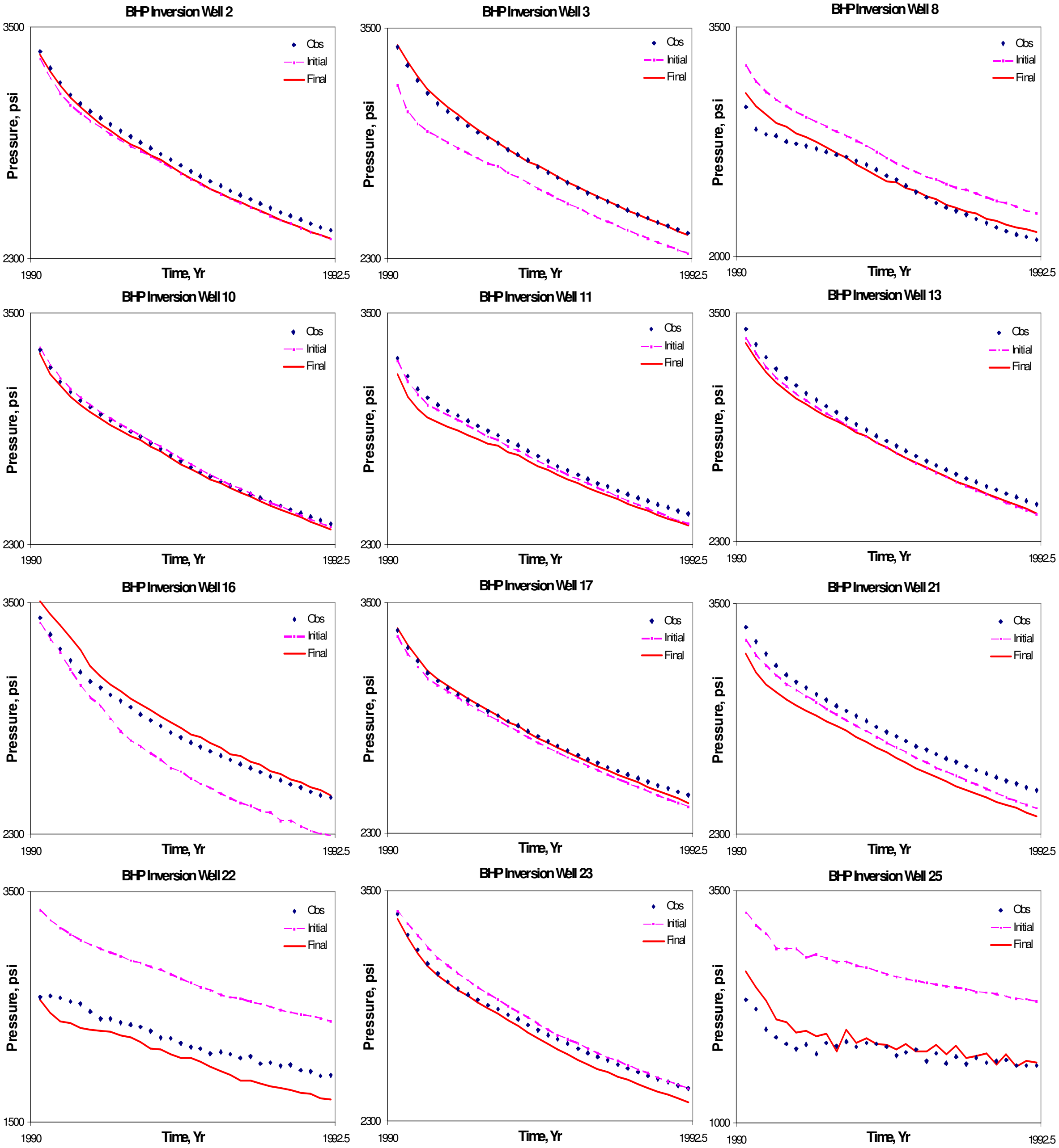

Fig. 5.3 - Pressure Inversion: Modified Ninth SPE Comparative Study

5.7 Simultaneous Inversion of Saturation and Pressure Data

In the joint inversion of saturation and pressure, the data misfit portion of the objective function (Eq. 5.33) is a combination of both the saturation and pressure misfit objectives while the regularization terms stay the same.

$$\|\delta d_s - G\delta k\| + \beta_1\|\delta k\| + \beta_2\|L\delta k\| \quad \ldots\ldots\ldots\ldots\ldots\ldots\ldots\ldots\ldots\ldots\ldots\ldots\ldots\ldots.. \quad 5.33$$

In the expression above, δd_s denotes the stacked vector of the arrival time misfit of the water and saturation components and the zeroth-frequency pressure misfit. G represents the stacked matrix of the pressure and saturation sensitivity coefficients denoted by *M* and *S* in Eqs. 5.32 and 3.7 respectively, the weighting and arguments of the regularization terms remain as previously defined. It is the iterative minimization of this augmented misfit function that constitutes the joint saturation and pressure inversion discussed in this section.

The workflow for the simultaneous integration of production and pressure data is shown in Fig. 5.4. In the inversion process, the saturation is resolved along the streamlines and pressure is resolved on the grid. This is consistent with the IMPES type formulation of streamline simulation where saturation is solved along the streamlines and pressure solution is obtained on the grids. In the sections that follow, for the same synthetic case presented earlier, we validate the joint inversion of saturation components and pressure data.

5.7.1 Joint Inversion: 2-D Three Phase Synthetic Model

The algorithm (Fig. 5.4) is applied to the two-dimensional three-phase model previously used to verify individually, the saturation and pressure inversion schemes. Applying the algorithm to the same model allows for the evaluation of the performance of the joint inversion. In this application, the initial model is the same as in previous applications and thus the initial misfit of the saturation components and those for the pressure in all the wells are exactly the same.

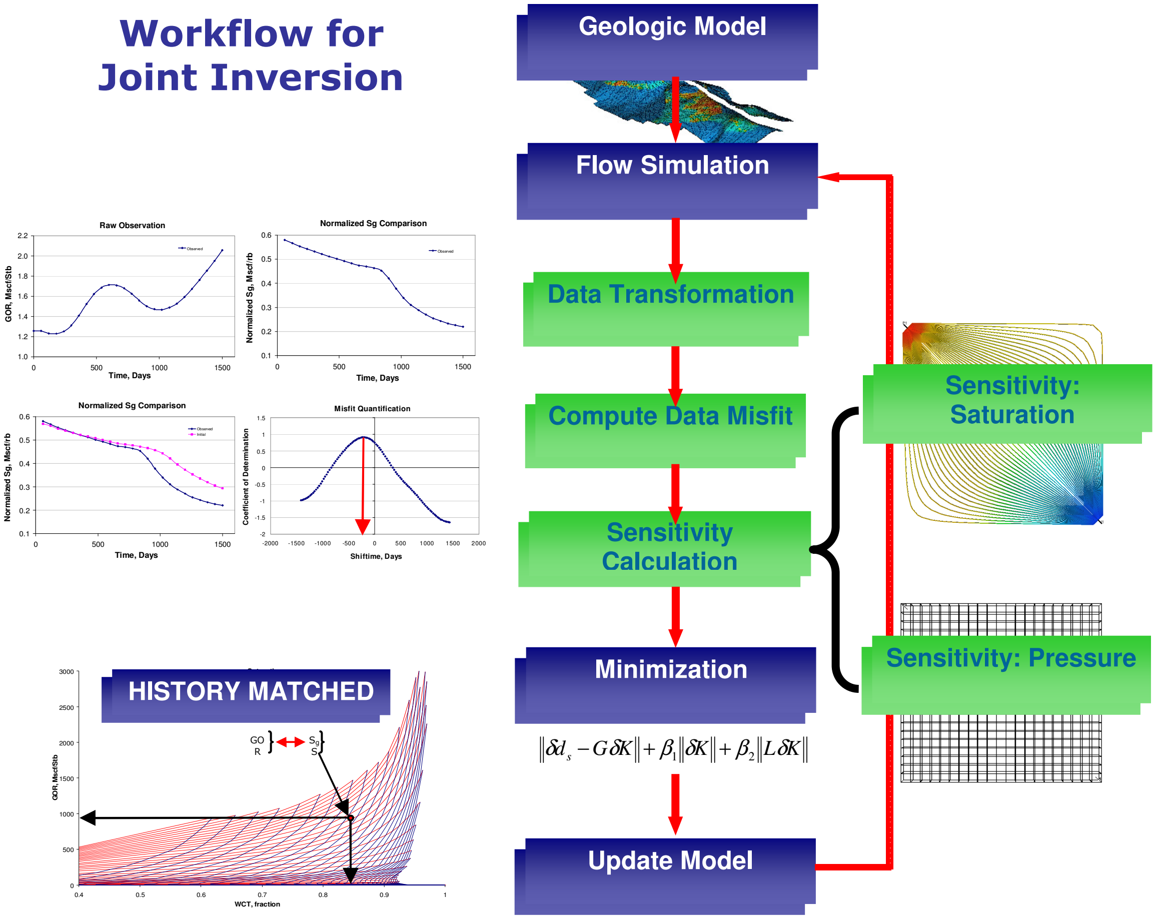

Fig. 5.4 - Workflow for Joint Saturation and Pressure Inversion

The match obtained after the saturation inversion and the resulting BHP profile for some of the wells in the model is presented in Fig. 5.5a for comparison with the match obtained after the joint inversion (Fig. 5.5b). The overall match after the joint inversion is reasonably good for both gas and water saturation components as well as the pressure. While the pressure match has been greatly improved by the joint inversion, some deterioration is noticed in the match on the saturation components and thus the derived quantities, GOR and WCT.

Separately, the saturation and pressure inversion on the same model has been shown to result in a more precise match on the saturation and pressure respectively. The slight deterioration noticed then is the result of combining both and not the inefficiency of either of the two inversion schemes.

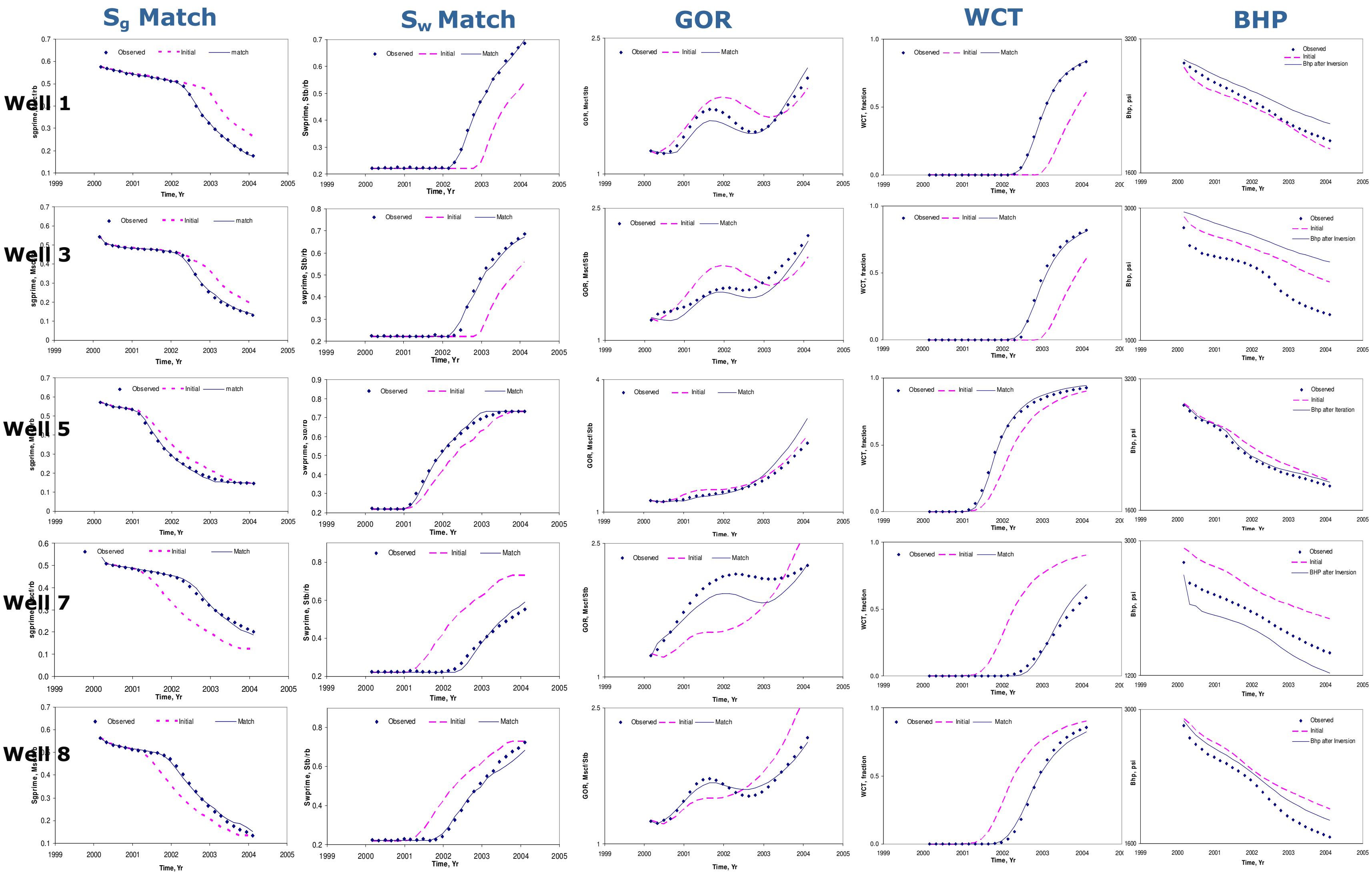

Fig. 5.5a - Synthetic Model Showing Mismatch in Pressure after Saturation Inversion

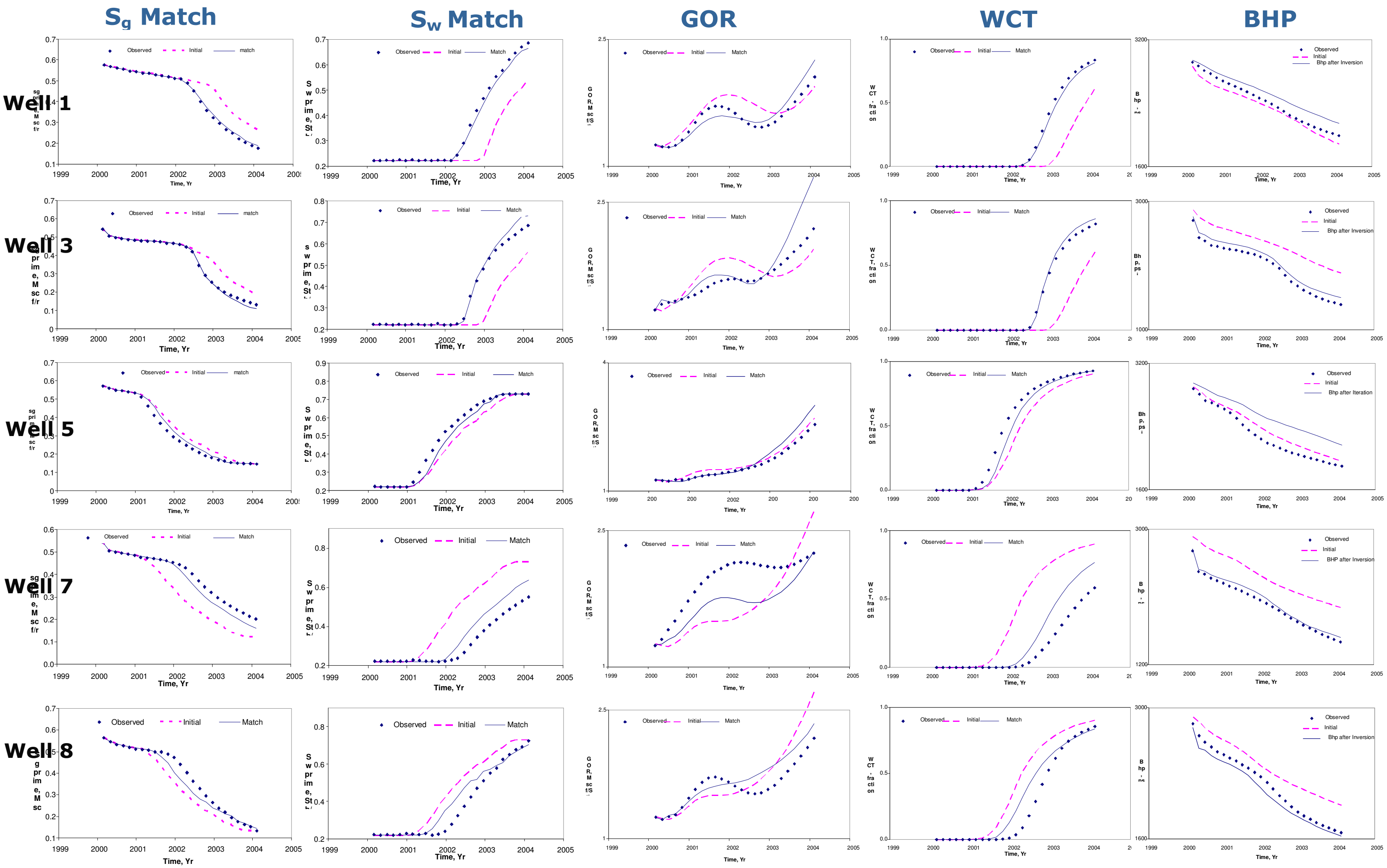

Fig. 5.5b - Synthetic Model after Joint Saturation and Pressure Inversion

Some of the several possible reasons that the joint inversion would result in some trade off between saturation and pressure match are:

- **Increased non-linearity of the problem:** As the non-linearity increases, the starting point of the inversion becomes more important as the likelihood of getting stuck in local minima is increased.
- **Difference in scale and units of data types:** Both saturation components and zeroth-frequency component of pressure included in the inversion have different units. The magnitude of the partial derivatives of the arrival time of fixed saturation components with respect to permeability will be significantly different than the partial derivative of the zeroth frequency of pressure with respect to permeability. Also, there is a difference in the number of sensitivities concerned with saturation components and those with the pressure component. During the minimization iterations of LSQR, the different scale lengths of the Hessian will affect the solution. (Williamson 1990) resulting in most of the misfit projected in a direction relative to the other.[35]
- **Increased problem difficulty:** In general the inverse problem is more difficult and the many more imposed constraint results in a more restrictive solution space.

Having highlighted the trade off in the history match, where we lose slight precision on the saturation match and obtain on the other hand a better reproduction of the reservoir energy through the match on the pressure, it is important to note that the result of the joint inversion is more valuable for reservoir management and decision making purposes thus justifying the trade off seen in this particular application.

5.7.2 Joint Inversion: A Three Phase Field Application

The field case is a highly faulted, West-African reservoir from which production started early in 1971 with an underlying aquifer providing some pressure support. The reservoir model consists of twelve layers with each layer sub divided into a 182 by 51 grid cells

(Fig. 5.6). Fluid property in the reservoir is modeled by five sets of PVT data corresponding to the different identified equilibrium regions. The first two regions have the gas-oil contact (GOC) at a depth of 5925 ftss and the water-oil contact at 6135 ftss. The third region has a shallower GOC at 5772 ftss and WOC at 5803 ftss. The last two regions have intermediate depths of the contacts with the GOC at 5790 ftss and the WOC at 5925 ftss. The rock-fluid property is modeled by a normalized relative permeability curve with the end-points and critical saturations of each cell specified. The reservoir is produced under depletion with three producers (Well 17D, Well 21, and Well 41) downthrow of the major fault. Well 17D is completed in layers 6 through 8 and has over thirty years of production history without significant water production. Well 21, also completed in the same interval, has observation limited to the early years of production. Well 41 is a more recent well completed in layers 3, 6, and 7. Among the three, Well 41 is the only well that has substantial water production. While there is sufficient pressure information for well 17D, the only pressure information available is a static BHP survey done in wells 17D and 21 and an RFT test done in well 41.

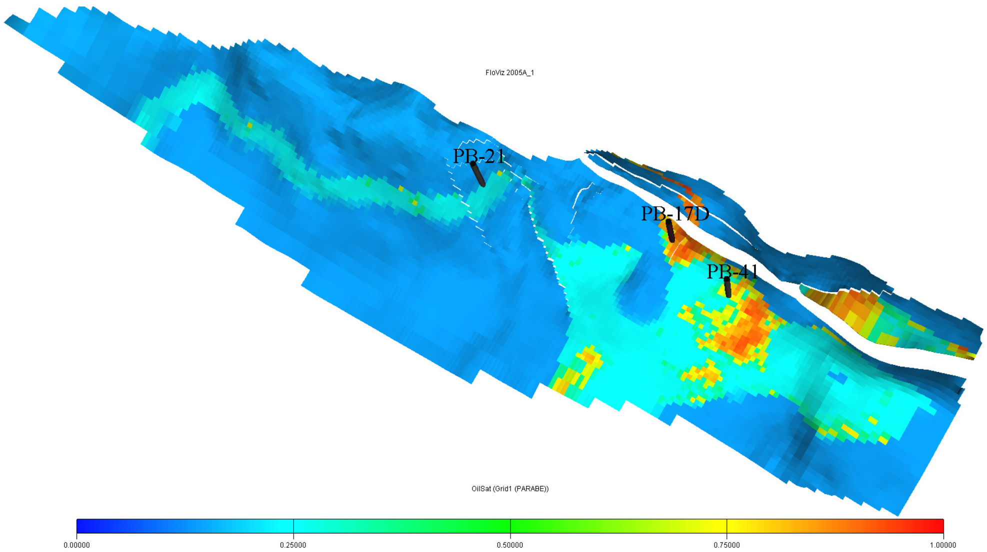

Fig. 5.6 - Three Phase Field Model with an Underlying Aquifer and a Gas Cap Produced under Depletion by Wells 21, 17D, and 41

The insufficient pressure measurement is quite typical of reservoir models in existence due to cost considerations associated with the installation of downhole monitoring equipments in every well in the field. Transforming production data to saturation components assumes knowledge of the observed pressure at each observation time as detailed in chapter II. This fundamental assumption is violated when observed pressure is not available at all observation times. To circumvent this problem, we perform first, a pressure inversion on the limited observed pressure (Fig. 5.7). With the resulting pressure profile, for each observation we now have both production data and pressure information required for the transformation of production data to saturation quantities. While the initial pressure match allows for the transformation to saturation components, the inherent uncertainty associated with lack of information (insufficient pressure data) is inherited by the saturation components through the transformation operator ***T***. This is because in between the scanty pressure measurements, the behavior of the profile is largely unknown.

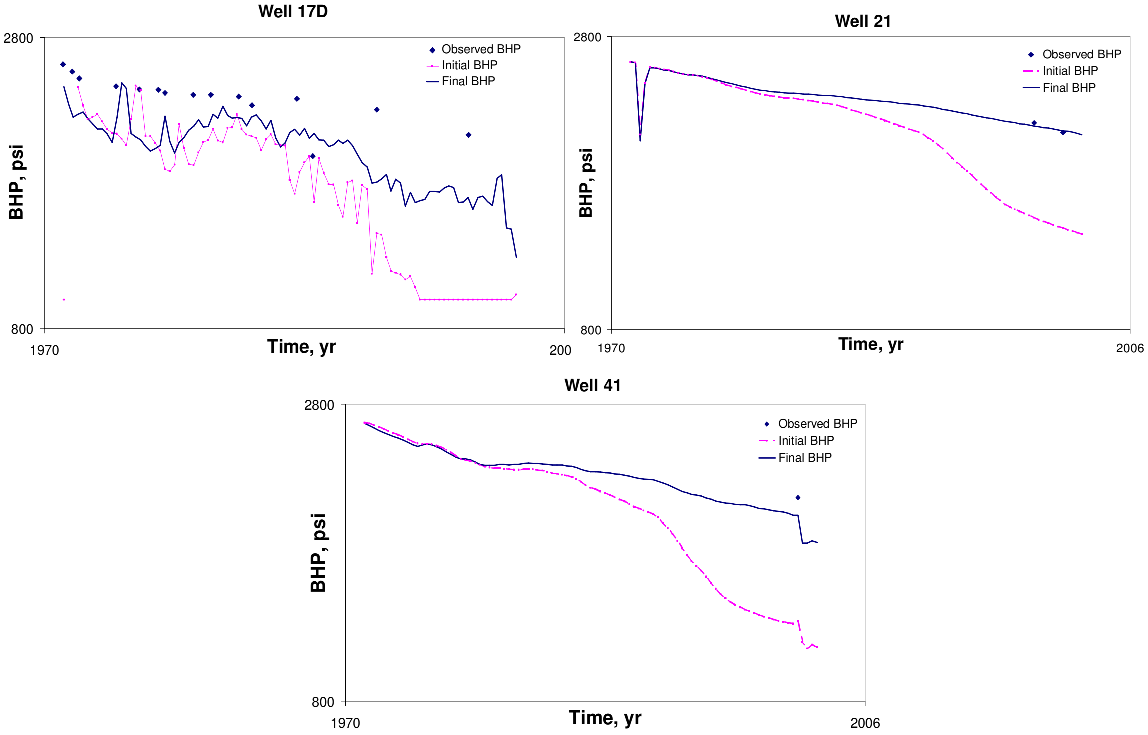

Fig. 5.7 - Initial Pressure Match on Limited Observation Gives Information Required to Transform Production Data to Saturation Components

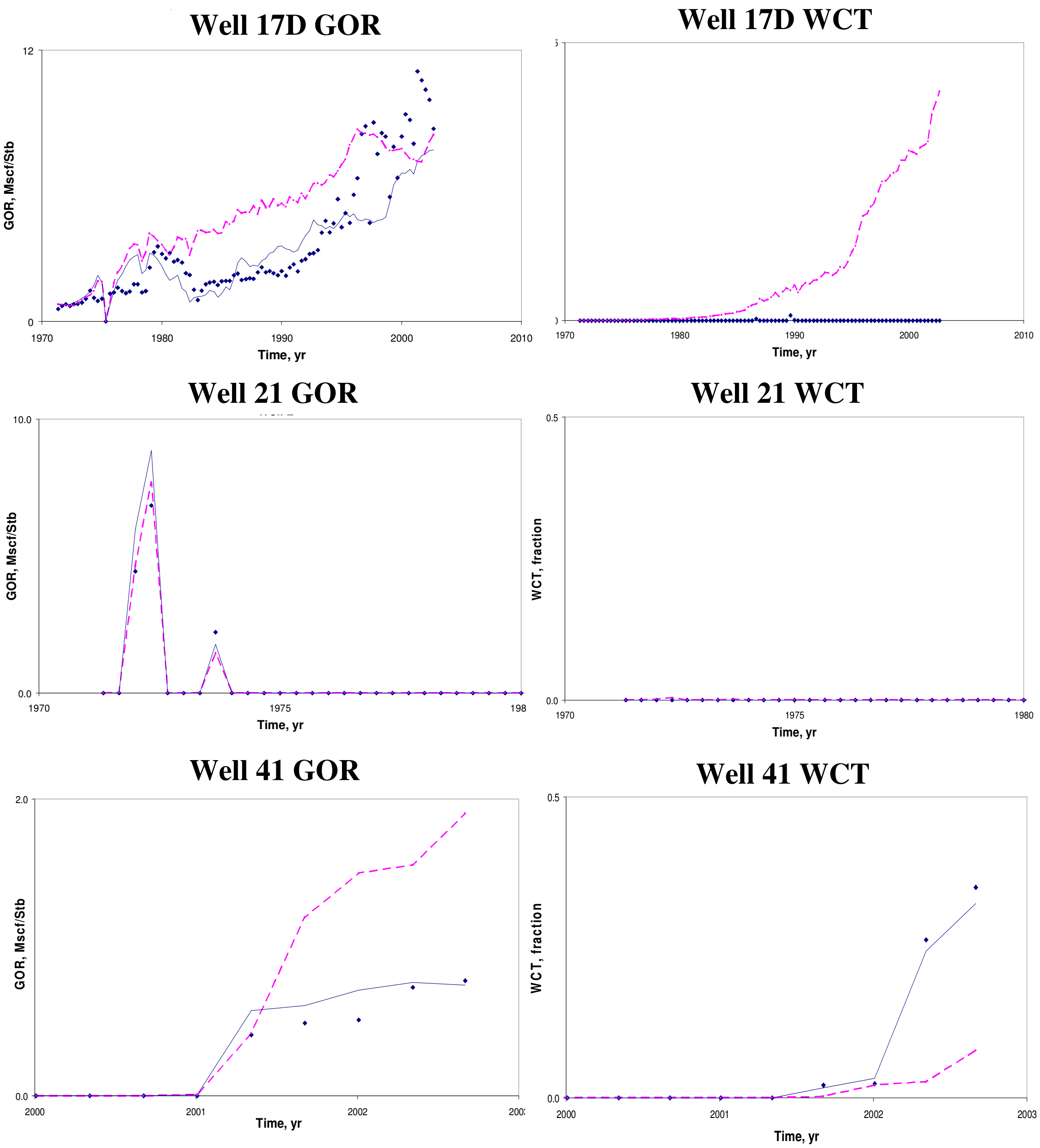

Fig. 5.8 - Saturation Match on Field Model after Pressure Inversion

The initial pressure match is followed by a saturation inversion and the result is presented in Fig. 5.8 In this plot, the pink dashed lines represent the simulated data using the initial model, the blue dots, the observed data, and the blue solid is the final match. In all the wells, the match on the historic data is reasonable for both GOR and WCT.

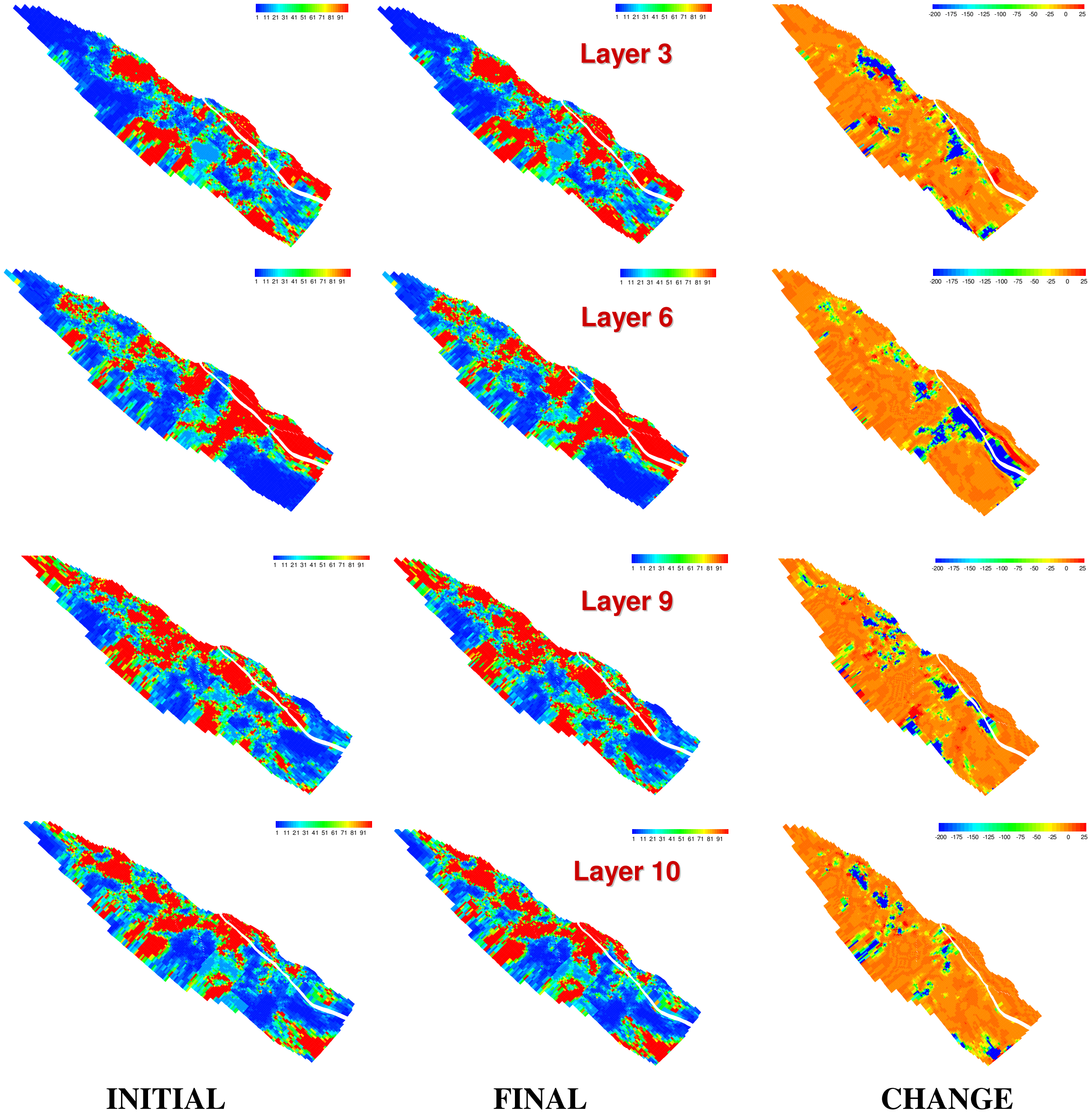

Fig. 5.9 - Geologic Realism Preserved after Data Integration

A comparison of the pre and post inversion models on a layer basis indicates the prior geologic model is preserved (Fig. 5.9). A mere visual inspection of the initial and final models as shown for some of the layers (First two columns of Fig. 5.9) is not sufficient to differentiate between the models as the changes have been efficiently integrated into the prior geologic model as imposed by the norm constraint. Changes made on these layers are obtained by differencing the prior and final permeability vectors to obtain the plot on the rightmost column of the figure.

This application is typical of most reservoir models in that the frequency of production sampling is higher than that of BHP measurement. The systematic approach presented highlights the uncertainty associated with history matching such models.

5.8 Chapter Summary

In this chapter, we discussed the mathematical formulation of the low-frequency asymptotic pressure inversion after Vasco and Karasaki. We further focused on the zeroth-frequency component in this work as a simplification of the presented formulation. The adequacy of the zeroth component was then verified by application to both 2-D and 3-D synthetic cases that have been previously used to validate the saturation inversion. The encouraging results; the rapid convergence of the zeroth-frequency pressure inversion, and the close match on the synthetic models motivates its application in addressing the pressure component of the history match which until now was assumed to be handled outside the inversion scheme. The saturation inversion algorithm presented in chapter III is then modified to incorporate the zeroth-frequency pressure inversion in a joint inversion algorithm to resolve both saturation components and pressure. The joint inversion algorithm is then validated through its application to a synthetic model.

The application to a field case needed a slight modification because of insufficient pressure data. In this case, the pressure inversion is first performed to provide pressure information at each observation of production data needed for the transformation of production data to saturation components. Then, a joint inversion of both saturation and pressure components is done following the presented algorithm.

CHAPTER VI

HANDLING GLOBAL PARAMETERS

At this point, the history matching algorithm presented is entirely consistent with the forward model. Both saturation and pressure components are resolved along streamlines and on the grid respectively. It is implicit in the formulation that any match attained in this manner assumes both relative permeability data and PVT relations are accurate. While a strong argument can be made for the accuracy of PVT data based on lab measurements, relative permeability data from analysis of core samples drawn from portions of the field; does carry along some uncertainties.

In this work, we handle the uncertainties associated with such global parameters through experimental design (ED) and response surface modeling (RSM). We focus on applications related to uncertainties associated with the set of relative permeability curves used to model rock-fluid interaction for three phase flow. While the relative permeability is the focus, the presented methodology could be applied to the PVT data and other global parameters. Each of the components is introduced first and then all components are integrated in the application that follows.

6.1 Experimental Design and Response Surface

Several authors have discussed in detail, the theory of experimental design. ED/RSM methodology has been applied in reservoir characterization applications including uncertainty modeling, sensitivity studies, and history matching. [34-39] The design problem relates to the choice of input for efficient analysis of data. Experimental design is an intelligent determination of choice input combination for minimizing the amount of experimental runs (reservoir simulation as applied here.) required to capture adequately the influence of the input parameters on the model response. In the design, several parameters are varied simultaneously with the possibility of obtaining the same information as by varying each parameter in turn, thus resulting in significantly fewer experiments or computations. This technique has been successfully applied in several different disciplines as well, for analysis and optimization of complex, nonlinear systems described by computer models.[41] A design is a set of input parameter combination with each parameter assuming different values in the set. The input parameters are designated factors and the value they assume is termed the level. There are different design methods and they differ according to the application of interest. Two particularly relevant methods are the designs used for screening and those used for response surface modeling.[42]

6.1.1 Screening Designs

The purpose of conducting a screening design is to determine from a list of potential factors influencing an outcome, those that are really important with a level of statistical confidence. Intuitively, to accomplish this, one runs a given factor at two levels (a high level and a low level) and determines if the variation in the level of a factor has any effects on the response. The easiest design for this is a “two level full factorial” design. In this case every factor is run with all the other factors at their possible levels (low, high, or centerpoint) and the main and interaction effects are determined. The two-level full factorial design requires 2^n number of runs plus the number of centerpoint (n being the number of factors). As the number of factors increase, this design type becomes unattractive as it then requires too many experiments. A variation of this method is the fractional factorial design. They are so called because they “fractionate” a full factorial design to estimate main and interaction effects without having to do all the experiments required to estimate higher order interaction terms. As it is not possible to resolve all the terms in a full factorial regression model with a fractional factorial experiment, fractional factorial designs are further categorized according to their resolution. The particular application steers the resolution option. A further simplification of the screening design experiment aimed at drastically reducing the number of experiments to be performed is the Plackett-Burman design. When the number of experiments required to estimate the coefficients in a regression model is the same as the number of coefficients themselves, the experiment is said to be saturated. The fractional factorial designs typically result in more experiments than the minimum required for saturation. Plackett-Burman designs help fill the void of inefficiency by providing designs that are saturated. The trade off that result from the savings is the ensuing aliasing between main and interaction effects.[43]

In the application here, we have for the most part, used a fractional factorial design for the screening phase of the factors as described later.

6.1.2 Response Surface Modeling Designs

In contrast to screening designs, the objective of RSM designs is to identify detailed dependence of different factors on a response. Logically, this follows the screening design after the important factors have been identified. Two notable types of RSM designs are the central composite designs (CCD) and Box-Behnken design.

The central composite design is used for building a quadratic model for the response variables that offers greater efficiency over the three-level factorial experiment. The design consists of three types of points:

- The axial points that are created by a screening analysis
- The cube points from a full factorial design, and
- A center point created by a nominal design (one in which all factors are assigned their center values.)

The CCD can be partitioned into two subsets of points; the first subset estimates linear and two-factor interaction effects while the second subset estimates curvature effects.[42] In the absence of significant curvature effects based on the analysis of data from the first subset, speed-up is gained by ignoring the second subset. CCDs provide information on experiment variable effects and overall experimental error in a minimum number of runs. The availability of varieties of CCDs that are used under different experimental regions of interest and operability offers additional flexibility to these methods. These varieties of CCD are the central composite inscribed (CCI), central composite circumscribed (CCC), and central composite face-centered (CCF). Both CCC and CCI are rotatable in that the moments of the distribution of the design remain unchanged when the design points are rotated about the center point.

Box-Behnken designs are an unusual class of three-level designs that place points on the midpoints of the edges of the (hyper-) cubical design region as well as points at the center. Fig. 6.1 shows the three-factor Box-Behnken design with three center points.

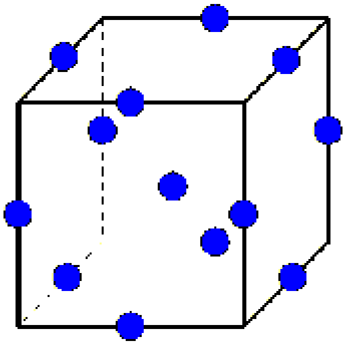

Fig. 6.1 - The Box-Behnken Design in Three Factors (NIST/SEMATECH e-Handbook of Statistical Methods, Feb. 9, 2003, Sec. 5.3.3.6.2)

Depending on the number of factors, they are rotatable or nearly so. An inspection of the figure indicates that no experiments are done at the design corners and there are no experiments where at least one of the factors is not at its midpoint. This model is appropriate if there is no interest in predicting behavior in the corners of the design space. The application to relative permeability data which is the focus of this section utilizes both the CCD and Box-Behnken designs for RSM after detailed analysis of the factorial designs in the screening stage.

6.1.3 Response Surface Modeling

Response surfaces (RS) are useful and simple proxies to experiments (simulators in this application), which relate in a closed form experimental response to input variables or experiment factors. The RS then serves as a proxy for the simulator to reduce the computational burden. Response surface models are usually low order polynomials generated using regression methods.[44] When these polynomials exhibit low accuracy in fitting the experimental data, adding more design point only marginally improves the accuracy of the response surface. For such cases, response surface methodology can be adapted by the use of interpolation methods such as splines, and kriging. The drawback of these interpolation methods is their tendency to smooth out non-linearities. [44]

Interpolation methods thus become inaccurate if non-linearity effects are strong and more so if these non-linearity effects are localized in the parameter space.

For reservoir simulation applications, response surfaces have been constructed with regression method, interpolation method, and neural network. The inaccuracy of regression methods for non-linear problems has been pointed out and thus its unsuitability for three phase applications. Interpolation methods such as kriging and 'thin plate' splines have the advantage of honoring experimental data even if scattered but have the artifact of smoothing the response surface. Neural networks could provide accurate proxies but the size of the training data set required to achieve such accuracy could be very large leading to prohibitive computational time.

We have chosen to use the 'thin plate' spline for modeling the response surface because of its computational efficiency and its appropriateness for non-linear effects. We chose this over the kriging interpolant as it does not require the assumption of the validity, and thus need for modeling of a variogram.

6.1.4 'Thin Plate' Splines

Given n control points in a plane $(\hat{x}_i, \hat{y}_i) \in \Re^n$ and their corresponding function values $\hat{v}_i \in \Re,\ i = 1,.......,n$, the thin plate spline interpolation $f(x, y)$ specifies a mapping $f : \Re^2 \rightarrow \Re$ whose bending energy E_f is minimal,

$$E_f = \iint_{\Re^2} (f_{xx}^2 + 2f_{xy}^2 + f_{yy}^2) dxdy \quad \ldots\ldots\ldots\ldots\ldots\ldots\ldots\ldots\ldots\ldots \quad 6.1$$

with the interpolation values at a point *(x, y)* given by

$$f(x, y) = \underbrace{a_1 + a_2 x + a_3 y}_{affline} + \underbrace{\sum_{i=1}^{N} w_i U\left(\left\|(\hat{x}_i, \hat{y}_i) - (x, y)\right\|\right)}_{Non-Affline} \quad \ldots\ldots\ldots\ldots\ldots\ldots \quad 6.2$$

where

$$U(r) = r^2 \log r \quad \ldots\ldots\ldots\ldots\ldots\ldots\ldots\ldots\ldots\ldots\ldots\ldots \quad 6.3$$

The interpolated spline function consists of two parts: affine transformation and the non-affine warping.[45] The affine transformation consists of the ***a*** terms in Eq. 6.2 while the non-affine warping is specified by the ***w*** terms.

Since the second derivatives of the spline $f(x, y)$ need to be square-integrable, two constraints are imposed:

1. Zero total 'force'; i.e.

$$\sum_{i=1}^{n} w_i = 0 \quad \text{...} \quad 6.4$$

2. Zero total 'force moment', i.e.

$$\sum_{i=1}^{n} w_i x_i = 0 \quad \text{...} \quad 6.5$$

As presented above, the thin plate spline is 2-dimensional. An extension of the formulation to n-dimensional space Ω was done by Li and Friedmann.[44]

In the n-dimensional space, the thin-plate spline is the fundamental solution to the bi-harmonic equation:

$$\Delta^2 U(x_1, x_2, ,........x_n) = 0 \quad \text{...} \quad 6.6$$

and the interpolant is now represented as

$$f(x) = a.\begin{bmatrix} 1 \\ x \end{bmatrix} + w \bullet U(x), x \in \Omega \quad \text{..} \quad 6.7$$

Where ***x*** is a vector of all variables or factors as applied in this section, ***a*** is the vector of coefficients, and ***w***, the weight of the non-affline component.

In application, given a set of experiments / simulations with input (factors) at different levels, and the corresponding vector of response, the thin-plate interpolant is 'calibrated' to the data. The response of any new experiment / simulations is then obtained simply by applying the 'calibrated' coefficients to the new set of input / factors.

6.2 ED / RSM Application to SCAL Data

The introductory notes on experimental design and response surface modeling presented thus far is aimed at a clear exposition of the application of ED/RSM technique to three phase relative permeability data.

In three phase applications, both the oil-water and gas-oil relative permeability curves are considered concurrently. Since the relative permeability curves are usually represented as data points based on laboratory measurements, the initial challenge relates to identifying meaningful characteristics of these curves around which the uncertainty could be modeled. The Corey model is a simple and convenient characterization of the relative permeability curves using the end points and exponents of the mobile phases in a two phase system. Thus, having specified the irreducible saturation of the phases, the Corey model completely describes the variation of the relative permeability with saturation given the endpoints and the exponents. The uncertainty in the relative permeability data in general then translates to an uncertainty in the endpoints and exponents of the Corey model as well as the irreducible saturations.

In this section, the nine-spot synthetic model that has been consistently used to validate concepts is again used to verify the methodology. The objective here is to model the more realistic scenario whereby the relative permeability data is not known accurately. This adds an additional degree of complexity to the problem as both the starting permeability field and the three-phase relative permeability data are unknown.

6.2.1 Modeling the Relative Permeability Curve and Identifying Experiment Factors

While the work here uses the Corey model for clarity, the use of splines is more general as the spline honors all the data points as opposed to the exponential-type Corey model. Although less intuitive, modeling the uncertainty in the relative permeability data using the endpoints and exponents as done with the Corey model can be achieved through an expression of uncertainty in the coefficients at each of the knots of a fitting spline.

In the synthetic case discussed, the reference relative permeability data is provided (Table 6.1) for both oil-water and gas-oil systems. With these tables, in order to fit the Corey model we perform an optimization to determine the fitting Corey exponents (n_w, n_o, n_g, *and* n_{og}). Fig. 6.2 shows the fit of the Corey model to the relative permeability data. It is clear the gas-oil relative permeability data has been adequately matched by the Corey model while the oil-water data is not as precisely matched. In this case the exponential nature of the Corey model makes it difficult to match the reference data better than achieved here. The fitting exponents to the reference relative permeability data and the endpoints are then used as factors for the screening phase of the design.

Table 6.1 - Three Phase Relative Permeability Data for Synthetic Nine-Spot Case

Three Phase Relative permeability Data (Synthetic Nine-Spot Model)					
Oil-Water Relperm Data			***Gas–Oil Relperm Data***		
S_w	**Kr_w**	**Kr_{ow}**	**S_g**	**Kr_g**	**Kr_{og}**
0.221	0	1	0	0	1
0.25	0.01	0.47	0.03	0	0.76
0.3	0.03	0.22	0.11	0.0246	0.4
0.4	0.07	0.095	0.244	0.0791	0.08
0.5	0.13	0.035	0.307	0.1212	0.021
0.582	0.179	0.008	0.37	0.1805	0.0082
0.681	0.275	0.00017	0.459	0.332	0.0014
0.701	0.305	0.000065	0.478	0.365	0.00047
0.706	0.316	0.00005	0.491	0.396	0
0.731	0.36	0			

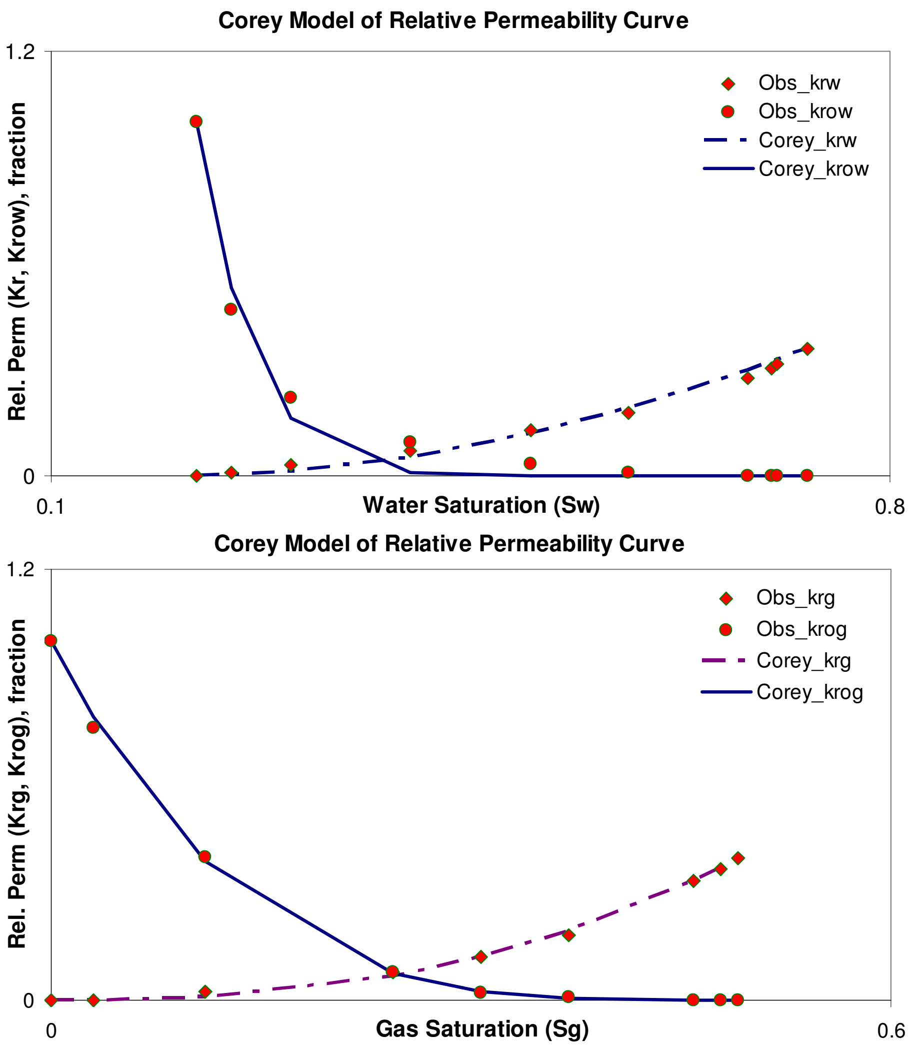

Fig. 6.2 - Corey Modeling of Relative Permeability Data

6.2.2 Identifying the Most Relevant Factors: Screening Design

Following the Corey modeling of the relative permeability data for the synthetic case, the factors for a screening design with their centerpoints are shown in Table 6.2

In the table, the low and high values represent the limits of the parameters used for the screening design phase to model uncertainty associated with the relative permeability data. These values are based on the Corey model estimate of the parameters which have been used as the center points for the experiment. For the screening design, a high resolution fractional factorial design with four center points is run on all identified factors for two responses.

Table 6.2 - Factors and Centerpoints Based on Corey Modeling of SCAL Data

Factors	Low	Center point (Corey Model)	High
n_w	1.00	1.82	2.64
n_{ow}	6.56	10.79	12.00
n_g	1.00	2.53	5.00
n_{og}	1.50	3.75	6.00
Kr_w^0	0.12	0.36	0.60
Kr_{ow}^o	0.60	1.00	1.00
Kr_g^0	0.19	0.39	0.60
Kr_{og}^o	0.6	1.00	1.00
S_{wc}	0.20	0.22	0.24
S_{orw}	0.10	0.27	0.45
S_{org}	0.18	0.29	0.4

The first response is the total watercut misfit between calculated and observed WCT obtained from the reference permeability field as well as relative permeability data (both of which we are trying to reconstruct.) and the second response is the total GOR misfit. The multiple regression analysis of the fractional factorial screening design shows some of the factors to be weakly sensitive to the response based on statistical significance test. The factors strongly influencing both responses are then used for the RSM design stage. The significant factors and the design levels are shown in Table 6.3

Table 6.3 - Seven Significant Factors and Centerpoints for RSM Design

Factors	Low	Center point (Corey Model)	High
n_{ow}	6.56	10.79	12.00
n_{og}	1.50	3.75	6.00
Kr_{ow}^o	0.60	0.80	1.00
Kr_g^0	0.19	0.39	0.60
S_{wc}	0.20	0.22	0.24
S_{orw}	0.10	0.27	0.45
S_{org}	0.18	0.29	0.4

With the streamlined factors, the next phase is the RSM design where the design experiments / simulations and responses are used with the thin-plate interpolant to generate a proxy to the reservoir simulator. For this purpose, a two-response Box-Behnken design with 5 center points is simulated. The experiment is further used to model the “thin plate” interpolant modeling the response surface. The validation of this is shown in Figs. 6.3 & 6.4 where the inherent constraint of honoring the data points is satisfied for the RSM design (Fig. 6.3)

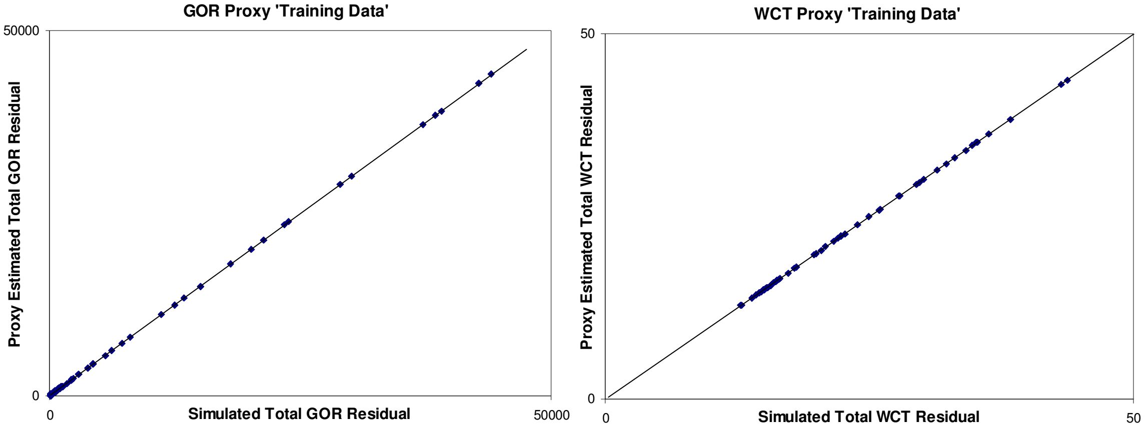

Fig. 6.3 - Thin Plate Interpolant Honors Experimental Data

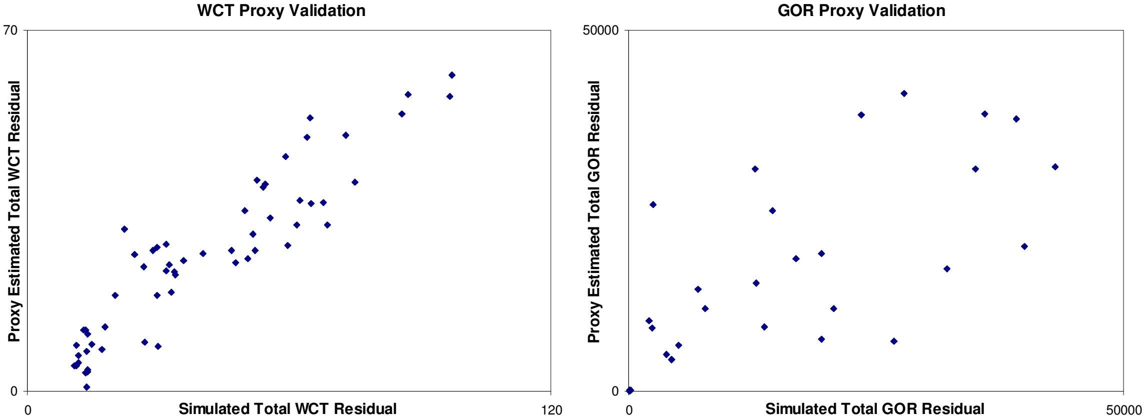

Fig. 6.4 - Proxy Validation with Screening ED More Accurate for WCT Than GOR

For a concrete validation of the proxy, the data earlier used for the screening experimental phase is used for predictive purposes (Fig. 6.4). The figure shows that the WCT residual is more accurately predicted than the GOR residual. The inaccuracy of the validation especially as related to GOR residual suggests a higher resolution design and possibly a need for the partitioning of the design. This observation further highlights the high non-linearity and thus the difficulty of history matching GOR data.

6.2.3 Monte Carlo Sampling of the Response Surface

Since the objective is find the relative permeability model that gives the lowest GOR and WCT residual, the ease of estimating the residuals using the proxy accommodates the relatively inefficient sampling of the response surface used here. It should be noted that it is indeed possible to perform a minimization on the response surface modeled by the thin plate interpolant using conventional minimization algorithms. However, the possibility of getting stuck in local minima using gradient based methods and the relative expense of applying global minimization algorithms given the simplistic nature of the interpolant is the reason behind the Monte Carlo sampling applied here. The sampling is done by creating new ‘experiments’ in a Monte Carlo fashion by generating samples from a triangular distribution that follows the estimates of the low, centerpoint, and high values of each factor. This assumed triangular distribution introduces a bias in that we would be sampling more frequently a subspace of the solution space. For generality, a uniform sampling over the range of variability of each of the factors should be applied. On sampling, a set of combinations that give the lowest residuals are analyzed to obtain a representative relative permeability model to be used for the saturation inversion. A 2-D analogy of this sampling is shown in Fig. 6.5. Ordinarily, the particular combination that gives the lowest residual would be used. However, to factor in the inaccuracy of the proxy, several experiments are analyzed. Also, as emphasized previously, the production data is uniquely characterized by the well node saturations and BHP. It is then possible to obtain experiments that have low residuals on WCT and GOR but high on BHP. It is the experiment that consistently minimizes all misfit indices that is used as a representative relative permeability model.

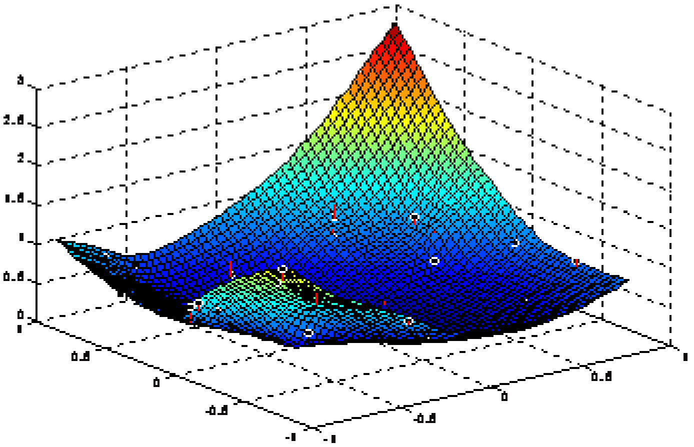

Fig. 6.5 - Sampling the Response Surface to Obtain the Experiments That Yield the Lowest Residuals: A 2-D Illustration

In this synthetic application, the selected relative permeability model based on the Monte Carlo sampling of the thin-plate modeling of the response surface is shown in solid in Fig. 6.6. The dashed line represents the reference relative permeability model; the Corey model of which is used as the centerpoint in both screening and RSM designs.

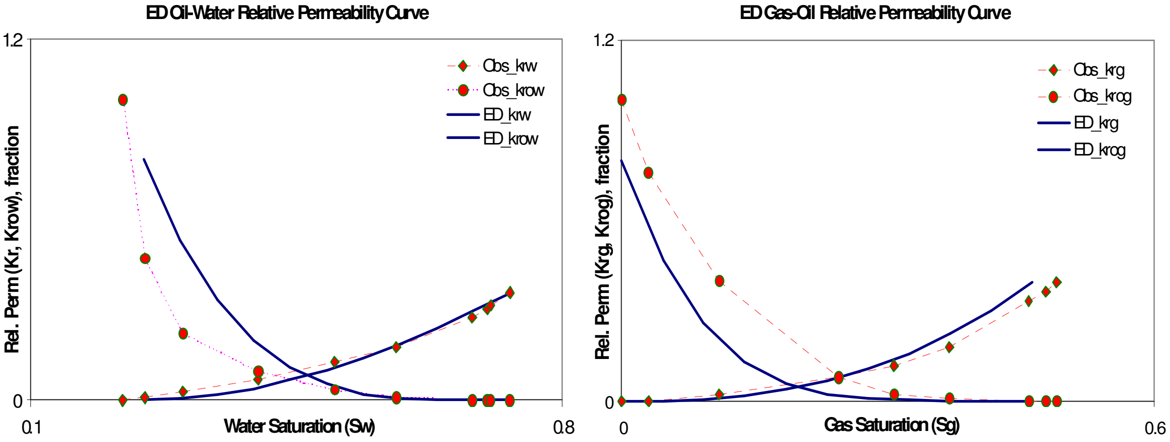

Fig. 6.6 - Relative Permeability Model Based on ED/RSM for Synthetic Case

The difference in the reference and ED generated relative permeability curves is obvious from the figure and the reason for this is not far fetched. In this particular application, both the reference permeability field and reference relative permeability model is assumed unknown. The ED/RSM reconstruction of the reference relative permeability model is then based on some permeability field that would not result in a match on the observed data even if the reference relative permeability field were to be applied. To compensate for the difference in permeability field, the ED/RSM generated relative permeability model then differs from the reference relative permeability model as presented in the figure.

With the ED/RSM generated relative permeability model, the reconstructed permeability field after saturation inversion is shown in Fig. 6.7 in comparison with the reference permeability and the reconstructed permeability using the reference relative permeability model.

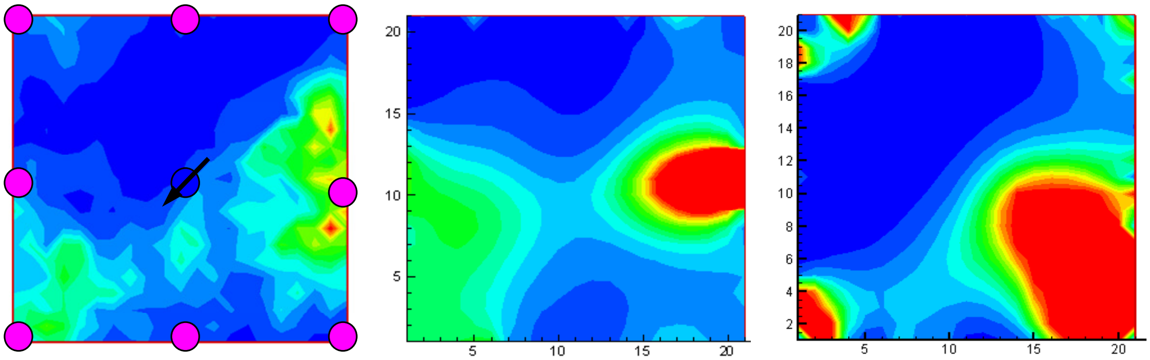

(a.) Reference Permeability Field

(a.) Reconstructed with reference Rel. Perm

(b.) Reconstructed with ED/RSM Rel. Perm.

Fig. 6.7 - Reconstructed Permeability Data with ED/RSM Relative Permeability Model Compares Well with Reference Permeability Field

The figure shows that the reconstructed permeability field after saturation inversion using the ED/RSM relative permeability curve model compares fairly well with the reference permeability. Intuitively, iterating back and forth between ED/RSM and saturation inversion would result in a decent match on both the reference relative permeability data and the reference permeability field.

6.3 Chapter Summary

The essence of the presented methodology to history matching three phase data relies on the transformation of production data to saturation components which facilitates saturation inversion using streamline-derived sensitivities. The pressure misfit is handled using the low-frequency asymptotic pressure inversion approach.

When the relative permeability data is accurately known (ideal case), history matching task of permeability reconstruction reduces to saturation and pressure match. In the more likely scenario where uncertainty exists in the relative permeability model, an additional degree of complexity arises from the fact that the saturation responsible for production is unknown. In this case, the known variables become the observed pressure, and phase production rates. The work in this chapter then suggests following the steps below to history matching three phase data:

I. An initial match on the pressure data using an initial relative permeability model through the pressure inversion methodology described in chapter IV.
II. ED/RSM remodeling of the relative permeability curves with three responses corresponding to WCT, GOR, and BHP residuals using permeability field from the pressure inversion of step 1
III. Joint integration of saturation and pressure data based on the methodology described in chapter V using the refined relative permeability derived from step 2.
IV. Check the model for geologic consistency.
V. ED/RSM remodeling of the relative permeability curves with three responses corresponding to WCT, GOR, and BHP residuals using permeability field from joint inversion of step 3.
VI. Loop over steps 3 and 4 until history is matched.

While the steps highlighted could be tedious and computationally intensive for high resolution reservoir models, it captures the high non-linearity of the problem and the interdependence of each of the variables. The suggested procedure in particular, and the work presented in general assume an accurate modeling of the fluid properties as well as measurements of well flowing pressures. In the absence of pressure measurements, it is clear that a calibration effort can be less meaningful.

For improved accuracy of the ED/RSM method, a multiple resolution approach suggested by Li and Friedmann could be used. Alternatively, more experiments could be run to provide more ‘training data’ for the TPS model to give a reliable representation of the response surface for each response variable.

CHAPTER VII

CONCLUSIONS AND RECOMMENDATIONS

7.1 Conclusions

Traditionally, calibrating reservoir models to dynamic data is done manually. The subjective overtone and the lack of geologic consistency are among the many pitfalls of this approach that have resulted in a loss of appeal for it. The need of a reliable reservoir model for timely performance prediction and economic forecast, and the advent of high resolution geocellular models have made assisted and automatic history matching algorithms more appealing for the task of history matching. Of the automatic history matching algorithms, the sensitivity-based methods have drawn particular attention because of their rapid convergence characteristics. Furthermore, streamline-based sensitivity calculation offers additional speed savings due to the one-dimensional nature of the sensitivity calculations.

In this work, the computational efficiency of the streamline approach and its successful application to high resolution two-phase models is explored and the technique is extended to three-phase applications. The systematic procedure to history matching outlined in this dissertation clearly addresses pertinent issues associated with history matching, and is fundamentally consistent with the governing equations modeling fluid flow in the reservoir. The approach presented essentially decouples the flow and transport components of the problem and resolves the transport components based on streamline-derived sensitivities, and the flow component on the underlying grid. To honor the interdependency of the variables, the inversion is done jointly for both saturation components and pressure. The adequacy of the zeroth component of the low-frequency asymptotic pressure inversion for matching pressure data for three phase flow has been verified by application to both synthetic and field cases.

Conventional approach to history matching emphasizes the requirement of reproducing the reservoir energy through a pressure match and subsequently, a saturation match. This reasoning is validated in this work and the role of pressure in history matching is made clear in the transformation of production data to saturation data that presumes knowledge of the well flowing pressure. In the absence of pressure data, the ambiguity regarding the phase saturations characterizing production is obvious and a match on phase flow rates does not translate to the reproduction of the well node saturations responsible for observed production. For this reason, when the sampling of BHP is infrequent and limited pressure information is available, compared to a more frequent sampling of well phase production rates, it is necessary to match the observed BHP first. With the resulting pressure profile, there is enough information to transform production data to saturation components and thus, proceed with the saturation inversion. However in this case, there is full awareness of the uncertainty associated with the results of the calibration exercise due to the lack of the observed pressure profile between observations.

When there is significant uncertainty associated with the relative permeability data describing the preferential fluid flow in porous media, another degree of complexity is added even if pressure data is available as this impacts the transformation of production data to saturation components. The uncertainty amounts to matching the wrong saturations at the well node. We have shown how this can be handled using experimental design and accurate response surface modeling methodology. As we cannot transform production data to representative saturation components in this case, only the observed pressure represents a reliable observation for calibration at the initial stage. However, we would be calibrating with a potentially inaccurate model of relative permeability data. This interdependence then calls for a sequential algorithm for the calibration exercise where the permeability field obtained from the initial pressure match is used for the ED/RSM reconstruction of the relative permeability data based on the minimization of WCT, GOR, and BHP residuals, followed by a joint saturation and pressure inversion with the ED/RSM relative permeability data. This procedure though tedious, highlights the non-linearity of the problem, and accentuates the need for pressure measurement for a reliable calibration of a static model to dynamic three phase data.

The generalized travel time inversion is known to have superior convergence characteristics over the amplitude inversion for two-phase applications. In this work, we have shown that such convergence superiority also applies to three-phase applications. The accurate quantification of data misfit using generalized travel time technique depends on the monotonicity of the profile. The more monotonic the profile, the more accurate the misfit quantification using generalized travel time technique is. For the typical gas-oil ratio data, the profile is non-monotonic and it is thus difficult to quantify accurately, the misfit using the generalized travel time technique. By working with saturation components as presented in this work, it is our observation that the erratic profile of GOR data is somewhat dampened thus enabling better misfit quantification using the generalized travel time technique.

The presented transformation of production data to saturation components is done strictly as a matter of necessity based on the unique approach of this method to match the fundamental variables responsible for production rather than derived quantities of WCT and GOR. This approach takes advantage of the form of the saturation equation in the streamline coordinates to directly compute sensitivities to the saturation components rather than formulating the expression for the sensitivity of derived quantities to a perturbation in reservoir parameter. The underlying idea being that a match on the saturations and pressure at the well node automatically results in a match on the derived quantities.

Based on the findings from the results obtained in the different sections of this work, the following conclusions are reached:

1. Given production data and measurements of flowing BHP, a transformation to the phase saturations characterizing production at the well node is possible. This transformation assumes an accurate knowledge of the relative permeability model. While the proposed transformation gives the phase saturations at the well node for single layer model, it is the equivalent phase saturations that is obtained for a multilayer model. To obtain particular layer phase saturations from the transformation for a multilayer model, additional data from a production logging tool (PLT) such as spinner data or an inversion of a distributed temperature sensor (DTS) data is needed.
2. The presented approach to history matching is consistent with the IMPES type formulation of the streamline forward model where the flow and transport equations are solved on the grid and along streamlines respectively. In the inversion algorithm presented, saturation residuals are resolved based on

streamline-derived sensitivities while pressure residuals are resolved through grid-based sensitivities.

3. For those reservoir models with limited observed pressure data due to infrequent measurements compared to the measurement frequency of phase production rates, an initial pressure match is required to obtain the pressure profile necessary for the transformation of production data to saturation components needed for the saturation inversion.
4. Because of the high non-linearity of the problem and potential roughness of the minimization surface, it is beneficial for the prior model to be ‘close’ to the solution. As such, an initial pressure match would be favorable irrespective of the sampling frequency of the pressure measurements compared to that of the production data.
5. When there is a significant amount of uncertainty associated with the relative permeability data, the well node saturations characterizing production obtained using the transformation is not reliable. In this case, an algorithm is presented in chapter VI that starts with a pressure match, followed by an ED/RSM methodology for reconstructing the relative permeability data, and then a joint inversion of saturation and pressure. Since the initial pressure match was done with the incorrect relative permeability data, the interdependency is honored by looping over the ED and a joint inversion of saturation and pressure.
6. Working with the defined saturation components for inversion favors the quantification of data misfit using the generalized travel-time technique because the data is more nearly monotonic for the saturation components especially for low to moderate gas saturations at the outlet node and an associated continual pressure drop.

7.2 Recommendations

Several recommendations that could improve the performance of the history matching algorithm or extend the applications of presented concepts are listed below:

1. Saturation components in the limit of two phase gas-oil flow: The central idea behind the history matching procedure in this work is the advancing of the appropriate saturation quantities to the well node. We take advantage of the form of the saturation equation in streamline coordinates to define composite saturation quantities that are advanced to the well node instead of individual saturation quantities. Thus, instead of advancing S_g and S_w, we advance $S_g^{'}$ and $S_w^{'}$ as a matter of convenience.

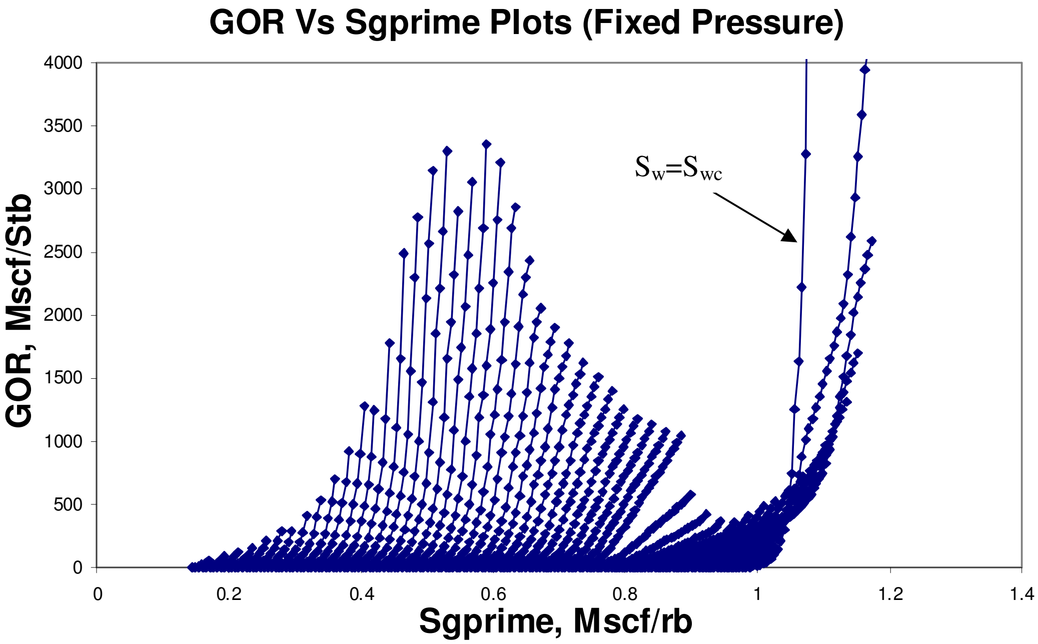

Fig. 7.1 - At Connate Water Saturation, Insignificant Changes in Sgprime Results in Huge GOR Changes

At the connate water saturation, the relationship between GOR and $S_g^{'}$ resembles a spike function (Fig. 7.1) and thus $S_g^{'}$ is not as sensitive to GOR as S_g would be. In this case, working with S_g could be beneficial.

2. In the formulation of the inverse problem, the pressure component of the sensitivity term was neglected and Eq. 7.1 below is approximated by Eq. 7.2

$$\frac{\partial S_g^{'}}{\partial t}\frac{\partial t}{\partial m}+\frac{\partial S_g^{'}}{\partial \tau}\frac{\partial \tau}{\partial m}+\frac{\partial S_g^{'}}{\partial p}\frac{\partial p}{\partial m}=0 \quad \ldots\ldots\ldots\ldots\ldots\ldots \quad 7.1$$

$$\frac{\partial S_w^{'}}{\partial t}\frac{\partial t}{\partial m}+\frac{\partial S_w^{'}}{\partial \tau}\frac{\partial \tau}{\partial m}=0 \quad \ldots\ldots\ldots\ldots\ldots\ldots \quad 7.2$$

Including this term could potentially result in the simultaneous match of both pressure and saturation components upon saturation inversion. The reasoning being that pressure is implicitly defined in the composite saturation quantities. Note that the last term of the sensitivity $\frac{\partial S_g^{'}}{\partial p}\frac{\partial p}{\partial m}$ is the product of the sensitivity of pressure to perturbations in reservoir parameter and the variation of saturation component with pressure. The low-frequency asymptotic pressure inversion gives an approximation to $\frac{\partial p}{\partial m}$ and $\frac{\partial S_g^{'}}{\partial p}$ can be obtained by numerical differentiation of the profile of $S_g^{'}$ Vs. p.

3. The saturation inversion presented inherently assumes that the pressure is not so ‘far’ from observation. The joint inversion of saturation and pressure adjusts the pressure thus negating potential problems of this assumption. It is recommended that an initial pressure inversion is done before embarking on a saturation or joint inversion in the case where this assumption is largely violated.

REFERENCES

1. Vasco, D.W., Yoon, S., and Datta-Gupta, A.: “Integrating Dynamic Data Into High-Resolution Reservoir Models Using Streamline-Based Analytic Sensitivity Coefficients,” *SPE Journal* (December 1999) 389.
2. Datta-Gupta, A. et al.: “Streamlines, Ray Tracing and Production Tomography: Generalization to Compressible Flow,” *Petroleum Geoscience* (May 2001) 75.
3. Reis, L.C., Hu, L.Y., and Eschard, R.: “Production Data Intergration Using a gradual Deformation Approach: Application to an Oil Field (Offshore Brazil)” paper SPE 63064 Presented at the 2000 Annual Technical Conference and Exhibition, Dallas, Texas, 1-4 October.
4. Landa, J.L., Kamal, M.M., Jenkins, C.D., and Horne, R.N.: Reservoir Characterization Constrained to Well Test Data: A Field Example,” paper SPE 36511, Presented the 1996 SPE Annual Technical Conference and Exhibition, Denver 6-9 October.
5. Anterion, F., Karcher, B., and Eymard, .R. “Use of parameter gradients for reservoir history matching,” paper SPE 18433, Presented at the 1989 SPE symposium on reservoir simulation, Houston 6-8 February.
6. Wu, Z., Reynolds, A. C., and Oliver, D.S.: “Conditioning Geostatistical Models to Two-Phase Production Data” *SPE Journal*, **4**(2), 142-155, June (1999).
7. Wang, Y. and Kovscek, A.R.: “A Streamline Approach to History Matching Production Data,” paper SPE 59370 presented at the 2000 SPE/DOE Symposium on Improved Oil Recovery, Tulsa, 3-5 April.

8. Sahni, I., and Horne, R.: Multiresolution Wavelet Analysis for Improved Reservoir Description". *SPE Reservoir Evaluation & Engineering*, February, 53-69, (2005)
9. Tarantola, A, *Inverse Problem Theory – Methods for Data Fitting and Model Parameters Estimation,* Elsevier, New York (1987).
10. Milliken, W.J. et al.: "Application of 3-D Streamline Simulation to Assist History Matching," paper SPE 63155 presented at the 2000 SPE Annual Technical conference and Exhibition, Dallas, 1-4 October.
11. Oliver, D.S.: "Incorporation of Transient Pressure Data into Reservoir Characterization," *In Situ,* **18**, 243-275, 1994.
12. Vega, L., Rojas, D., and Datta-Gupta, A.: "Scalability of the Deterministic and Bayesian Approaches to Production-Data Integration Into Reservoir Models," *SPEJ* (September 2004) 330.
13. Sun, N. Z. and Yeh, W.W.: "Coupled Inverse Problems in Ground water Modeling, I, Sensitivity Analysis and Parameter Identification," *Water Resources Research* (1990) **26**, 2507.
14. Datta-Gupta, A. et al.: "Streamlines, Ray Tracing and Production Tomography: Generalization to Compressible Flow," *Petroleum Geoscience* (May 2001) 75.
15. Yoon, S. et al.: "A Multiscale Approach to Production-Data Integration Using Streamline Models," *SPEJ* (June 2001) 182.
16. Cheng, H., Datta-Gupta, A., and He, Z.: "A Comparison of Travel-Time and Amplitude Matching for Field-Scale Production-Data Integration: Sensitivity, Nonlinearity, and Practical Implications," *SPEJ* (March 2005) 75.
17. Vasco, D.W. and Karasaki, K.: "Interpretation and inversion of low-frequency

head observations," *Water Resources. Research* (2006) **42**, W05408

18. Datta-Gupta, A. and King, M., 2007. *Streamline Simulation*. Society of Petroleum Engineers, ISBN: 978-1-55563-111-6
19. Cheng, H. et. al.: "Compressible Streamlines and Three-Phase History Matching, " paper SPE 99465 presented at the 2006 SPE/DOE Symposium on Improved Oil Recovery, Tulsa, 22-26 April.
20. Bear, J., 1972. *Dynamics of Fluids in Porous Media*. Dover Publications, Inc., New York, 764pp
21. Stone, H.L.: "Estimation of Three-Phase Relative Permeability and Residual Oil Data, " *JCPT*, (1973) **12**, p. 53.
22. Schlumberger GeoQuest: ECLIPSE Technical Description 2003A
23. Luenberger, D.G., 1997 *Optimization by Vector Space Methods*. John Wiley & Sons, Inc., New York, NY 10158-0012
24. McLaughlin, D. and Townley, L.R.: "A Reassessment of the Groundwater Inverse Problem," *Water Resources Research* (1996) **32**, No. 5, 1131.
25. Oliver, D.S and Reynolds, A.C. "Introduction to Petroleum Reservoir Inverse Theory.," Class notes.
26. Bates, D.M. and Watts, D.G.: "Relative Curvature Measures of Non-linearity," *J.R. Statist. Soc. B* (1980) **42**, No. 1, 1.
27. Luo, Y. and Schuster, G.T.: "Wave-Equation Traveltime Inversion," *Geophysics* (1991) **56**, 5, 645.
28. He Z., Yoon, S., and Datta-Gupta, A.: "Streamline-Based Production Data Integration With Gravity and Changing Field Conditions, " *SPEJ* (December 2002) 423.

29. Killough, J.E.: “Ninth SPE Comparative Solution Project: A Reexamination of Black-Oil Simulation,” paper SPE 29110 presented at the 13th SPE Symposium on Reservoir Simulation held in San Antonio, TX, 12-15 February 1995.
30. Peaceman, D. W., *Fundamentals of Numerical Reservoir Simulation*, Elsevier Scientific Publishing Company, North Holland, Amsterdam and New York 1977.
31. Arsac, J. (1966), *Fourier Transforms and the Theory of Distributions*, Prentice-Hall, Upper Saddle River, N.J.
32. Virieux, J., C. Flores-Luna, C., and Gilbert, D. “Asymptotic Theory for Diffusive Electromagnetic Imaging,” *Geophys. J. Int.*, **119**, 857-868.
33. Vasco, D. W.: “An Algebraic Formulation of Geophysical Inverse Problems,” *Geophys. J. Int.*, **142**, 970-990.
34. Bracewell, R. N., *The Fourier Transform and Its Applications*, McGraw-Hill, New York.
35. White, C. D., Willis, B. J., Narayanan, K. and Dutton, S.P.: “Identifying and Estimating Significant Geologic Parameters With Experimental .Design,” *SPEJ* (Sept 2001), 311-324.
36. Brandsaeter, I., Wist, H.T., Naess, A., Lia, O., Arntzen, J. et al.: “Ranking of Stochastic Realizations of Complex Tidal Reservoirs Using Streamline Simulation Criteria,” *Petroleum Geoscience* (2001) **7**, S53-S63.
37. Manceau, E., Mezghani, M., Zabala-Mezghani, I. and Roggero, F.: “Combination of Experimental Design and Joint Modeling Methods for Quantifying the Risk Associated With Deterministic and Stochastic Uncertainties-An Integrated Test Study,” paper SPE 71620 presented at the 2001 SPE Annual Technical Conference and Exhibition, New Orleans, Louisiana, September 30-October 3.

38. Friedmann, F., Chawathe, A. and Larue, D.K.: “Assessing Uncertainty in Channelized Reservoirs Using Experimental Designs,” paper SPE 71622 presented at the 2001 SPE Annual Technical Conference and Exhibition, New Orleans, Louisiana, September 30-October 3.
39. White, C.D. and Royer, S.A.: “Experimental Design as a Framework for Reservoir Studies,” paper SPE 79676 presented at the 2003 SPE Reservoir Simulation Symposium, Houston, Texas, February 3-5.
40. Parish, R.G., Calderbank, V.J., Watkins, A.J., Muggeridge, A.H., Goode, A.T. et al.:“Effective History Matching: The Application of Advanced Software Techniques to the History Matching Process,” paper SPE 25250 presented at the 1993 SPE Reservoir Simulation Symposium, New Orleans, Louisiana, February 28-March 3.
41. Sacks, J., Welch, W.J., Mitchell, T.J. and Wynn, H.P.: “Design and Analysis of Computer Experiments,” *Statistical Science* (1989) **4**, 409-435.
42. Douglas C. Montgomery, *Design and Analysis of Experiments*, 3rd ed., 1991, John Wiley & Sons, Inc. New York, NY(ISBN 0-471-52000-4)
43. Li, B. and Friedmann, F.: “Novel Multiple Resolutions Design of Experiment/Response Surface Methodology for Uncertainty Analysis of Reservoir Simulation Forecasts,” paper SPE 93853 presented at the 2005 SPE Reservoir Simulation Symposium, Houston, Texas, January 31- February 2.
44. Lim, J. and Yang, M.: “A Direct Method for Modeling Non-rigid Motion with Thin Plate Spline,” *CVPR.,* **1**, 1196 - 1202.

APPENDIX A

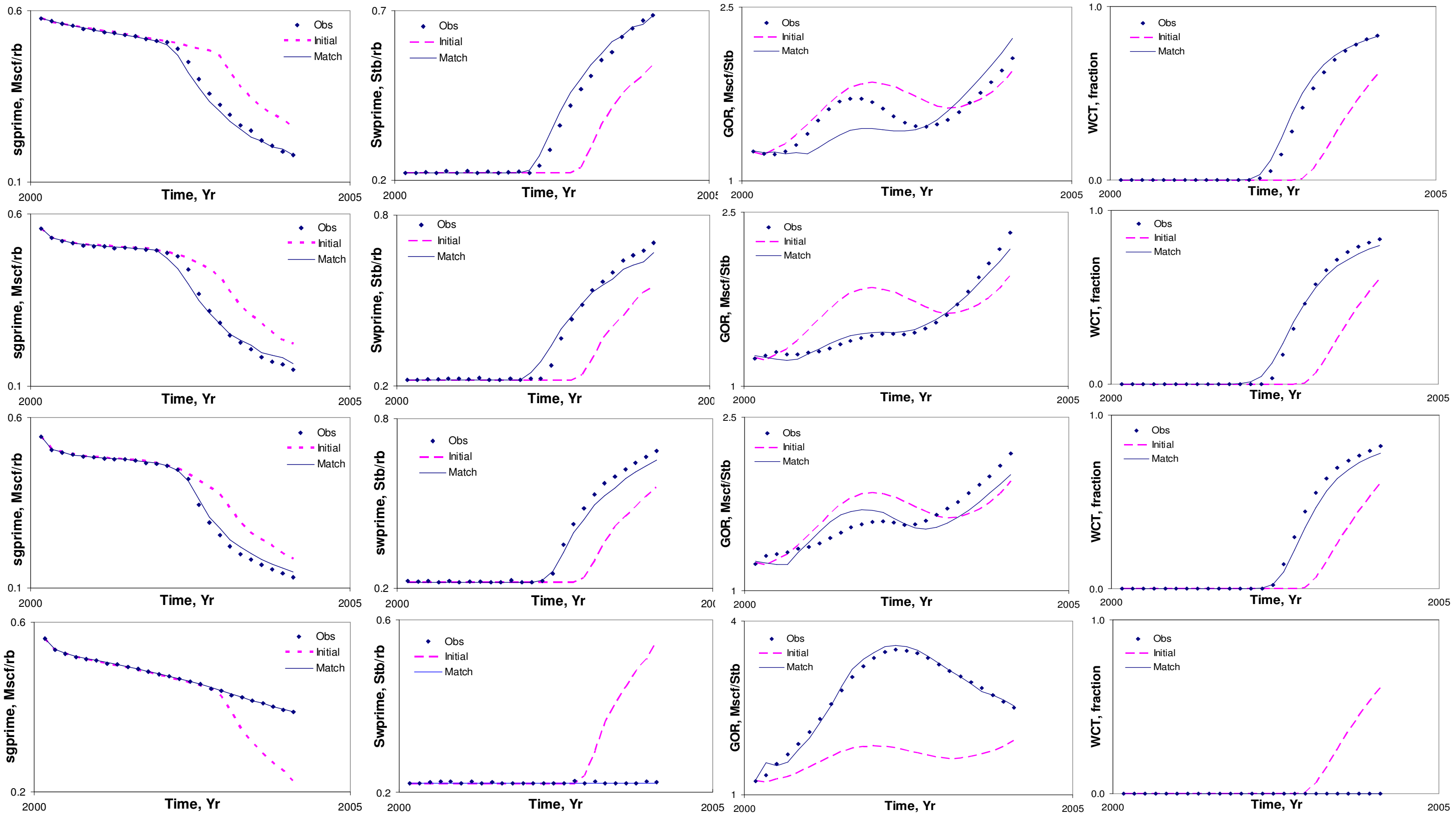

Fig. A-1 – Synthetic Nine-Spot Model: Amplitude Match on Saturation Components (Wells 1-4)

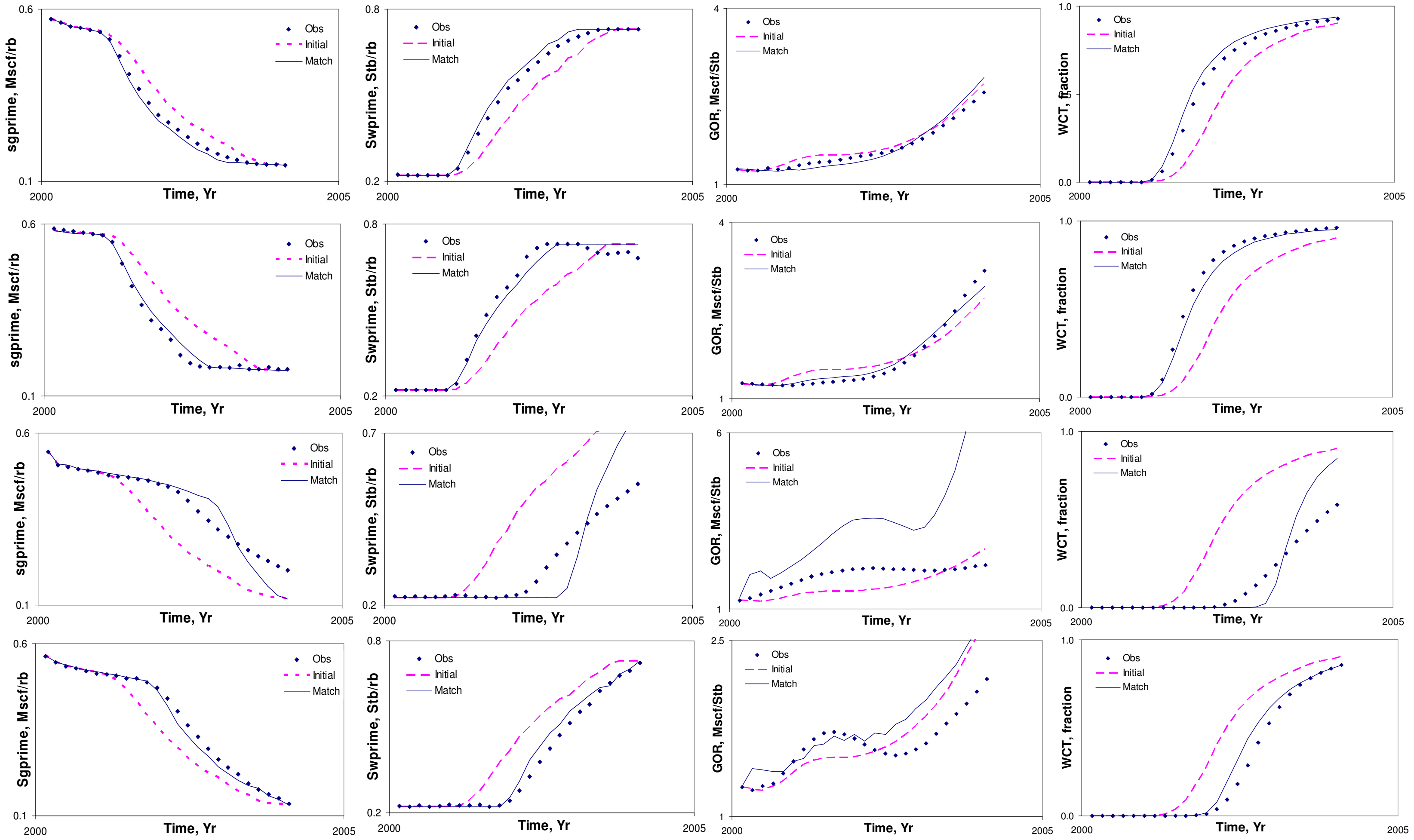

Fig. A-2 – Synthetic Nine-Spot Model: Amplitude Match on Saturation Components (Wells 5-8)

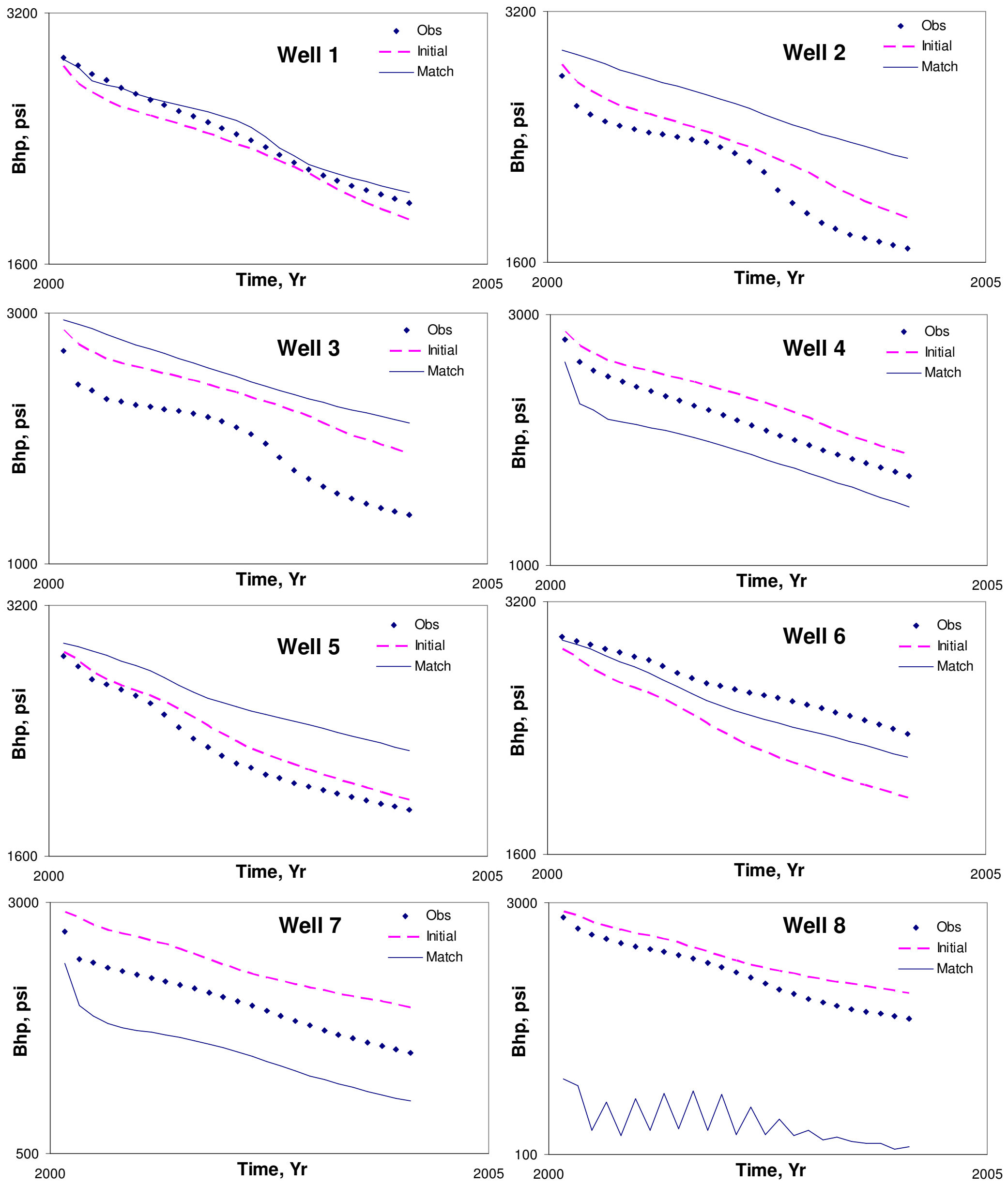

Fig. A-3 – Synthetic Nine-Spot Model: Pressure Comparison after Amplitude Match on Saturation Components

APPENDIX B

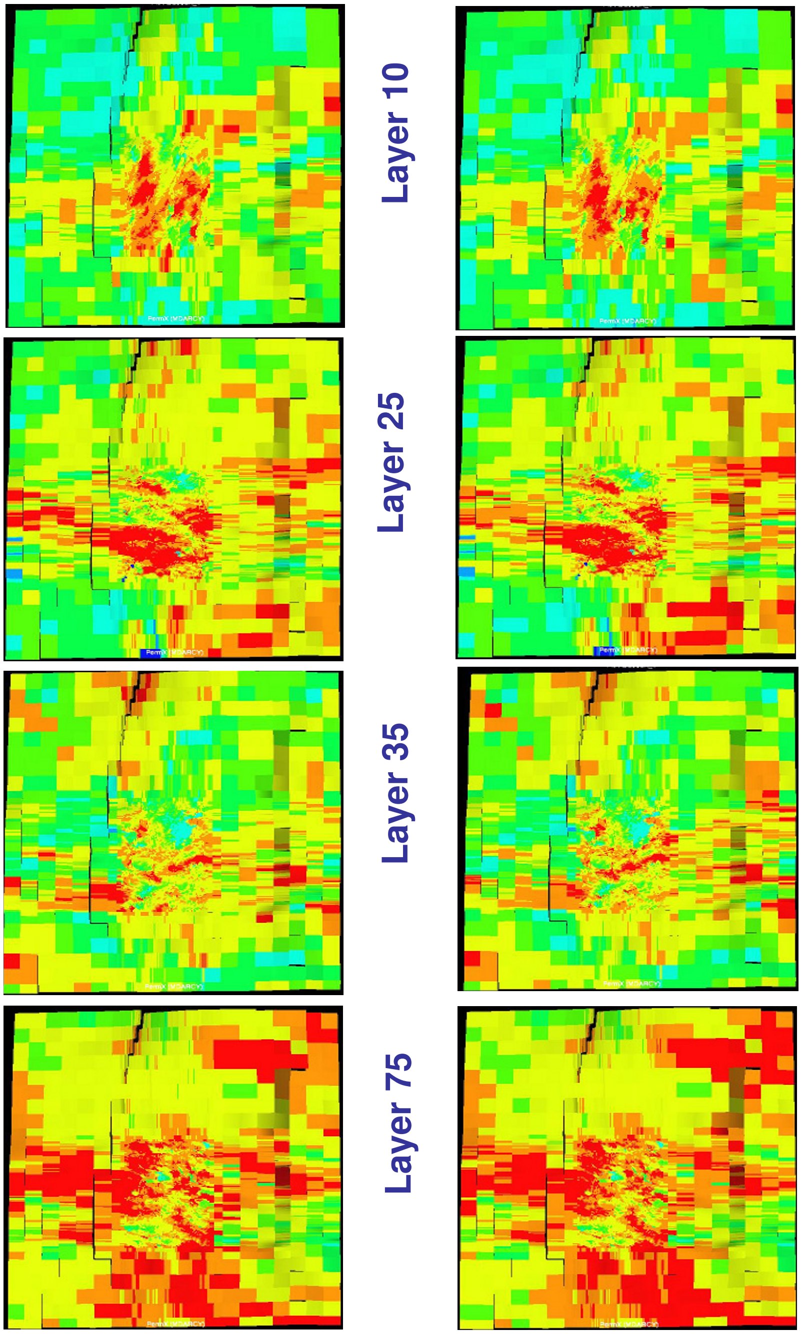

Fig. B-1 – Preservation of Prior Model after Reconciling over 50 years of Production History on a Million Cell Model, Giant Asian Field.

VITA

Adedayo Stephen Oyerinde completed his Bachelor of Science degree at the University of Ibadan, Department of Petroleum Engineering, Nigeria in May 2000, and later obtained his Master of Science degree at the Harold Vance Department of Petroleum Engineering, Texas A&M University, in August, 2004. His permanent address is 83, Hospital road, Badagry, Lagos, Nigeria.